

**Quantifying the Roughness of
Vegetated Versus Non-Vegetated
Riverbanks Using Terrestrial Laser
Scanning**

Grigorios Vasilopoulos
May, 2013

Quantifying the Roughness of Vegetated Versus Non-Vegetated Riverbanks Using Terrestrial Laser Scanning

by

Grigorios Vasilopoulos

Thesis submitted to the University of Southampton in partial fulfilment of the requirements for the degree of Master of Science in Geo-information Science and Earth Observation, Specialisation: Environmental Modelling and Management

Project Supervisor
Professor Stephen E. Darby

UNIVERSITY OF
Southampton

Disclaimer

This document describes work undertaken as part of a programme of study at the University of Southampton. All views and opinions expressed therein remain the sole responsibility of the author, and do not necessarily represent those of the institute.

Abstract

Riverbank erosion is one of the most important processes in fluvial dynamics affecting physical, environmental and socio-economic issues. The presence of vegetation on riverbank affects the flow dynamics and consequently the erosional and depositional processes and forms. An excess shear stress model is most commonly used for the quantification of bank erosion rates, which incorporates the skin drag component of the boundary shear stress. However, the accurate estimation of the skin drag requires the estimation of the dominant form drag component of the boundary shear stress, for which dense topographic measurements are necessary. This has been a limitation of previous studies, inhibiting the progress towards quantifying the effect of vegetation on riverbank roughness and consequently on the erosional and depositional processes and forms. High resolution surface measurements were obtained from a part of the riverbank of the River Lugg, with the use of Terrestrial Laser Scanning (TLS). From the 3D point cloud data, Digital Terrain (DTM) and Digital Surface (DSM) models were created, from which the roughness metrics, under the presence and absence of vegetation, were extracted, along four cross sections. Statistical analysis of the roughness metrics reveals that the presence of vegetation has a significant effect on the roughness of the bank. Moreover, a ratio of the form drag stress was calculated, indicating that the present vegetation increases the form drag stress by 57 to 95 %. The increased values of the form drag will in turn limit the values of the skin drag and consequently control the bank erosion rates. Furthermore, the additional form drag will affect the river flow dynamics, decreasing the flow velocity and increasing the flow depth, indicating a higher flood risk potential.

Acknowledgements

It is a pleasure to thank all those who have made this thesis possible. Firstly, I would like to express my gratitude to my supervisor Professor Stephen E. Darby for his valuable guidance and encouragement throughout this study. I would also like to give special thanks to Dr Julian Leyland, who generously offered valuable help and advice, including introducing me to the fascinating field of terrestrial laser scanning. Both of them always kept their doors open. I would also like to thank Mr Liam Riddy for his valuable help during my fieldwork expedition.

A special thanks is owed to all the new friends that I made these last 22 months, both at ITC and the University of Southampton. It was a privilege to meet and work with you. I will not name you individually because it would be a very long list of names, but you know who you are!

Above all, I would like to thank my mother Konstantina and my sister Eliza for their endless love, encouragement and support.

Table of Contents

Abstract	vii
Acknowledgements	ix
List of figures	xiii
List of tables	xvii
1 Introduction	1
1.1 Background	1
1.2 Erosion Mechanisms.....	2
1.3 Partitioning of the Boundary Shear Stress.....	3
1.3.1 Regular Sequences	3
1.3.2 Irregular Sequences	7
1.4 Effects of Vegetation	9
1.5 Methods of Measurement.....	11
1.5.1 Ground Survey Methods	11
1.5.2 Remote Sensing Methods	12
1.6 Problem Statement.....	18
1.7 Research Objectives.....	19
1.7.1 General Objective.....	19
1.7.2 Specific Objectives	19
1.7.3 Research Questions	19
2 Materials and Methods	21
2.1 Area of Interest.....	21
2.1.1 Study Site	23
2.2 Methodology	25
2.2.1 Overview of the Methodology	25
2.2.2 TLS Data Acquisition	27
2.2.3 TLS Data Manual Processing	29
2.2.4 DTM/DSM Creation and Profile Extraction	32
2.2.5 Modelling in Matlab.....	37
3 Results and Analysis.....	41
3.1 Statistical Analysis.....	42
3.1.1 Histograms of the Roughness Metrics	42
3.2 Resolution Analysis.....	51
3.3 Form Drag Index (FDI)	53
4 Discussion.....	57
4.1 Optimal Scale of Measurement	57
4.2 Vegetated versus Non-Vegetated Bank Roughness	57
4.3 Criticism.....	58
4.3.1 Manual TLS Data Cleaning	58
4.3.2 Filtering Method	59
4.3.3 Modelling Approach	60
4.3.4 FDI.....	60
4.4 Recommendations	61

5 Conclusion	63
References.....	65
APPENDIX A: TLS Point Clouds	71
APPENDIX B: ArcGIS Model.....	75
APPENDIX C: DTMs and DSMs	77
APPENDIX D: Modelled Profiles	79

List of figures

Figure 1: Diagram of the plan view geometry of the modelled bank topographic roughness elements, along with the internal boundary layer, wake, and outer boundary layer regions of the flow (flow direction is left to right). The dashed line of the downstream element indicates that it is removed from the flow, with <i>uref2</i> for this element being the average squared velocity over this area. The unit “cell” from $\lambda/2$ to $3\lambda/2$ is the length over which the stresses are averaged. After Kean and Smith (2006a).....	4
Figure 2: The overlapping capabilities of geospatial technologies used to characterise fluvial systems. The necessary survey density refers to the minimum number of observations required to characterise each landscape scale. The ability of terrestrial laser scanning to derive information to parameterize the fluvial system from grain-to-reach within one single data set is demonstrated in the figure. Reproduced from Brasington et al. (2012).	13
Figure 3: Basic principles of TLS measurement; combination of measured range and scan angle provides the 3D coordinates of the target within an arbitrary three dimensional system, after Lemmens (2011).	14
Figure 4: Types of TLS instruments: Optech ILRIS 3D, window-like scan system (left); RIEGL VZ-6000, panoramic with a polygonal wheel (centre); Leica ScanStation C10, with a Palmer scan system (right).....	15
Figure 5: River Wye with its two most important tributaries; the River Lugg and River Monnow. Reproduced from Jarvie et al. (2005)	21
Figure 6: Catchment of the River Lugg (map provided from prof. S.E. Darby, personal communication, 2013)	22
Figure 7: Aerial view of the study site as captured from Google Earth.....	23
Figure 8: Part of the outer bank of River Lugg on the study site. The flow depth was of approximately 1 m, keeping the lower part of the riverbank submerged.	24
Figure 9: Annual hydrograph of the River Lugg for 2011, based on the gauging station Lugg at Luggwardine – code 5503. The lowest flows are observed in September and October while the highest ones from December to February, this figure is reproduced from the Centre for Ecology & Hydrology (2013).	24
Figure 10: Flowchart showing the general steps of the followed methodology	26
Figure 11: Leica ScanStation C10 (left) and Leica HDS (6’ circular tilt and turn) target (right), mounted on tripods.	27

Figure 12: Maps showing the three scanning positions as well as the location of the targets.28

Figure 13: Part of the panoramic image taken with the camera that is built in the Leica ScanStation C10 laser scanner.29

Figure 14: Top down view showing the different steps of cleaning and partitioning of the point cloud data. a) The original point cloud, b) the point cloud after the removal of the points lying outside the area of interest, c) the two subsequent point clouds, the points representing the riverbank are in orange colour and the ones representing the lower, rigid parts of the vegetation are in green colour. The correctly reoriented axes are also presented on the bottom left of the figure. Detailed figures showing the 3D point cloud data are also presented in Appendix A.31

Figure 15: Graphical example of the filtering process and DTM creation. a) Part of the original point cloud, b) the derived raster c) the new points derived from the raster, d) DTM based on the triangulation of the points from c.33

Figure 16: Subset of the created DTM after the application of filters of different unit cell size; a) 1 cm, b) 5 cm, c) 10 cm and d) 15 cm. The level of detail decreases as the unit cell size becomes larger; however, larger cell sizes filter out points representing the grass more effectively. The cross sections used to extract the profiles are also presented; the vertical distance between two subsequent cross sections is 0.25 m.34

Figure 17: Graphical example of the filtering process and DSM creation. a) Subset of the original point cloud, b) the derived raster, the unit cell size is 1x1 cm and the cell value is equal with the mean y value of the corresponding points, c) the new points derived from the raster, d) the points of c merged with the points derived from the raster created during the DTM creation (e.g. Figure 15c), e) rasterization of the points, the cell size is 1x1 cm and the cell value is equal to the minimum y value of the corresponding points, f) points derived from the previous raster, g) final DSM of the riverbank in a TIN format.36

Figure 18: Subset of the created DTM after the application of filters of different unit cell size; a) 1 cm, b) 5 cm, c) 10 cm and d) 15 cm. The level of detail decreases as the unit cell size becomes larger; however, larger cell sizes filter out points corresponding to grass more effectively. The cross sections used to extract the profiles are also presented. The vertical distance between two subsequent cross sections is 0.25 m.37

Figure 19: Modelled profiles of the cross section S2 from the 5cm resolution of the DTM (I) and the DSM (II). On the top panel a subset of the profile is presented, showing the points that were selected by the user. On the middle panel the original profile is presented with

the blue line and the detrended profile with the green one. The bottom panel is showing the original profile with blue points, the Gaussian fit with the red line and the calculated residuals with green points.....39

Figure 20: Histograms representing the distributions of the roughness metrics and their important combinations, extracted from the profiles of the DTM and the DSM at 1 cm resolution. The vertical lines and numbers at the top right corner of each histogram correspond to the 88th percentiles of the distributions.44

Figure 21: Histograms representing the distributions of the roughness metrics and their important combinations, extracted from the profiles of the DTM and the DSM at 5 cm resolution. The vertical lines and numbers at the top right corner of each histogram correspond to the 88th percentiles of the distributions.46

Figure 22: Histograms representing the distributions of the roughness metrics and their important combinations, extracted from the profiles of the DTM and the DSM at 10 cm resolution. The vertical lines and numbers at the top right corner of each histogram correspond to the 88th percentiles of the distributions.48

Figure 23: Histograms representing the distributions of the roughness metrics and their important combinations, extracted from the profiles of the DTM and the DSM at 15 cm resolution. The vertical lines and numbers at the top right corner of each histogram correspond to the 88th percentiles of the distributions.50

Figure 24: Variations of λ , H , σ and Z_{0sf} as a function of the DTMs' resolution52

Figure 25: Variations of λ , H , σ and Z_{0sf} as a function of the DSMs' resolution52

Figure 26: The FDI as it was calculated based on the regularised values averaged for the total surveyed reach that were derived from the models of different spatial resolutions.....54

Figure 27: The original TLS 3D point cloud data; a) side view, b) top down view, c) front view..... 72

Figure 28: The cleaned TLS 3D point cloud data; a) side view, b) top down view, c) front view..... 73

Figure 29: The final TLS data after their partitioning into two subsequent point clouds. The points representing the riverbank are in orange and the points representing the vegetation stems are in green colour a) side view, b) top down view, c) front view74

Figure 30: Model created in ArcGIS model builder for the filtering of the point clouds, the creation of the DTMs and DSMs, as well as the extraction and exporting of the profiles.76

Figure 31: DTMs and DSMs of the riverbank in TIN format after the application of filters of different unit cell size. A) DTM 1cm, b) DSM 1

cm, c) DTM 5 cm, d) DSM 5 cm, e) DTM 10 cm, f) DSM 10 cm, g) DTM 15 cm, h) DSM 15 cm.	78
Figure 32: Modelled profiles of the cross section S1 from the 1 cm resolution of the DTM (I) and the DSM (II).	80
Figure 33: Modelled profiles of the cross section S2 from the 1 cm resolution of the DTM (I) and the DSM (II).	81
Figure 34: Modelled profiles of the cross section S3 from the 1 cm resolution of the DTM (I) and the DSM (II).	82
Figure 35: Modelled profiles of the cross section S4 from the 1 cm resolution of the DTM (I) and the DSM (II).	83
Figure 36: Modelled profiles of the cross section S1 from the 5 cm resolution of the DTM (I) and the DSM (II).	84
Figure 37: Modelled profiles of the cross section S2 from the 5 cm resolution of the DTM (I) and the DSM (II).	85
Figure 38: Modelled profiles of the cross section S3 from the 5 cm resolution of the DTM (I) and the DSM (II).	86
Figure 39: Modelled profiles of the cross section S4 from the 5 cm resolution of the DTM (I) and the DSM (II).	87
Figure 40: Modelled profiles of the cross section S1 from the 10 cm resolution of the DTM (I) and the DSM (II).	88
Figure 41: Modelled profiles of the cross section S2 from the 10 cm resolution of the DTM (I) and the DSM (II).	89
Figure 42: Modelled profiles of the cross section S3 from the 10 cm resolution of the DTM (I) and the DSM (II).	90
Figure 43: Modelled profiles of the cross section S4 from the 10 cm resolution of the DTM (I) and the DSM (II).	91
Figure 44: Modelled profiles of the cross section S1 from the 15 cm resolution of the DTM (I) and the DSM (II).	92
Figure 45: Modelled profiles of the cross section S2 from the 15 cm resolution of the DTM (I) and the DSM (II).	93
Figure 46: Modelled profiles of the cross section S3 from the 15 cm resolution of the DTM (I) and the DSM (II).	94
Figure 47: Modelled profiles of the cross section S4 from the 15 cm resolution of the DTM (I) and the DSM (II).	95

List of tables

Table 1: The extracted roughness metrics from the ten first roughness elements along the cross section S2 of the 5 cm DTM of the riverbank. Full data tables presenting the extracted roughness metrics are available for download via: <https://www.dropbox.com/sh/zhoflfka387qkff/EOSFRp0A6P>41

Table 2: The extracted roughness metrics from the ten first roughness elements along the cross section S2 of the 5 cm DSM of the riverbank. Full data tables presenting the extracted roughness metrics are available for download via: <https://www.dropbox.com/sh/zhoflfka387qkff/EOSFRp0A6P>42

1 Introduction

1.1 Background

The erosion of riverbanks is one of the most important processes in fluvial dynamics, with the resultant loss of land affecting a number of physical, environmental and socio-economic issues (Darby et al., 2007). Erosion of bank toe materials can lead to mass wasting under the influence of gravity, and therefore to riverbank retreat (Darby et al., 2010). Even small rates of erosion, in rivers flowing through populated areas, can present hazards to agriculture, built infrastructure and navigation (Rinaldi and Darby, 2007). For example, according to Hossain (1993), in the village of Pach Baroil in Bangladesh, over the period between 1979 and 1989, 20% of farmlands were lost due to riverbank erosion, which in turn resulted in a loss of more than 50% of crop income, affecting 45% of all households. Furthermore, in the United States it is estimated that riverbanks with a total length of 227 000 km require protection from erosion. The cost of protecting these riverbanks was estimated in 1981 to be about \$1 billion (US Army Corps of Engineers, 1983 cited in Darby et al., 2000)

Moreover, the sedimentary materials produced by bank erosion processes can lead to increased sedimentation downstream. It is estimated that materials originating from bank-eroded sediments can contribute up to 80% of the total sediment budget in the case of incised channels; however this contribution is lower in the case of low-energy rivers, such as the ones found in the UK (Darby et al., 2007). The increased sedimentation resulting from bank-derived sediment loads may in turn lead to alterations of the aquatic habitat, including suffocation of bottom-dwelling organisms and fish eggs and reductions of water quality, the latter of which can interfere with drinking water treatment processes, as well as the recreational use of rivers (United States Environmental Protection Agency, 2000).

Vegetation has been shown to affect fluid flow dynamics (Thorne and Furbish, 1995, Darby, 1999, Griffin and Smith, 2004, Griffin et al., 2005). This has a strong potential effect on the sediment transport capacity and consequently on the erosional and depositional processes and forms.

1.2 Erosion Mechanisms

Many processes contribute to riverbank erosion, such as weathering of the bank material and direct removal of sediments due to shear stresses exerted by the water flow, as well as mass wasting, triggered by erosion of the bank toe material and the gravitational influence (Amiri-Tokaldany et al., 2003).

According to Xia et al. (2008), the composition of the soil (e.g. clay content), as well as the mechanical properties of the banks of a river, are highly related to the process of riverbank erosion. Knapen et al. (2006) identify two components controlling the resistance of soils to hydraulic erosion, the erodibility coefficient (k) and the critical shear stress (τ_{cr}). These components are independent of each other, and affected by different soil and environmental properties. Therefore, in order to estimate the resistance of the soil against the erosion triggered by concentrated flow, both components need to be considered (Knapen et al., 2006).

Quantification of the rate of hydraulic erosion of riverbanks in most cases is achieved by the use of an excess shear stress formula such as (Partheniades, 1965; Arulanandan, 1980 cited in Darby et al., 2010)

$$\varepsilon = k(\tau_{sf} - \tau_c)^\alpha \quad (1)$$

where ε (m/s) is the rate of the fluvial bank erosion per unit time and unit bank area, k (m^2s/kg) and τ_c (Pa) are the erodibility parameters, namely the bank erodibility coefficient and critical shear stress, respectively, τ_{sf} (Pa) is the skin drag component of the boundary shear stress and α (dimensionless) is an empirically derived exponent which in bank erosion studies is often assumed to take the value of 1 (Rinaldi and Darby, 2007).

According to Smith and McLean (1977), the boundary shear stress (τ_T) has two components, skin drag (τ_{sf}) and form drag (τ_d).

$$\tau_T = \tau_{sf} + \tau_d \quad (2)$$

The former is the result of the friction between the flowing water and the surface of the channel while, the latter is the outcome of pressure forces that are acting on the surfaces of large-scale elements that protrude into the flow (Kean and Smith, 2006a). These roughness elements are the outcome of erosion and slumping of bank sediment and/or they may also be related to the presence of vegetation, such

as roots or grass sods protruding into the flow (Kean and Smith, 2006a), and they affect the geometry of the riverbank and consequently the flow characteristics of the river. This is due to the fact that a bend's evolution is being constantly affected by the geometry of the neighbouring bends both upstream and downstream, which are also evolving constantly (Thorne and Furbish, 1995). The former occurs due to the direct influence of the bend's geometry on the flow conditions downstream and the latter due to backwater effects, triggered by the downstream bend, which may affect the upstream flow characteristics (Smith and McLean, 1984).

Meile et al. (2011), after experiments that they conducted using flumes under steady flow conditions, suggest that the effect of the roughness elements in the flow becomes apparent when their roughness height becomes relatively large in comparison to the flow depth (i.e. when the roughness height approaches the order of magnitude of the flow depth).

1.3 Partitioning of the Boundary Shear Stress

Partitioning of the boundary shear stress into skin drag and form drag is critical in bank erosion studies, since of these two components only the skin drag (τ_{sf}) is related to riverbank erosion (Smith and McLean, 1977), as shown in equation (1), but it is the form drag (τ_d) that seems to be the dominant component of equation (2) (Thorne and Furbish, 1995, Darby et al., 2010). This means that riverbanks which have very high form roughness would tend to be associated with limited erosion rates (Darby et al., 2010).

Kean and Smith published two interrelated papers (Kean and Smith, 2006a, 2006b), in which they developed an analytical model that allows the partitioning of the boundary shear stress into its skin drag (τ_{sf}) and form drag (τ_d) components. In the first paper Kean and Smith (2006a) describe the methods of partitioning the boundary shear stress in the case of a sequence of identical, evenly spaced, topographic elements (regular sequence), while in their companion paper (Kean and Smith, 2006b) they expand their methods to cover the cases of sequences consisted of topographic elements with random geometrical characteristics (irregular sequence).

1.3.1 Regular Sequences

Kean and Smith (2006a) use a formula to define the drag stress (F) of an individual roughness element in which:

$$F = \frac{1}{2} \rho C_D H B u_{ref}^2, \quad (3)$$

where ρ is the water density, H is the protrusion height of the element, B is the length of the direction perpendicular to the x and z axes (Figure 1), u_{ref} is the reference velocity and C_D is the drag coefficient of the element.

The square of the reference velocity (u_{ref}^2) is defined by Kean and Smith (2006a) as the average of the velocity that would be present if the element were removed from the flow. In a regular sequence of topographic elements the reference velocity, for each element, is affected by the wake induced by the upstream elements, as well as a growing internal boundary layer on the wall that begins on the reattachment point (R) (Figure 1) of the separation zone on the upstream form. Therefore the reference velocity is affected by three adjacent, individual regions; an internal boundary region, a wake region and an outer boundary layer region, and the flow velocity fields have to be individually determined for each one of these regions in order for the reference velocity to be calculated.

The model of Kean and Smith (2006a) follows the same approach used by Smith and McLean (1977) and McLean and Smith (1986) where the velocity field is estimated for each region individually, followed by joining all three regions by the use of matching conditions. This is carried out under the assumption that the geometry of the topographic elements can be approximated by undulations of Gaussian shape (Darby et al., 2010).

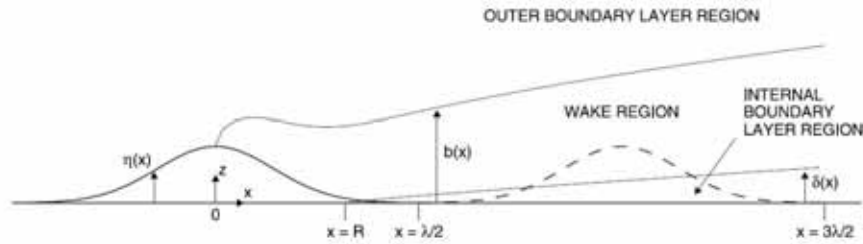


Figure 1: Diagram of the plan view geometry of the modelled bank topographic roughness elements, along with the internal boundary layer, wake, and outer boundary layer regions of the flow (flow direction is left to right). The dashed line of the downstream element indicates that it is removed from the flow, with u_{ref}^2 for this element being the average squared velocity over this area. The unit "cell" from $\lambda/2$ to $3\lambda/2$ is the length over which the stresses are averaged. After Kean and Smith (2006a)

1.3.1.1 Internal Boundary Layer

Kean and Smith (2006a) define the velocity within the internal boundary layer using the law of the wall

$$u = \frac{u_{*IBL}}{\kappa} \ln \frac{z}{z_{0SF}}, \quad (4)$$

where κ is von Karman's constant (equal to 0.408), z is the distance away from the boundary, z_{0SF} is the local roughness height of the boundary without the topographic elements and u_{*IBL} is the shear velocity inside the boundary layer which is equal to $\sqrt{\tau_{IBL}/\rho} \approx \sqrt{\tau_{SF}/\rho}$, where τ_{IBL} is the local skin friction shear stress that would be present if the object were removed from the flow and is similar to the actual skin friction shear stress acting on the surface of the roughness element (τ_{SF}).

1.3.1.2 Outer Boundary Layer

Similarly to the region of the internal boundary layer, the flow in the outer boundary layer region also follows the law of the wall

$$u = \frac{u_{*T}}{\kappa} \ln \frac{z}{z_{0T}}, \quad (5)$$

where $u_{*T} = \sqrt{\tau_T/\rho}$ and z_{0T} is the local roughness height due to skin friction and form drag.

1.3.1.3 Wake Region

Schlichting's far-field wake solution is used for the wake region (Schlichting, 1979 cited in Kean and Smith, 2006a) in which

$$u = u_b \left[1 - g(x) f \left(\frac{z-\eta}{b} \right) \right], \quad (6)$$

where according to Kean and Smith (2006a):

$$g(x) = A_2 \left(\frac{x+x_0}{c_{DH}} \right), \quad (7)$$

and

$$f \left(\frac{z-\eta}{b} \right) = \left[1 - \left(\frac{z-\eta}{b} \right)^{3/2} \right]^2, \quad (8)$$

where x is the distance downstream of the centre of the element producing the wake, z is the distance away from the reference level of the roughness elements $z = \eta$ is the surface of the boundary, u_b is the velocity at the top of the wake, x_0 is the virtual origin which according to Kean and Smith is equal to zero and b is the wake thickness given by (Kean and Smith, 2006a):

$$b = 2A_1 C_D H \left(\frac{x+x_0}{C_D H} \right)^{1/2}, \quad (9)$$

where A_1 and A_2 are constants set equal to $\sqrt{10\beta}$ and $\sqrt{20}/(18\beta)$, respectively with β being a constant that sets the value of the eddy viscosity within the wake and according to Kean and Smith (2006a), based on the flume experiments of Hopson (1999), is given by:

$$\beta = 0.226 \left[1 - \exp \left(-0.353 \frac{\lambda}{H} \right) \right], \quad (10)$$

where λ is the distance between two topographic elements (Figure 1).

1.3.1.4 Matching Conditions

In the next step Kean and Smith (2006a) apply the matching conditions between the Internal Boundary Layer and the Wake Region and between the Wake Region and the Outer Boundary Layer, which enables the identification of the velocity field, $u(x, z)$, that would be present if the topographic element were removed from the flow. In that way they define the reference velocity as:

$$u_{ref}^2 = \frac{1}{A} \int_A u^2(x, z) dA. \quad (11)$$

In equation (11), A is the plan view area of the topographic element and, since the shape of the elements is approximated as Gaussian, it is given by:

$$A = H\sigma \sqrt{\pi/2} \left[\operatorname{erf} \left(\frac{x_{dn}-x_c}{\sqrt{2}\sigma} \right) - \operatorname{erf} \left(\frac{x_{up}-x_c}{\sqrt{2}\sigma} \right) \right], \quad (12)$$

where σ is the streamwise length of the element and x_{dn} , x_c and x_{up} are the positions of the downstream end, centre and upstream end of the element, respectively.

By specifying the value of the flow velocity within the outer boundary layer the total drag on the roughness element is related to the drag on the topographic element using (2). With the use of (3), under the

assumption that the topographic elements have a Gaussian shape, the drag stress can be estimated with (Darby et al., 2010):

$$\tau_d = \frac{1}{2} \rho C_D \frac{H}{\lambda} u_{ref}^2. \quad (13)$$

By expressing the average skin friction stress (τ_{sf}) as $\langle \tau_{IBL} \rangle \equiv \rho \langle u_{*IBL} \rangle^2$, where $\langle \rangle$ indicates a spatial average, the boundary shear stress (τ_T) can be expressed as:

$$\tau_T = \rho u_*^2 = \rho (\alpha_0 \langle u_{*IBL} \rangle^2) + \frac{1}{2} \rho C_D \frac{H}{\lambda} u_{ref}^2, \quad (14)$$

where α_0 is the estimate of the ratio $u_{*SF} / \langle u_{*IBL} \rangle$, which in the Kean and Smith (2006a) paper is taken to be 1. Since τ_{sf} typically is an order of magnitude less than τ_d , the error of this approximation is minimal (Kean and Smith, 2006a).

Therefore (14) can be written as:

$$\tau_T = \rho \langle u_{*IBL} \rangle^2 + \frac{1}{2} \rho C_D \frac{H}{\lambda} u_{ref}^2, \quad (15)$$

For the drag coefficient (C_D) Kean and Smith (2006a), based on the experimental data of Hopson (1999), suggest an empirical formula

$$C_D = 1.79 \exp\left(-0.77 \frac{\sigma}{H}\right). \quad (16)$$

Based on the above, it is evident that for the model to work, the geometrical characteristics of the topographic element (H , σ , λ) as well as an estimated value of the z_{0SF} and the flow velocity within the outer boundary layer (u_{out}) at a known distance from the boundary (z_{crit}) all need to be specified (Darby et al., 2010).

1.3.2 Irregular Sequences

In their companion paper Kean and Smith (2006b) expand their analytical model to accommodate the case of an irregular sequence of roughness elements (i.e. random geometrical characteristics, as well as random spacing between the roughness elements).

As previously discussed for the case of regular sequences, one of the factors affecting the reference velocity is the flow velocity within the wake region. However, the extent of the wake region is affected by the geometrical characteristics of the topographic element that produces it. For example a large roughness element downstream of a

small one will not be drastically affected by the wake region of its upstream, small, roughness element, since a large part of it will be above the wake created by the small element upstream. On the contrary, a small topographic element downstream of a large one will be heavily affected by the wake that is produced by the large element. Therefore in the case of an irregular sequence, the relative location of an individual element, within the sequence, as well as the geometric characteristics of the elements upstream, drastically affect its reference velocity (Kean and Smith, 2006b).

Kean and Smith (2006b), differentiate the meaning of two variables that were introduced in the modelling of a regular sequence. In the case of an irregular sequence, λ is no longer the distance between the crests of two sequentially roughness elements, but it is defined as the distance between the intersection of the fitted Gaussian curve of the element with the fitted Gaussian curve of the next element that lies upstream. Moreover, since λ and H have different values for each roughness element, the value of β (which, according to (10), is a function of λ and H) has to be defined for each individual roughness element in the sequence. For each individual topographic element, in the calculation of β the protrusion height (H) of the upstream element must be used.

After experimentation with different configurations of a set of four types of elements and comparison of the flow for each configuration, Kean and Smith (2006b) found that the form drag on each element is affected by the position of the element within the sequence. However, the average stress over the set shows relatively little variability among different configurations. This is mainly because the wake that is produced by an element upstream affects the element that lies immediately downstream, but the effect on the next element that lies further downstream is minor (Kean and Smith, 2006b).

Kean and Smith (2006b) also suggest that for each irregular sequence of roughness elements an equivalent regular one exists that will produce the same spatially averaged flow velocity. However, it is very difficult to specify the geometry for the equivalent regular sequence, since this geometry is not unique. Nevertheless, after empirical analysis Kean and Smith (2006b) show that an equivalent regular surface can be derived using the approximation:

$$\begin{aligned} H_{reg} &= H_{88} \\ \sigma_{reg} &= \sigma_{88} , \\ \lambda_{reg} &= 6H_{88} \end{aligned} \tag{17}$$

where H_{reg} , σ_{reg} , λ_{reg} are the geometrical characteristics for the equivalent regular sequence and H_{88} , σ_{88} are the 88th percentiles of the distributions of H and σ for the irregular sequence.

1.4 Effects of Vegetation

The presence of vegetation on riverbanks has an ambiguous effect on the bank stability and consequently on the erosion rates. Vegetation may promote sediment instability through tree collapsing and grass growth inhibiting (Murgatroyd and Ternan, 1983), as well as flooding, triggered by the increased resistance to the flow, and localised erosion (Darby, 1999). Conversely, vegetation reduces the sediment moisture content by reducing infiltration and increasing evapotranspiration (Darby, 1999), vegetation roots provide reinforcement of the bank materials enhancing bank stability (Thorne and Furbish, 1995). Moreover, vegetation can also entrap and retain suspended material promoting sedimentation (Abt et al., 1994). Furthermore, vegetation elements on a riverbank play the role of roughness elements, altering the geometry of the bank and consequently influencing the flow conditions (Thorne and Furbish, 1995).

Thorne and Furbish (1995) conducted an experiment in Ocklawaha Creek, a sand-bedded stream in Northern Florida with a floodplain characterised by dense vegetation. They took flow measurements such as flow velocity and water level under the presence of natural bank vegetation. Subsequently they removed the vegetation, constructed a smooth wall along the outside bank of the river simulating smooth hydraulic conditions and obtained an identical set of measurements. Comparison of the two sets of measurements revealed that bank roughness, emanating from the presence of vegetation, alters the flow field and significantly decreases the flow velocity.

Griffin and Smith (2004) conducted an analysis on the East Plum Creek basin, south of Denver, Colorado. Extreme rainstorms occurred in the area on 16 June, 1965 which led to severe flooding, causing floodplain unravelling and extensive structural damage in parts of the river. The analysis is based on data derived from two sets of aerial photographs; the first set was obtained during May of the same year and the second one two days after the flood. This data was incorporated with field observations made in February of 2000. The data was analysed with the flow model of Smith (2004). Griffin and Smith (2004) concluded that areas covered with dense vegetation were protected from erosion, while in areas that the vegetation was

sparse or absent severe erosion occurred. Furthermore it is shown by Griffin and Smith (2004) that the form drag emanating from the dense shrubs increased the flow depth by more than a metre in comparison to the flow depths that would have occurred if vegetation was absent for the same flow discharge. Moreover calculations of the model created by Smith (2004) suggest that the flow velocities were about 40% lower and the actual boundary shear stress was reduced by three orders of magnitude due to the presence of dense vegetation (Griffin and Smith, 2004).

Griffin et al. (2005) showed that in the Rio Puerco, a tributary of the Rio Grande in New Mexico, the boundary shear stress decreased twice as much in areas with moderate to dense bank shrubs in comparison to bare areas. The Griffin et al. (2005) study was based on cross sections that were taken along the river with the use of a tape and level in order to characterise the surface characteristics of the channel, as well as plot sampling along the bank, that provided estimations of the characteristics of the vegetation which was afterwards modelled as vertical cylinders extending through the flow (Griffin et al., 2005). The results show that the boundary shear stress in the channel decreased by up to 20% due to the friction on the lateral boundaries, however in the areas covered by moderate to dense vegetation the decrease was even higher, up to 40%.

Huai et al. (2012) studied the flow on a curved open channel for which the inner bank was covered with rigid vegetation. Their study was based on laboratory measurements incorporated within a *RNG k- ϵ* model, a form of turbulence model in which the Navier-Stokes equations have been renormalized in order to take into consideration motion effects of smaller scales (Yakhot et al., 1992). From this study it was concluded that the presence of vegetation significantly decreases the stream-wise flow velocity, furthermore it provides protection to the riverbank from scour and erosion and enhances sedimentation due to decreased values of boundary shear stress (Huai et al., 2012).

Based on these previous studies, it is evident that the presence of riverbank vegetation has a strong potential effect on the form drag component of the boundary shear stress and consequently on the fluid flow dynamics and sediment transport capacity, which in turn may affect erosional and depositional processes and forms. However, quantification of that effect requires explicit calculation, based on highly detailed, precise and accurate measurements of both the topography of the riverbank and the geometrical characteristics of any vegetation that is also present. Until recently obtaining such

measurements has been problematic, due in part to a lack of suitable technology. For example, Thorne and Furbish (1995) succeeded in quantifying the characteristics of the flow field under the presence and absence of vegetation, but they did not attempt to obtain measurements that would characterise the vegetation and its effect on the form roughness. Furthermore, Griffin and Smith (2004) estimated an average roughness for the floodplain of East Plum Creek, using field observations to characterise the vegetation, but working under the assumption that the distribution of shrubs in the area is uniform. Moreover, Griffin et al. (2005) obtained cross sections of the Rio Puerco from where they derived points with an average spacing of 41 m to characterise the channel morphology. Subsequently Griffin et al. (2005) used sampling plots along the banks of the river to estimate the physical characteristics of the shrubs which they then upscaled for the total area covered by vegetation.

1.5 Methods of Measurement

Several methods of obtaining surface characteristics have been developed through years of research. These methods can be grouped into two fundamental categories; traditional methods based on ground surveying and methods based on remote sensing.

1.5.1 Ground Survey Methods

The methods that fall under this category have the advantages of simplicity, their straightforward approach and require relatively simple post-processing of the obtained data. However, they also have the disadvantages of being labour intensive, being subject to blunders originating from human errors and comprise a trade-off between the duration of the survey and the spatial resolution of the obtained data (Brasington et al., 2003).

Ground survey methods have been used in many previous studies. For example, Brasington et al. (2003) conducted a 14-days GPS survey of the River Feshie covering an area of 300 x 80 m. The collected data consisted of 29 000 observations with an average density of 1.7 pts/m². Griffin et al. (2005) surveyed 49 cross sections, using GPS and a tape and level, along the Rio Puerco, New Mexico. With this method Griffin et al. (2005) derived 1957 points, with an average point spacing of 41 m. Kean and Smith (2006b) used a 9 m straight edge placed along the bank of Rio Puerco, New Mexico. Subsequently, they extracted bank profiles by measuring the distance between the straight edge and the bank of the river at 5 cm intervals.

A similar method was followed by Darby et al. (2010) on the Mekong River where, with the use of a laser range finder, they measured offsets at 0.5 to 1 m intervals along survey transects of constant elevation along the riverbank.

1.5.2 Remote Sensing Methods

Remote sensing methods, in contrast to traditional ground surveys, are capable of obtaining survey data of high resolution over large areas within a limited time. Furthermore, the semi-automated workflow, which is usually followed in such methods, significantly reduces the required labour as well as the risk of human errors. However, data obtained by remote sensing, in most cases, require significant post-processing and can be subject to other types of errors which will be further analysed in the following section.

Light detection and ranging (LIDAR) is one of the most common methods of surveying natural surfaces and extracting digital terrain (DTMs) or surface (DSMs) models, the other being digital photogrammetry (Schenk, 1999). Both of these methods can be airborne, conducted from a platform mounted on a plane or helicopter, or terrestrial conducted from ground level.

Figure 2, reproduced from Brasington et al. (2012), demonstrates the capabilities of different survey methods relating them with the appropriate scale of measurement required for different types of landforms of a fluvial system. As shown here, a single TLS measurement can accommodate a plethora of studies from a particle to a reach scale.

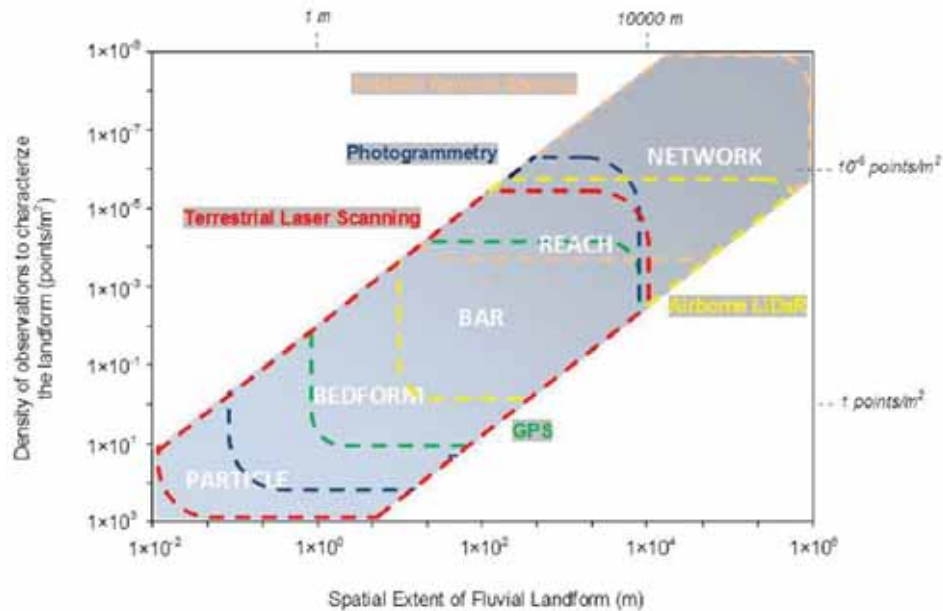


Figure 2: The overlapping capabilities of geospatial technologies used to characterise fluvial systems. The necessary survey density refers to the minimum number of observations required to characterise each landscape scale. The ability of terrestrial laser scanning to derive information to parameterize the fluvial system from grain-to-reach within one single data set is demonstrated in the figure. Reproduced from Brasington et al. (2012).

1.5.2.1 Terrestrial Laser Scanning

Terrestrial Laser Scanning (TLS), as the method of ground based LIDAR is most commonly called, is an active, contactless method of data acquisition. Active means that it does not rely on any form of natural light, but instead, the scanner itself emits electromagnetic radiation (Lemmens, 2011). The principles that TLS is based on are essentially the same that apply on airborne LIDAR (Hodge et al., 2009b).

There are two methods of measurement that are used in laser scanning technology; time-of-flight and phase measurement (Beraldin et al., 2010). Time-of-flight is based on the propagation velocity of light pulses, which is constant for a given medium. Therefore, the distance from the scanner to the target can be calculated by measuring the time that is needed for a light pulse to travel from the source to the target and back to the sensor (Beraldin et al., 2010). Phase measurement is based on continuous waves that are emitted from the laser source and subsequently collected on the

sensor after they have been reflected from the target's surface. The calculation of the range between the scanner and the target is achieved by comparing the phase difference of the waves of the emitted and collected laser beam (Beraldin et al., 2010). Measuring the angle of the laser beam, in conjunction with the measured range between the scanner and the target, provides the way to estimate the coordinates of the target within an arbitrary three dimensional system (Hodge, 2010) (Figure 3). This procedure is fully automated and repeated at very high speed, enabling the measurement of millions of points of a scene within limited amounts of time, resulting in a dense cloud of points (Lemmens, 2011). If the coordinates and the orientation of the scanner are defined within a coordinate system (e.g. with the use of D-GPS), then the point clouds can also be registered in the same coordinate system with a mm to cm accuracy (Antonarakis et al., 2009).

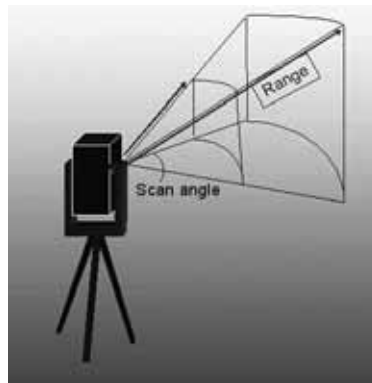


Figure 3: Basic principles of TLS measurement; combination of measured range and scan angle provides the 3D coordinates of the target within an arbitrary three dimensional system, after Lemmens (2011).

Terrestrial laser scanners can be classified into window-like and panoramic. The former have a fixed rectangular field of view, much like a conventional camera, while the latter have a field of view of 360° in the horizontal axes and typically $80-90^\circ$ on the vertical one, this is achieved by the use of a polygonal wheel rotating on the direction of the vertical axis (Beraldin et al., 2010). By replacing the polygonal wheel with a Palmer scan system the field of view of the vertical direction can be expanded in such a way that the only limitation is the self-occlusions by the scanner itself and the tripod that it is mounted on (Figure 4) (Beraldin et al., 2010).



Figure 4: Types of TLS instruments: Optech ILRIS 3D, window-like scan system (left); RIEGL VZ-6000, panoramic with a polygonal wheel (centre); Leica ScanStation C10, with a Palmer scan system (right).

The range measurement of a scanner varies according to the specifications of the instrument. There are short range scanners with a range of less than 25 m, medium range scanners with a range up to 250 m, and long range ones that can survey targets over distances longer than 250 m (Lemmens, 2011). The spatial resolution of the TLS, which defines the level of detail that can be captured by the instrument, is a combination of the sampling interval (i.e. minimum spacing between two subsequent points) and the footprint size of the laser beam (Hodge et al., 2009a). Both the sampling interval and the laser footprint size, and subsequently the spatial resolution of the obtained point cloud, are affected by the distance between the scanner and the surveyed surface (Lemmens, 2011).

In addition to the three dimensional position of points, a TLS will also record a value of the reflection intensity for each point (Lemmens, 2011). When the laser beam reaches the surveyed surface it might interact with it in three different ways; reflected, absorbed or transmitted (Rees, 2001). The intensity value of the echo of the emitted pulse depends on the distance between the scanner and the target, the angle of incidence and the target's reflectance properties (Lee et al., 2010). In that way, the intensity value for each point on the point cloud can be a potential source of information that can be used to discriminate between different types of objects.

Moreover, most TLS instruments have a built-in digital camera, or are equipped with a mount that can hold an external one (Lemmens, 2011). This provides the ability to capture a panoramic image of the scene before scanning. The colours from the panoramic image can afterwards be used for colouring the point cloud, thus assisting the point interpretation (Beraldin et al., 2010).

Furthermore, TLS is capable of surveying a scene from different positions, therefore, providing multiple point clouds representing the same surface from different angles. The individual point clouds can be

combined afterwards, as long as there are enough tie points in all clouds, thereby providing a three dimensional representation of the scene and preventing possible occlusions created by the intrusion of objects between the surveyed surface and the scanner (Antonarakis et al., 2009).

After the TLS data have been obtained and erroneous points have been filtered out (see following section), the 3D point cloud data can be transformed to 2.5D surfaces such as DTMs or DSMs. The difference between a 3D and a 2.5D surface is that on a 2.5D surface every x and y location has one unique elevation (Hodge et al., 2009a). The most common method of achieving the extraction of 2.5D surfaces from point clouds is by creating a Triangular Irregular Network (TIN) (Vosselman and Maas, 2010). The TIN can be further processed and DTMs or DSMs in a raster or grid format can be derived (Briese, 2010).

Errors in TLS data

TLS point cloud data may contain errors that can be classified into random, systematic and gross errors (Hodge et al., 2009b). Random errors appear on repeated measurements that are conducted under the same conditions and indicate the methodological as well as the instrument's precision. Systematic errors are defined as the difference between the real value and the measured one, reflecting the accuracy of the measurement. Gross errors are the outcome of human errors or malfunctions of the instrument (Hodge et al., 2009b).

The reflectivity of the surveyed surface, the view angle of the surveyed surface from the scanning position, and hardware design of the instrument are the most common sources of errors (Lichti, 2007). Errors caused by hardware design are related to the precision in which the sensor records the time-of-flight and angle of the laser beam (Hodge et al., 2009b). Recorded time-of-flight may also be affected by the reflectivity of the surveyed surface. As explained earlier, a laser beam emitted from the scanner hits the surveyed surface and returns to the sensor. However, the sensor has a threshold and it records the location of the point only after it receives a certain amount of light. Therefore, a more reflective surface may reflect more light, saturating the sensor faster than a less reflective one. Consequently surfaces with higher reflectance values will produce shorter (apparent) times-of-flight and therefore shorter ranges will be recorded (Hodge et al., 2009b). Moreover, the angle of the laser beam is recorded from the centre of the footprint. However,

if light is reflected from another area within the laser footprint it may lead to systematic errors, where the recorded point has the coordinates of the centre of the laser footprint, even though the laser beam was reflected on a different area within the laser footprint (Lichti et al., 2005).

Furthermore, errors can be introduced in the process of the registration of multiple point clouds in one scene. These errors are usually related to the accidental moving or mislabelling of the targets that are used as tie-points, or to the precision that the instrument is capable of locating and recording these targets (Hodge et al., 2009b).

Comparison of TLS with other methods

TLS's high speed of data acquisition, its high levels of precision and accuracy, as well as the limited amount of human intervention which significantly decreases the required labour, the risk of human blunders as well as the underlying dangers of traditional field measurements, mean that the TLS method offers significant advantages in comparison to traditional ground survey methods. For example in the study by Brasington et al. (2003) that was previously noted, it is explained that 29 000 points with an average point density of 1.7 pts/m² were collected during a 14-days GPS survey. In comparison, TLS has the ability to collect millions of points within less than an hour and with even higher levels of precision and accuracy.

In comparison to methods of airborne remote sensing, TLS also has a potential advantage. Due to the smaller distance between the surveyed surface and the scanner, and consequently the smaller footprint size and sampling interval, TLS has the capability of obtaining data of higher spatial resolution and accuracy. Moreover, in comparison to airborne photogrammetry, TLS has a significant advantage, since according to Brasington et al. (2003) and Rumsby et al. (2008), data obtained by aerial photogrammetry have found to be less precise and accurate even than traditional ground survey methods. Furthermore, when measuring vertical surfaces, such as steep riverbanks, the oblique survey angles used in TLS provide a significant advantage in comparison to any airborne approach which would measure only the top edge of such a surface (British Geological Survey, 2012). Nevertheless, airborne approaches have the ability of covering much larger areas within a limited amount of time. This is a significant advantage of airborne approaches over TLS when there is a need for surveying very large areas. However, in such cases, TLS can still prove to be extremely useful as a complementary method of data acquisition and TLS data, collected from sample plots within the

surveyed area, may be used to upscale or validate the airborne data, an example of this method can be found in Manners et al. (2013).

In comparison to terrestrial digital photogrammetry, TLS has the advantage of directly capturing three dimensional data. Conversely, photogrammetric methods provide two dimensional data which afterwards need to be transformed into 3D (Ingensand, 2006). Furthermore, with TLS a single view angle on the surveyed surface is sufficient, while photogrammetry requires at least two images from two different angles and relies on parallax (Ingensand, 2006, Hodge et al., 2009b, Hodge, 2010). However, multiple view angles are also desirable in TLS surveys, to prevent possible occlusions which are the outcome of objects positioned between the sensor and the target (Antonarakis et al., 2009). Moreover, photogrammetric methods rely on image texture in order to create stereo images, this can be problematic in cases of images with low texture or poor quality (Hodge et al., 2009b, Hodge, 2010, Lemmens, 2011). In addition, TLS, being an active system, is not affected by ambient light conditions (Lemmens, 2011). Furthermore, TLS's lower dependency on external control, in addition to automated methods of post processing and straightforward methods of DSM and DTM creation, makes it a better alternative to terrestrial digital photogrammetry (Hodge et al., 2009b, Hodge, 2010, Lemmens, 2011). Nevertheless, TLS equipment is significantly expensive in comparison to commercial digital cameras that are usually employed in digital photogrammetric approaches. Moreover, although laser scanners are becoming more portable, they are still more difficult to carry on a daily basis due to their size, weight and the necessary peripheral equipment, such as batteries, laptops and external power sources (Lemmens, 2011).

1.6 Problem Statement

As discussed in the previous sections, the presence of vegetation on riverbanks has a potential effect on the, dominant, form drag component of the boundary shear stress. This can consequently affect the flow dynamics of a river and in turn the erosional and depositional processes and forms. However, quantification of the additional drag induced by riverbank vegetation requires explicit calculations which must be based on dense measurements, obtained with very high levels of precision and accuracy. Obtaining such measurements was problematic until recently, due to the lack of technology, which has been a limitation of previous work.

TLS has the capability of obtaining the necessary type of measurements. This, in combination with the relatively

straightforward methods of post-processing applicable in TLS data, provides the potential of incorporating topographic measurements into the hydraulic models. Thus, having an advantage over traditional methods, that are using global estimates of roughness to numerical model flow velocities (Milan, 2009).

1.7 Research Objectives

1.7.1 General Objective

The general objective of this study is to use TLS to characterise the surface terrain characteristics of vegetated and non-vegetated riverbanks. Subsequently, the methods of Kean and Smith (2006a, 2006b) will be used to extract roughness metrics representing each surveyed surface, enabling a clear quantification of the effects of vegetation on riverbank roughness.

1.7.2 Specific Objectives

- a. To derive roughness characteristics of the surveyed riverbank from 3D point cloud data obtained using TLS.
- b. To compare the roughness characteristics of vegetated versus non-vegetated riverbanks

1.7.3 Research Questions

- a. Is it possible to use 3D point cloud data in order to derive the roughness characteristics of riverbanks?
- b. What is the optimal spatial scale for such measurements?
- c. Are there significant differences in the roughness parameters between vegetated and non-vegetated riverbanks?
- d. What are the possible effects of the above mentioned differences in the fluid flow dynamics and consequently on the erosional and depositional processes and forms?

2 Materials and Methods

2.1 Area of Interest

The River Lugg is a 6th order tributary of the River Wye and one of its two most important ones, the other being the River Monnow (Figure 5) (Jarvie et al., 2005).



Figure 5: River Wye with its two most important tributaries; the River Lugg and River Monnow. Reproduced from Jarvie et al. (2005)

The River Lugg flows from Wales following a south-east course, crossing the English-Welsh border and converging with the River Wye in Herefordshire (Wade et al., 2007). Its catchment consists of both upland and lowland areas with a total extent of 1077 km² (Lazar et al., 2010) (Figure 6). The amount of precipitation within the river's catchment shows significant spatial variability. In the upper catchment (Byton) the long term mean annual precipitation is 1041

mm, while in the lower parts (Luggwardine) it is 847 mm, generating a runoff of approximately 349 mm (Wade et al., 2007). This, in conjunction with the underlying geological setting, which consists of Old Red Sandstones on the lower parts and rocks of the Silurian period in the headwaters, significantly regulates the high flow peaks, indicating the existence of an underground aquifer (Lazar et al., 2010).

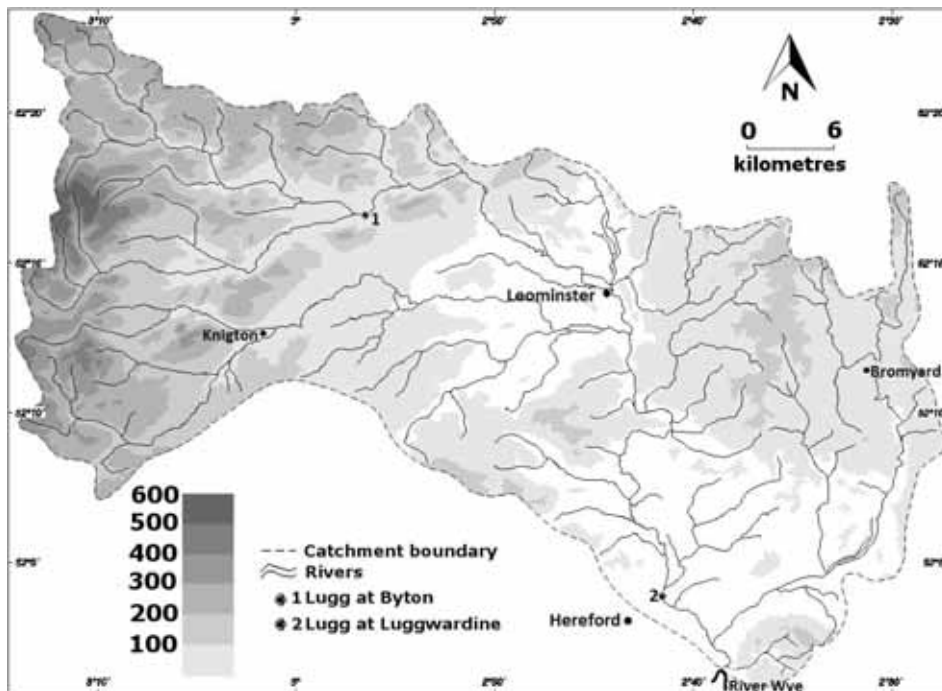


Figure 6: Catchment of the River Lugg (map provided from prof. S.E. Darby, personal communication, 2013)

In contrast to the low energy rivers located in much of the south and southeast UK, the river Lugg is characterised by riverbanks which indicate the presence of active erosional and depositional processes. The morphology of the riverbanks, which are steep and partially covered with vegetation, is the key criterion for the selection of the particular study area. Furthermore, the width of the river is relatively narrow, meaning that the scanner can be placed on one side of the river and easily survey the opposite riverbank. Moreover, there is an adequate road network in the area, providing sufficient accessibility.

The selection of this area of interest was further supported by the significant ecological importance of the river's catchment, which was characterised as an eutrophic sensitive area in 1994, due to high

concentrations of Phosphorous (Wade et al., 2007). Moreover, it was characterised as a Special Area of Conservation (SAC), due to the rich and important species of wildlife inhabiting the area, such as the Atlantic Salmon and the Brown Trout (Wade et al., 2007, Lazar et al., 2010).

2.1.1 Study Site

The study site comprises a part of a meander of the River Lugg. It is located approximately 2.5 km NE of Hereford (Figure 7); its coordinates are 521446.89 m E, 5768777.80 m N, in the Universal Transverse Mercator (UTM Zone 30 N) coordinate system.



Figure 7: Aerial view of the study site as captured from Google Earth.

The outer bank of the meander is relatively steep and covered by sparse vegetation which mostly consists of grass, shrubs and a few trees (Figure 8). The river depth at the site is approximately 2.5 m and the flow presents significant temporal variability throughout the year. As an example the annual hydrograph of 2011, based on measurements taken from the nearest gauging station (Lugg at Luggwardine; station code: 5503; located approximately 2 km SE of the study site) is presented in Figure 9. During the days of the

fieldwork expedition (13 - 14 of November, 2012) the water depth at the study site was approximately 1 m. Consequently, the lower part of the riverbank was submerged leaving exposed only the higher part with an average height of approximately 1.5 m (Figure 8).



Figure 8: Part of the outer bank of River Lugg on the study site. The flow depth was of approximately 1 m, keeping the lower part of the riverbank submerged.

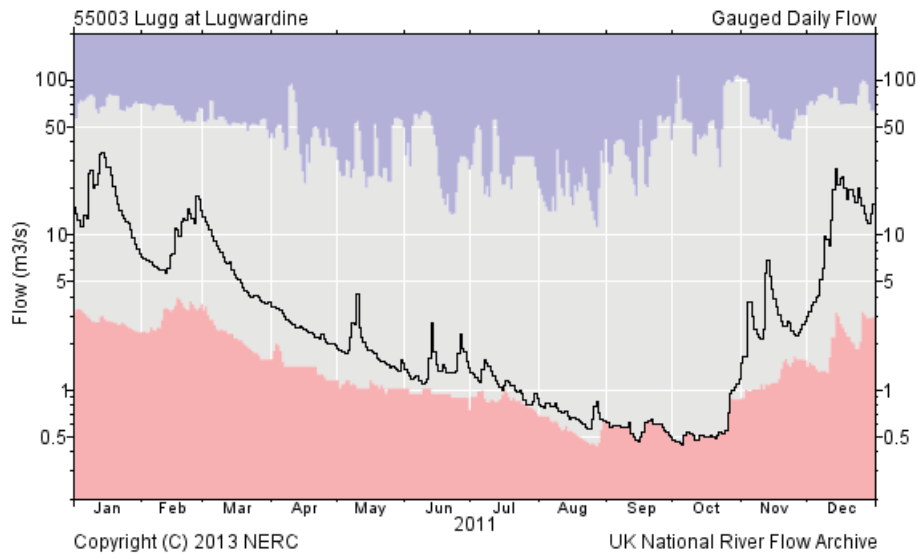


Figure 9: Annual hydrograph of the River Lugg for 2011, based on the gauging station Lugg at Luggwardine – code 5503. The lowest flows are observed in September and October while the highest ones from December to February, this figure is reproduced from the Centre for Ecology & Hydrology (2013).

2.2 Methodology

2.2.1 Overview of the Methodology

A general overview of the followed workflow is presented here, which is summarised in Figure 10. Detailed description of all the followed steps of the methodology is provided in the following sections (2.2.2 – 2.2.5).

3D point cloud data was collected from the study site using a Leica ScanStation C10 terrestrial laser scanner (see section 2.2.2). The data were initially inspected using Leica Cyclone v.7.4 and points lying outside the area of interest were manually removed. Moreover the point cloud was partitioned into two subsequent point clouds in such way that the first contained the points representing the outer bank of the river, while the second contained the points representing the lower, rigid parts, of the present vegetation. Both point clouds were exported from Cyclone in an ASCII format (section 2.2.3).

Both ASCII files were imported into ArcGIS 10.1. A file geodatabase was created and the ASCII files were converted to point feature classes. The point feature classes underwent filtering in order to remove any erroneous points, using filters of different spatial resolution. Subsequently, the points representing the vegetation elements were merged with the points representing the riverbank and a DSM was created. Furthermore, a DTM was also created, based only on the points that belonged to the riverbank. In the next step, profiles were extracted from both the DSM and DTM and were exported from ArcGIS in a text format (section 2.2.4).

The text files containing the extracted profiles were imported into Matlab. A Matlab code developed by Leyland (2012) was used to model the riverbank profiles by fitting a Gaussian curve for each one of the roughness elements. Based on the fitted curves, the model calculates the roughness metrics for each profile with and without the presence of vegetation, (section 2.2.5).

The output data from the modelling process were analysed statistically and a comparison was made between the roughness metrics of the vegetated and the non-vegetated profiles for each case. The results of the analysis are presented in Chapter 3.

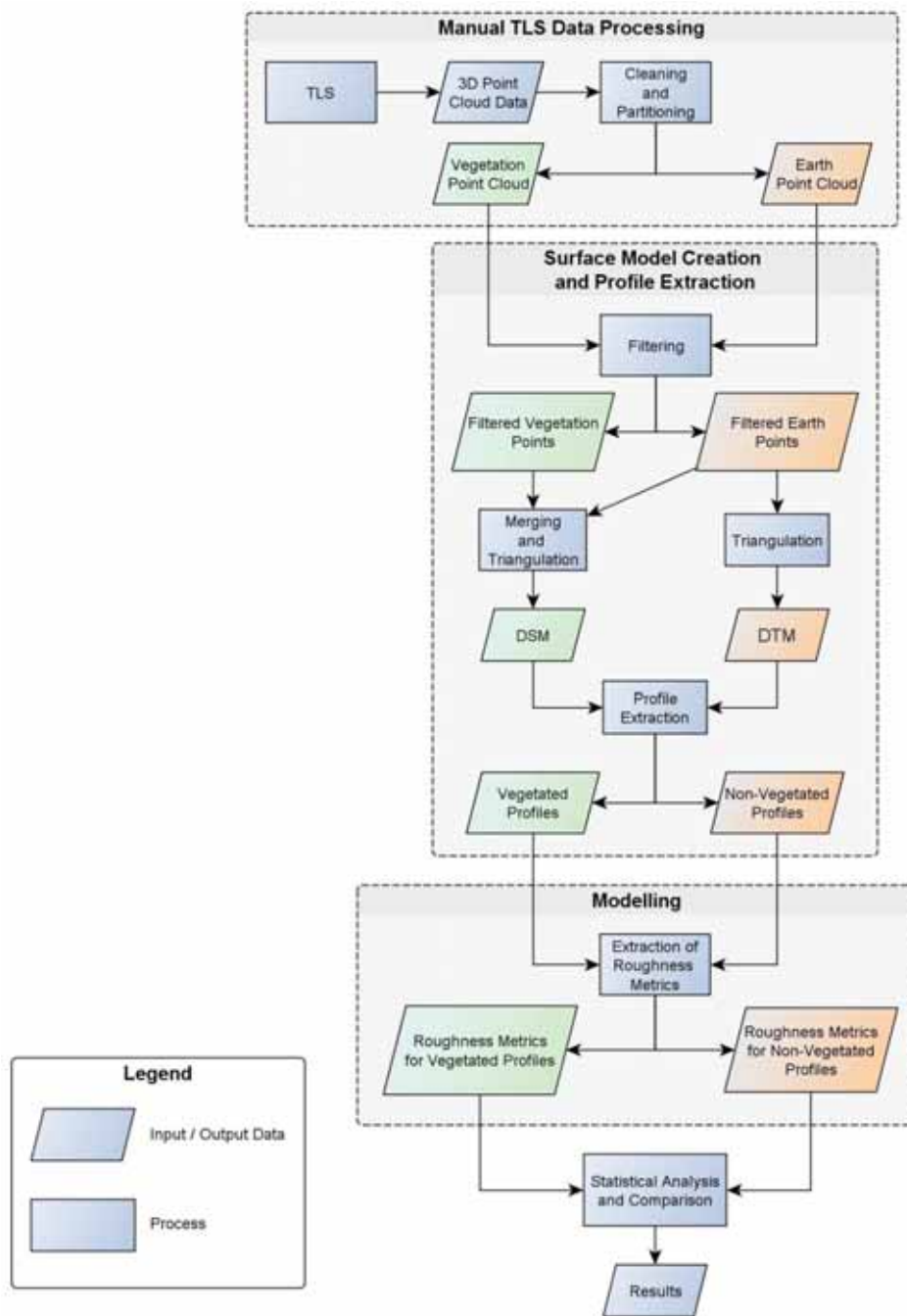


Figure 10: Flowchart showing the general steps of the followed methodology

2.2.2 TLS Data Acquisition

The required data for this study was collected during a two day period of fieldwork expedition that took place in 13 and 14 of November 2012. The River's Lugg water level at the site during this time was approximately 1 m, leaving the top part of the riverbank, with an approximate height of 1.5 m, exposed for scanning.

2.2.2.1 Instrument Deployment

A Leica ScanStation C10 scanner and four Leica HDS (6' circular tilt and turn) targets (Figure 11) were deployed in the study site, mounted on tripods.

The Leica ScanStation C10 is a pulsed, time-of-flight, terrestrial laser scanner. It has a field of view of 360° on the horizontal axis and 270° on the vertical one, and a maximum range of 300 m. It emits laser pulses with a wavelength of 532 nm (green part of the electromagnetic spectrum). It has high levels of accuracy (6 mm position, 4 mm distance and 60 μ rad angle) and the ability to collect a maximum of 50 000 pts/sec with a fully selectable point spacing (minimum point spacing < 1 mm).

The targets were placed in positions surrounding the surveyed area (Figure 12). Scanning of the targets from each scanning position provides sufficient tie points to allow the co-registration of multiple point clouds into one coordinate system. The targets remained fixed in their position throughout the survey.

The scanner was connected and operated from a laptop computer, equipped with Leica Cyclone v.7.4. A power generator was also used in order to replenish the laptop's battery charge when this was required.



Figure 11: Leica ScanStation C10 (left) and Leica HDS (6' circular tilt and turn) target (right), mounted on tripods.

2.2.2.2 Scanning

Scanning took place from three different positions (Figure 12); surveying the same area from different positions, and consequently from different angles, to minimise possible occlusions due to the intrusion of objects (e.g. tree branches) between the sensor and the surveyed surface (see also section 1.5.2.1). In this way, scanning position 2, shown in figure 12, was the main scanning position, covering the whole extent of the study site, while scanning positions 1 and 3 were used to obtain complementary data that would cover any possible occlusions.

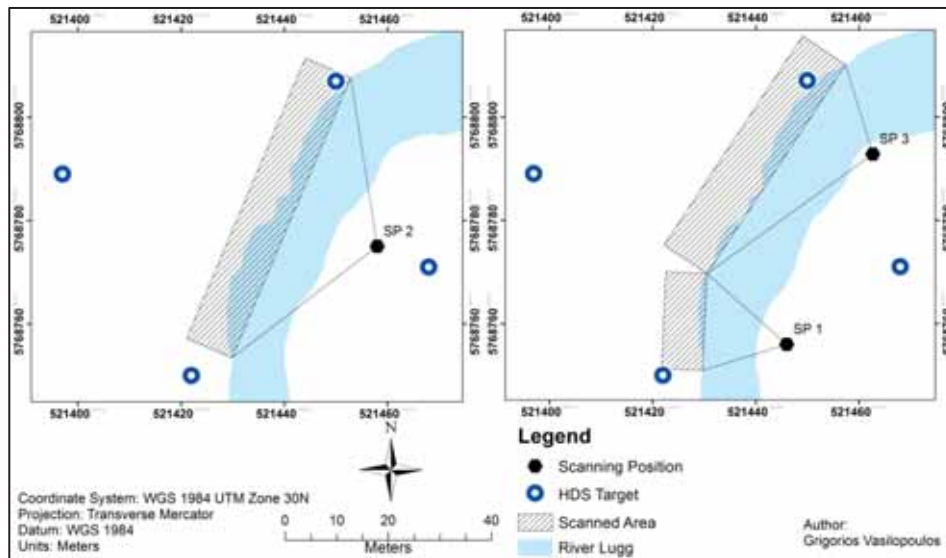


Figure 12: Maps showing the three scanning positions as well as the location of the targets.

Before scanning, a panoramic photo of the study site was taken, using the built in camera of the laser scanner (Figure 13). This significantly assists the scanning process, since the area that has to be scanned each time can be selected from the panoramic image. Furthermore, the colours of the panoramic photo can be used to colorize the points of the point cloud, assisting the point interpretation (see also section 1.5.2.1). In the next step all four HDS targets were selected from the image, scanned and their location was stored. Subsequently, the area that had to be surveyed was selected and scanned. The point spacing for the scanning was selected to be 5 mm; such point spacing can provide the detailed data required for this study, without the need for very long scanning times. Moreover,

according to the specifications of the particular scanner, the diameter of the laser footprint, for scanning distances up to 50 m, is 4.5 mm. This means that any point spacing smaller than 4.5 mm would not provide additional detail in the final dataset. Therefore, any roughness elements of a less than 5 mm scale are omitted from this study. The scanning was repeated two more times from the same position, therefore, three scans from each position were obtained. Repeating the scanning from the same position minimizes possible errors and helps to achieve a higher point density (Hodge et al., 2009a). As soon as the process was completed, the scanner was repositioned to the next scanning position and the exact same process was repeated. In that way, three ScanWorlds were created (one from each scanning position), each one containing three scan datasets of the exact same area.



Figure 13: Part of the panoramic image taken with the camera that is built in the Leica ScanStation C10 laser scanner.

2.2.3 TLS Data Manual Processing

2.2.3.1 Point Cloud Unification and Registration

The obtained TLS data were first processed using Cyclone v.7.4. As explained in section 2.2.2.2, the TLS data were organised in three ScanWorlds, one for each scanning position, and under each ScanWorld the three repeated scan datasets were stored. The first step required merging of the three repeated scan datasets into one, under each ScanWorld. This was done using Cyclone's unifying tool with the default options selected (i.e. no point cloud reduction). This process led to the creation of one scan data set under each

ScanWorld, containing all the point clouds from the three original datasets of the corresponding ScanWorld.

In the next step, the three individual ScanWorlds had to be co-registered under the same coordinate space. This should be done using the scanned targets as tie points. However, due to an error during the scanning of the targets, their position was not correctly stored in the datasets. Therefore, co-registration of the three point clouds could not be accomplished. A different approach was also attempted, according to which points that are present in at least two ScanWorlds can be identified and selected by the user as tie points for the registration of the point clouds. However, this approach led to significant errors (RMS = 1.5 cm and max = 9.8 cm).

Nevertheless, after a close inspection of the obtained data, it was realised that the point cloud stored under ScanWorld 2 was of high detail with only limited occlusions. Therefore, it was decided that the clouds stored under ScanWorlds 1 and 3 were not of critical importance and that all further analysis could be based only on the point cloud of ScanWorld 2, which contained approximately 11 million points and covered the total extent of the surveyed area, with an approximate length of 60 m.

2.2.3.2 Cleaning and Partitioning of the Point Cloud

The following step included cleaning of the point cloud from points that were lying outside the area of interest. This was done by manually selecting these points and deleting them. With this method only the points that were within the area of interest were kept (Figure 14b). Subsequently, the point cloud was partitioned into two individual model spaces. This was accomplished by selecting points and moving them into a different model space. The first model space contained only the points that were representing the bank of the river while the next one contained only points representing the lower, rigid, parts of the present vegetation (Figure 14c). The model space of the points corresponding to the riverbank contained 4 323 662 points with an average point density of 5.2 pts/cm². The model space of the points representing the vegetation elements contained 183 972 points. Since the vegetation points are concentrated only in a few locations within the total extent of the studied reach, a point density was not estimated.

Exporting the point Clouds

The point clouds were exported from Cyclone for further processing. Since the points are registered in an arbitrary coordinate system it was necessary to ensure that the axes of this coordinate system would be oriented in such a way that the point cloud would be also correctly oriented when imported in ArcGIS, in the next step. For that reason the axes were reoriented in Cyclone in such a way that the x axis was parallel to the streamwise length of the riverbank, the z axis was parallel to the riverbank's height, and the y axis was perpendicular to the other two axes, pointing towards the bank of the river (Figure 14c). After the correct orientation of the axes, the two point clouds were exported in an ASCII format that contained the x, y and z coordinates of each point.

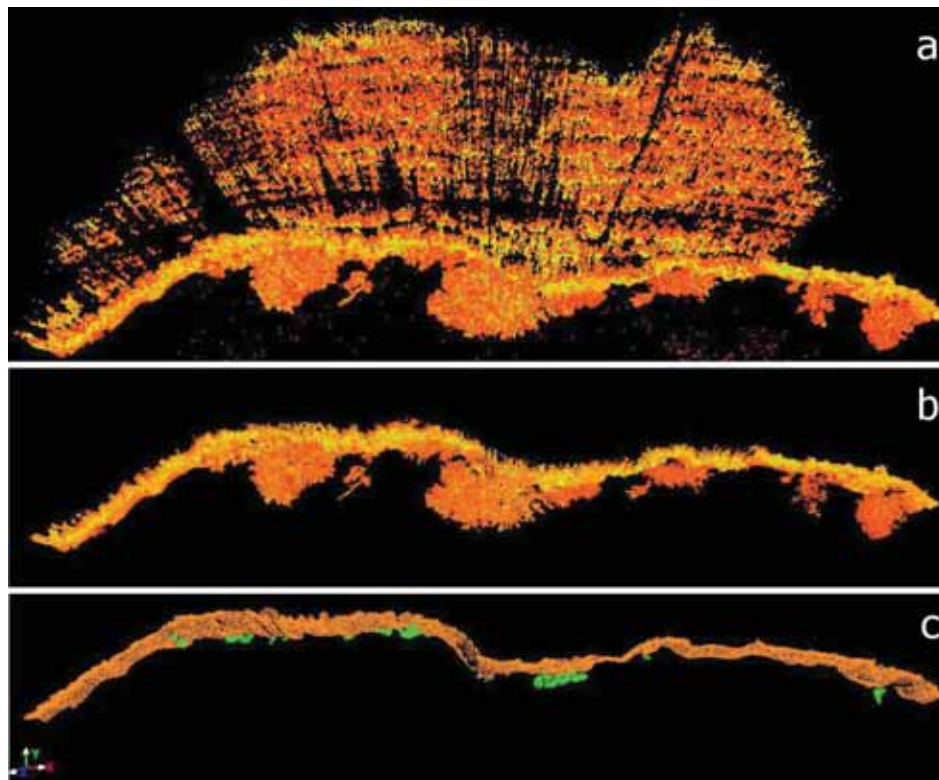


Figure 14: Top down view showing the different steps of cleaning and partitioning of the point cloud data. a) The original point cloud, b) the point cloud after the removal of the points lying outside the area of interest, c) the two subsequent point clouds, the points representing the riverbank are in orange colour and the ones representing the lower, rigid parts of the vegetation are in green colour. The correctly reoriented axes are also presented on the bottom left of the figure. Detailed figures showing the 3D point cloud data are also presented in Appendix A.

2.2.4 DTM/DSM Creation and Profile Extraction

2.2.4.1 Importing into ArcGIS and Filtering

The ASCII files, one containing the points representing the riverbank and one containing the points representing the vegetation stems, were imported into ArcGIS 10.1, converted into point feature classes and stored under a file geodatabase.

The point clouds were manually cleaned from erroneous points in Cyclone, as described in section 2.2.3.2. However, there were still points that had to be removed from the clouds, such as points representing grass lying on the surface of the riverbank. This was important since non-rigid vegetation elements will either be out washed from the flow in the case of a flood and therefore they will not affect the form drag, or they will bend, changing their angle in reference to the direction of the flow and subsequently changing the value of the form drag. Therefore, filtering of the point feature classes was required and four filters of different spatial resolution were applied, as described below.

Filtering of the riverbank, DTM creation and profile extraction

The filtering process was based on the assumption that, within a cell unit of a certain extent, there must be at least one point representing the surface of the riverbank, instead of the grass that partially covers it, and that this point will be located the furthest away from the scanner in comparison to the rest of the points within the cell unit. Therefore, the point feature class of the riverbank was rasterised, using four different raster cell sizes (i.e. 1, 5, 10 and 15 cm). In all cases the assigned value for each raster cell was selected to be equal to the maximum y value of all the points positioned within the cell, since that value would belong to the point lying the furthest away from the scanner and consequently was most likely to belong to the surface of the riverbank, than to the grass that partially covers it (Figure 15b).

Subsequently, the rasters were converted back to points, with each point being located in the middle of the corresponding raster cell and each raster cell value being assigned as the y coordinate of the corresponding point (Figure 15c). The new feature class that was created, containing the new points representing the bare riverbank, was used to construct the Digital Terrain Model (DTM) of the riverbank in a Triangular Irregular Network (TIN) format (Figure 15d).

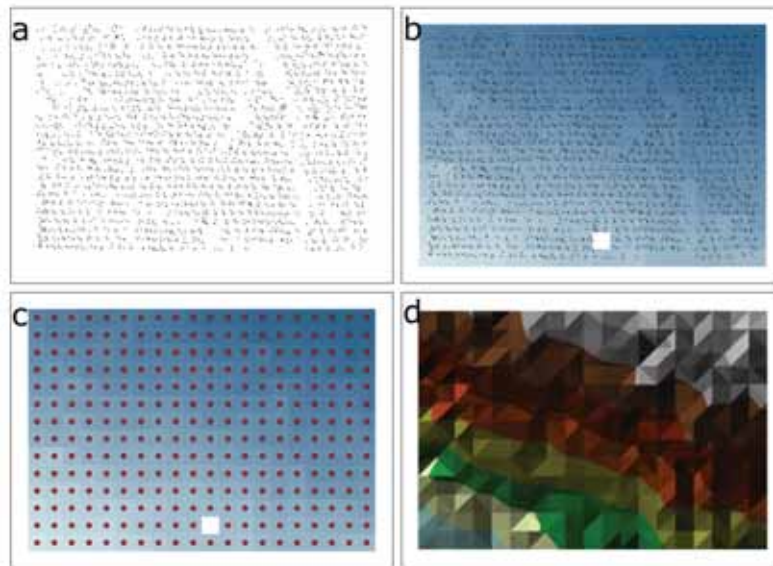


Figure 15: Graphical example of the filtering process and DTM creation. a) Part of the original point cloud, b) the derived raster c) the new points derived from the raster, d) DTM based on the triangulation of the points from c.

The filtering process was repeated four times in total, using a different unit cell size each time for the creation of the raster (1, 5, 10 and 15 cm, respectively). A smaller cell unit size has the advantage of preserving higher levels of detail on the final output; however, there is also a higher chance that parts of the grass covering the bank of the river will not be filtered out effectively. Conversely, a larger cell unit size is more effective in filtering out the points corresponding to grass; however, there is also a high chance of removing points that belong to the bank of the river, thus, reducing the detail of the final output. For that reason an analysis was conducted in order to investigate how the different raster cell sizes affects the derived roughness characteristics and is presented in Chapter 3. In Figure 16 a subset of the DTM of the riverbank is presented, showing the output after application of filters of different unit cell size.

After the DTMs were created, four profiles were extracted along the riverbank, located 0.25 m apart from each other (Figure 16). This was accomplished by digitizing four polylines along the DTM, on a new feature class. Using the interpolate shape tool, under the 3D analyst toolbox, the cross sections were enriched with elevation data derived from the DTMs. The extracted profiles were exported from ArcGIS in a text format.

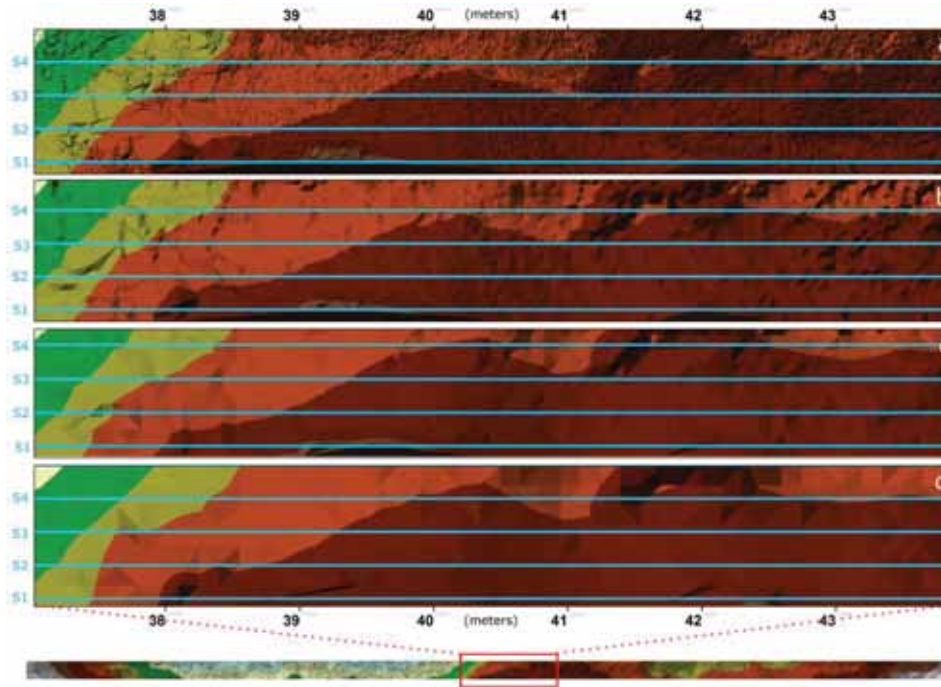


Figure 16: Subset of the created DTM after the application of filters of different unit cell size; a) 1 cm, b) 5 cm, c) 10 cm and d) 15 cm. The level of detail decreases as the unit cell size becomes larger; however, larger cell sizes filter out points representing the grass more effectively. The cross sections used to extract the profiles are also presented; the vertical distance between two subsequent cross sections is 0.25 m.

Filtering of the Vegetation, DSM creation and profile extraction

In order to extract profiles that would include the surface metrics of the present vegetation, the points representing the vegetation stems had to be incorporated in to the DTMs of the riverbank and Digital Surface Models (DSMs) had to be created. The points representing the vegetation stems (Figure 17a) were rasterised and the value of each raster cell was equal to the mean y value of the points located within the cell (Figure 17b). The mean y value was used based on the assumption that a vegetation stem, being a three-dimensional object, would be better represented, in a 2.5D surface, by its axis of symmetry. Subsequently, the raster was converted back to a point feature class, with each point being located in the middle of the corresponding raster cell and each raster cell value being assigned as the y coordinate of the corresponding point (Figure 17c). In the next step, these points were merged with the points representing the bare riverbank (Figure 17d) that were derived during the DTM creation (e.g. the ones from Figure 15c). After this step the feature class

contained both the filtered points representing the bare bank of the river as well as the filtered points representing the stems of the vegetation. This resulted in a point feature class in which some points had the same x and z but different y coordinates. For that reason the feature class was rasterised again, following the same method, but this time the assigned cell value was equal to the minimum y coordinate of the points within the corresponding raster, since this value represents the vegetation stems located in front of the riverbank (Figure 17e). Subsequently, the raster was converted back to points (Figure 17f), based on which the DSM of the riverbank in a TIN format was created (Figure 17g).

This process was also repeated four times in total, using the same different cell sizes that were previously used for the creation of the DTMs. Therefore, four final DSMs of the same area were created, each one with a different spatial resolution. Figure 18 presents a subset of these DSMs showing how the use of a different unit cell size affects the final output. Subsequently, four profiles were extracted along the exact same cross sections that were used earlier in the case of the DTMs (Figure 18) and exported in a text format. The method that was followed to extract and export the profile data from the DSMs was the same as before in the case of the DTMs.

The above described processes, that include the filtering of the point clouds, the creation of the DTMs and DSMs as well as the extraction of the profiles, were accomplished by creating a model in the model builder application of ArcGIS, which is presented in Appendix B. The DTMs and DSMs of all resolutions in their total extent are presented in Appendix C.

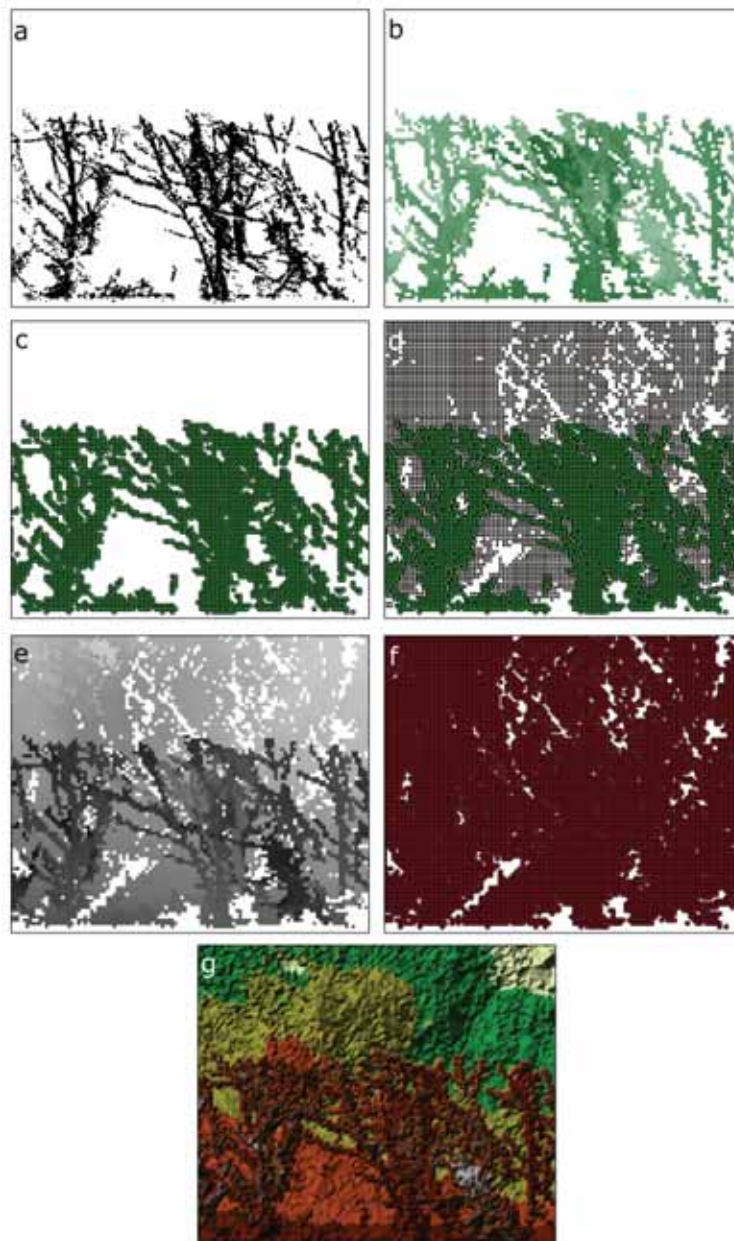


Figure 17: Graphical example of the filtering process and DSM creation. a) Subset of the original point cloud, b) the derived raster, the unit cell size is 1x1 cm and the cell value is equal with the mean y value of the corresponding points, c) the new points derived from the raster, d) the points of c merged with the points derived from the raster created during the DTM creation (e.g. Figure 15c), e) rasterization of the points, the cell size is 1x1 cm and the cell value is equal to the minimum y value of the corresponding points, f) points derived from the previous raster, g) final DSM of the riverbank in a TIN format.

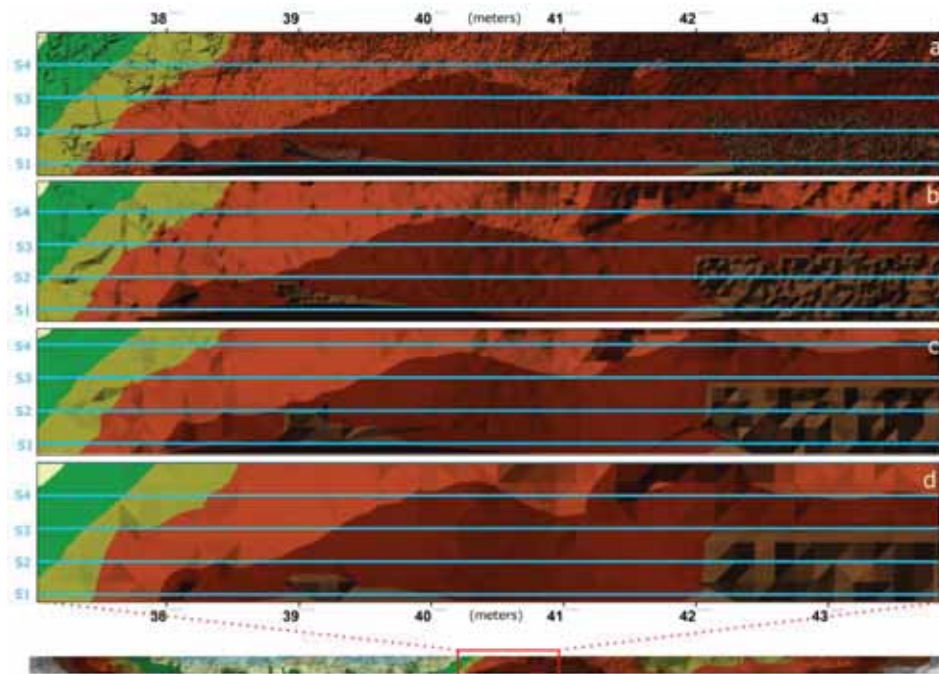


Figure 18: Subset of the created DTM after the application of filters of different unit cell size; a) 1 cm, b) 5 cm, c) 10 cm and d) 15 cm. The level of detail decreases as the unit cell size becomes larger; however, larger cell sizes filter out points corresponding to grass more effectively. The cross sections used to extract the profiles are also presented. The vertical distance between two subsequent cross sections is 0.25 m.

2.2.5 Modelling in Matlab

The subsequent step included extracting the roughness metrics from the profiles that were exported from ArcGIS. This was accomplished in Matlab using a code developed by Leyland (2012). This code fits Gaussian shaped curves that represent the roughness elements, located on the surface of the riverbank, based on points that are selected by the user. Furthermore, the code calculates the residuals between the original roughness element and the fitted Gaussian curve.

The exported, from ArcGIS, profiles were imported into Matlab. Subsequently, the code of Leyland (2012) was used and in each profile points that corresponded to the minima of each roughness element were selected (Figure 19 I and II top panel). Based on these points the code detrends the profile by removing undulations associated with the natural curvature of the river (Figure 19 I and II middle panel), since these undulations contribute insignificantly to the flow resistance (Kean and Smith, 2005). Furthermore, the code fits a

Gaussian curve for each roughness element (Figure 19 I and II bottom panel). Based on the geometry of the fitted Gaussian curves, the roughness metrics can be derived (i.e. H is the protrusion height, σ is the streamwise length of the Gaussian curve and λ is the spacing between two subsequent Gaussian curves). Moreover, based on the residuals between the fitted Gaussian curves and the geometry of the original roughness elements, the code calculates the local roughness height of the boundary without the topographic elements (z_{0SF}).

This process was repeated for all four profiles, which were previously derived from both the DTM and the DSM of the riverbank, for all four different spatial resolutions. Therefore, 32 profiles in total were analysed and the modelled profiles are presented in Appendix D. The output of the Matlab code was a text file for each profile containing the roughness metrics of each fitted Gaussian curve (λ, H, σ), the roughness height (z_{0SF}) calculated from the residuals between the fitted Gaussian curves and the original roughness elements, as well as, the values of the drag coefficient for each roughness element (C_D).

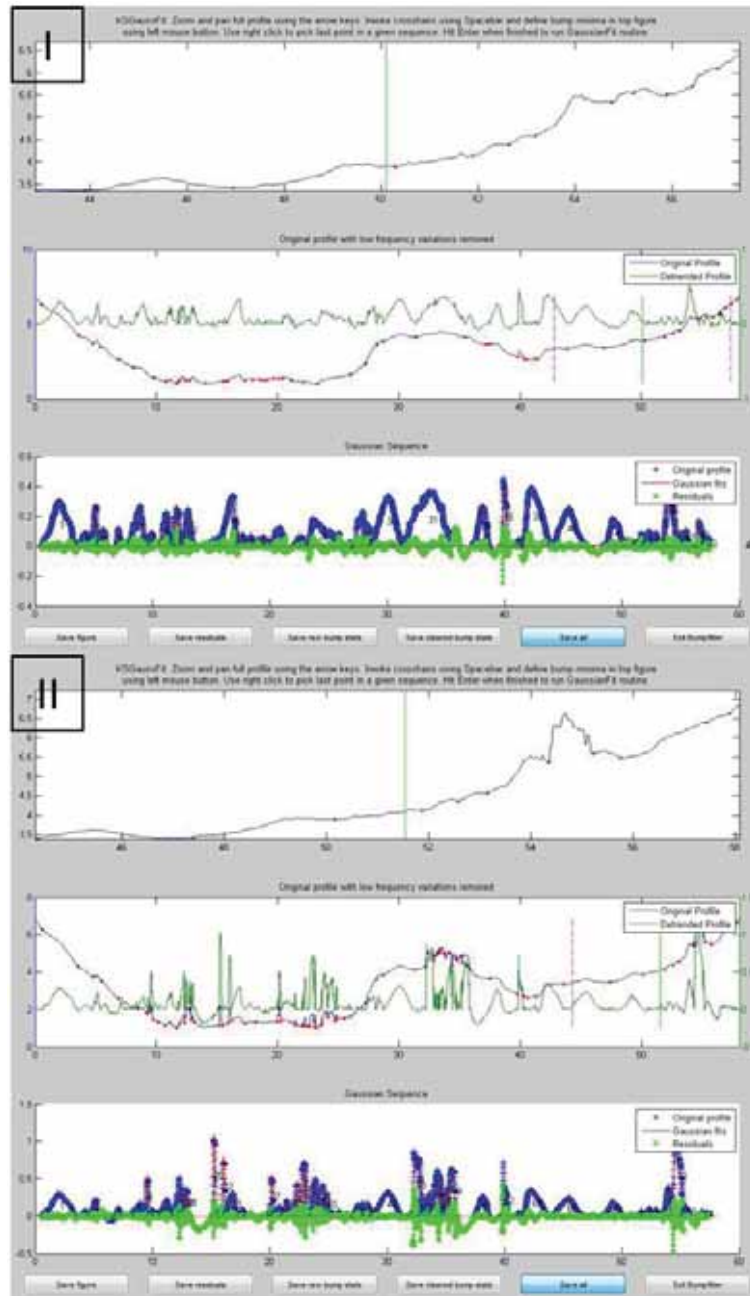


Figure 19: Modelled profiles of the cross section S2 from the 5cm resolution of the DTM (I) and the DSM (II). On the top panel a subset of the profile is presented, showing the points that were selected by the user. On the middle panel the original profile is presented with the blue line and the detrended profile with the green one. The bottom panel is showing the original profile with blue points, the Gaussian fit with the red line and the calculated residuals with green points.

3 Results and Analysis

As explained in sub section 2.2.5, a total of thirty-two profiles were analysed in Matlab to extract the pertinent bank roughness metrics. An example can be seen in Tables 1 and 2. Table 1 presents the roughness metrics, of the first ten roughness elements, that were derived from the cross section S2 of the 5 cm DTM, while Table 2 presents the roughness metrics, of the first ten roughness elements, derived along the same cross section but from the 5cm DSM. Data tables presenting the roughness metrics extracted from each of the profiles investigated herein, as derived from both the DTMs and the DSMs and at all spatial resolutions, are not presented in this document, for reasons of space, but are available for download via the following web-link:

<https://www.dropbox.com/sh/zhoflfka387qkff/EOSFRp0A6P>

Table 1: The extracted roughness metrics from the ten first roughness elements along the cross section S2 of the 5 cm DTM of the riverbank. Full data tables presenting the extracted roughness metrics are available for download via: <https://www.dropbox.com/sh/zhoflfka387qkff/EOSFRp0A6P>

<i>ID</i>	λ	<i>H</i>	σ	<i>C_D</i>	<i>Z_{0sf}</i>
1	3.8003	0.2887	0.646	0.3195	0.001795
2	0.983	0.0927	0.2171	0.2949	0.001037
3	0.6509	0.2589	0.1272	1.2261	0.002492
4	1.2517	0.1214	0.1703	0.6076	0.001979
5	0.7554	0.1182	0.0789	1.0708	0.001251
6	2.3003	0.2461	0.3171	0.6637	0.002305
7	0.5591	0.0974	0.084	0.9215	0.001395
8	1.3922	0.1904	0.1927	0.8209	0.002516
9	0.2061	0.2135	0.0393	1.5536	0.001203
10	0.5544	0.2532	0.1142	1.2648	0.004332

Table 2: The extracted roughness metrics from the ten first roughness elements along the cross section S2 of the 5 cm DSM of the riverbank. Full data tables presenting the extracted roughness metrics are available for download via: <https://www.dropbox.com/sh/zhoffka387qkff/EOSFRp0A6P>

<i>ID</i>	λ	H	σ	C_D	z_{0sf}
1	3.8686	0.2834	0.6516	0.3047	0.001696
2	0.8757	0.0684	0.1864	0.2195	0.000973
3	0.8806	0.212	0.1256	1.1343	0.002595
5	0.9234	0.1049	0.0807	0.99	0.000967
6	0.6106	0.0727	0.0554	0.9952	0.001222
7	0.8258	0.1633	0.1802	0.7655	0.001604
8	0.1163	0.1388	0.0265	1.5454	0.00272
9	0.36	0.5179	0.0653	1.6243	0.003994
10	0.365	0.0906	0.088	0.8468	0.000804

3.1 Statistical Analysis

Based on the extracted roughness metrics, parameter combinations, proposed by Kean and Smith (2006b), were also calculated, using the statistical software package R. The importance of these combinations lies on the fact that they represent the key physical attributes of the riverbank which are governing the flow resistance. Specifically, σ/H defines the shape of the roughness element, λ/σ is the ratio of the spacing of two subsequent crests and the streamwise length of the roughness element and $C_D H$ represents the wake's intensity downstream of the element that produces it. The tables, provided via the previously mentioned web-link (see introduction of this chapter), are updated and include the above mentioned combinations. Furthermore, histograms showing the distribution of the roughness metrics and their combinations were plotted, as discussed further below.

3.1.1 Histograms of the Roughness Metrics

The Matlab code, developed by Leyland (2012), generates the roughness metrics from each one of the fitted Gaussian curves. Histograms of the distributions of these values were plotted, in order

to highlight differences emerging from the presence of the vegetation on the riverbank which might not be clear from the comparison of the regularised, reach average values of the roughness metrics.

In Figures 20 to 23 the histograms of the roughness metrics that were extracted from the DTMs and the DSMs of all resolutions, along all four cross sections, as well as their important combinations are presented. The 88th percentiles of the distributions were calculated and are also presented in the histograms. In the cases of H and σ , the 88th percentiles represent their regularised values (equation 17). The regularised value of λ is a function of H ; nevertheless, the 88th percentiles for the distributions of λ , as well as for the distributions of the combinations of the roughness metrics are also shown, as a basis for comparison between the two alternative scenarios.

3.1.1.1 Histograms derived from the 1 cm resolution DTM and DSM

In Figure 20 the histograms of the distributions of the roughness metrics and their important combinations extracted from the 1 cm resolution DTM and DSM, are presented. The values of the roughness metrics are moderately affected by the presence of vegetation. In more detail, the distributions of λ are slightly wider when the vegetation is present, where the regularised values of λ are higher by 0.83 and 0.53 along the cross sections S1 and S3, respectively. The opposite effect is observed along the cross sections S2 and S4, where the regularised values are decreasing under the presence of vegetation by 1.25 and 0.1, respectively. A similar effect is also observed for the distributions of σ where the regularised values are higher by 0.17 and 0.05 along the cross sections S1 and S3 and lower by 0.36 and 0.09 along the cross sections S2 and S4. However, vegetation seems to have a more significant effect on the distribution of H , under the presence of vegetation. The regularised values of H are 0.21 higher along the cross section S1, 0.18 higher along the cross section S2 and 0.1 higher along the cross section S3; whereas no effect is shown along the cross section S4, located on the higher part of the riverbank and therefore intersecting with a lower density of vegetation. Finally, the wake's intensity increases due to the presence of vegetation along all four cross sections. The larger increase is observed along cross sections S1 and S2 where the regularised values of the product $C_D H$ are higher by 0.36 and 0.33 respectively, due to the presence of vegetation.

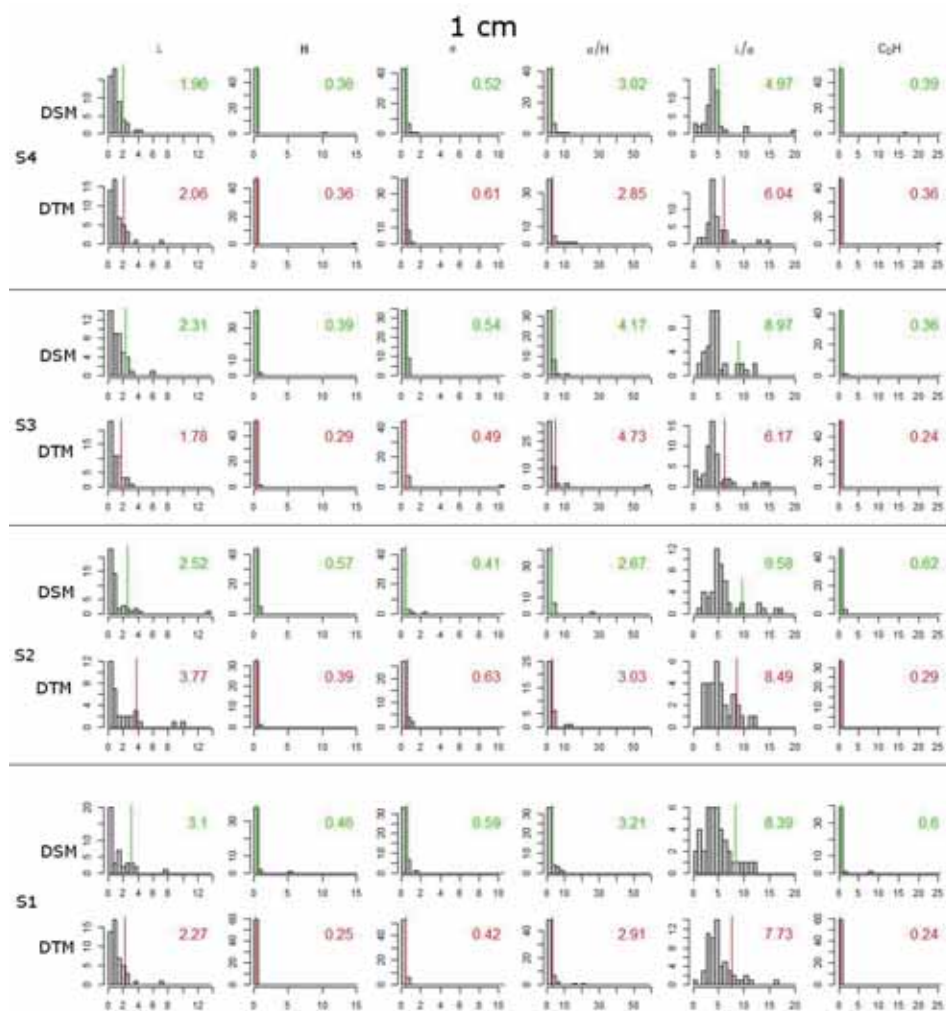


Figure 20: Histograms representing the distributions of the roughness metrics and their important combinations, extracted from the profiles of the DTM and the DSM at 1 cm resolution. The vertical lines and numbers at the top right corner of each histogram correspond to the 88th percentiles of the distributions.

3.1.1.2 Histograms derived from the 5 cm resolution DTM and DSM

The histograms of the distributions of the roughness metrics extracted from the 5 cm DTM and DSM are shown in Figure 21. The effect of the vegetation is more pronounced in this case. The regularised values of λ decrease by 1.24 in cross section S1, 0.75 in cross section S2, 0.72 in cross section S3 and 0.07 in cross section

S4, under the presence of vegetation. The regularised values of σ show a similar variation with an exception at the cross section S4. In more detail, they are decreasing by 0.30 along the cross sections S1 and S2 and by 0.02 along the cross section S3 when the vegetation is present. Furthermore, the presence of vegetation affects the distributions of σ , which appear more skewed to the right than in the non-vegetated scenario. The distributions of H are broader when the vegetation is taken into consideration where the regularised values of H are higher along the cross sections S1 and S2 by 0.13 and 0.21 respectively.

Moreover, the distributions of the ratio σ/H show a slight variation between the two scenarios. The regularised values of this ratio are much lower, by 2.23, for the cross section S1 when the vegetation is present. This effect becomes less pronounced for the cross sections that are located in higher parts of the riverbank. The regularised values of σ/H are 1.12 lower along the cross section S2 and 0.29 lower along the cross section S3, when the vegetation is present. Finally, the regularised values of the combination $C_D H$ are increasing due to the presence of vegetation; the regularised value is 0.36 higher for the vegetated scenario along the cross section S1 and 0.58 higher along the cross section S2. A small increase by 0.01 is also observed in the values of $C_D H$ along the cross section S4 when the vegetation is present.

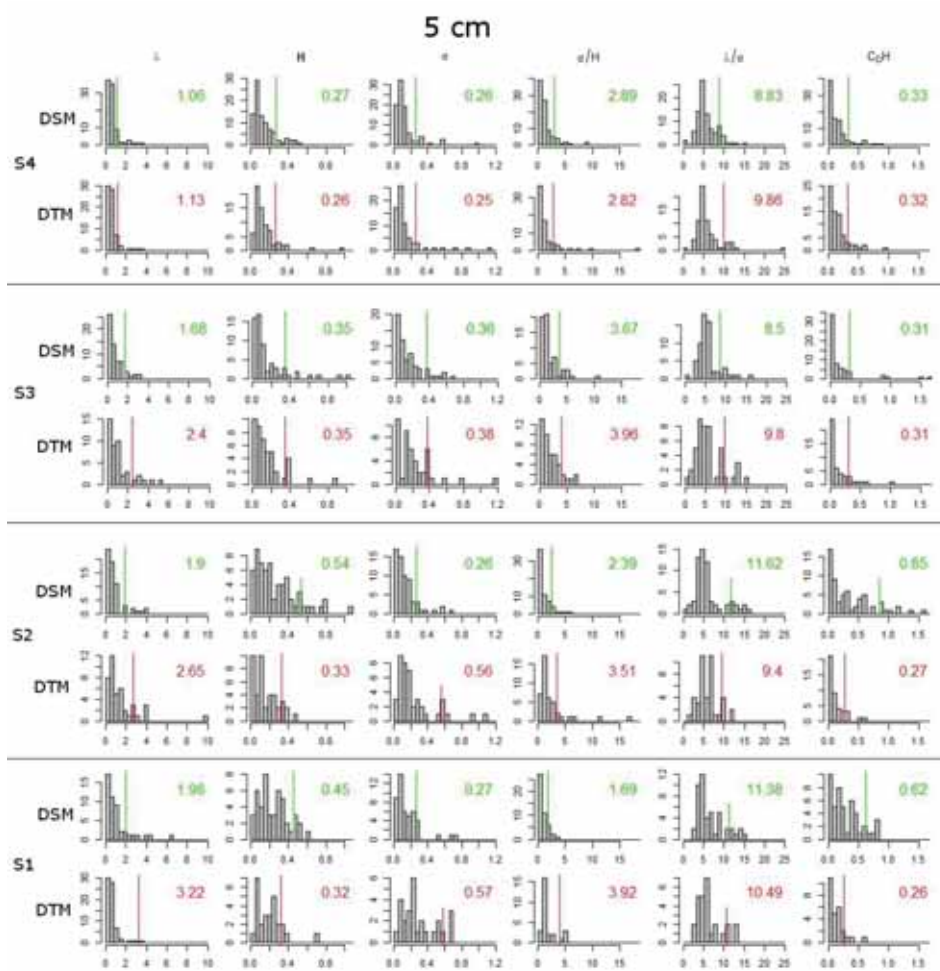


Figure 21: Histograms representing the distributions of the roughness metrics and their important combinations, extracted from the profiles of the DTM and the DSM at 5 cm resolution. The vertical lines and numbers at the top right corner of each histogram correspond to the 88th percentiles of the distributions.

3.1.1.3 Histograms derived from the 10 cm resolution DTM and DSM

The effect of the vegetation is more pronounced in the case of the 10 cm resolution DTM and DSM. The distributions of λ are less skewed to the right under the presence of vegetation and the regularised values of λ for the vegetated scenario are lower along the cross sections S1 and S2 by 1.01 and 0.57, respectively. Similarly, the regularised values of σ are lower for the vegetated scenario along the cross

sections S1, S2 and S4 by 0.22, 0.16 and 0.03 respectively. Conversely, the distributions of H are broader for the vegetated scenario with a small increase on the regularised values along all the cross sections (0.07, 0.42, 0.11 and 0.06 for the cross sections S1, S2, S3 and S4 respectively).

The regularised values of the ratio σ/H are lower in the vegetated scenario by 1.2 for the cross section S1, 2.59 for the cross section S2 and 0.2 for the cross section S3. The opposite effect is observed along the cross section S4 where the regularised value of the ratio is higher by 0.16. The distributions of the product $C_D H$ are broader for the vegetated scenario along all four cross sections. The regularised values are higher along the three lower cross sections (0.23, 0.67 and 0.22 for the cross sections S1, S2 and S3 respectively).

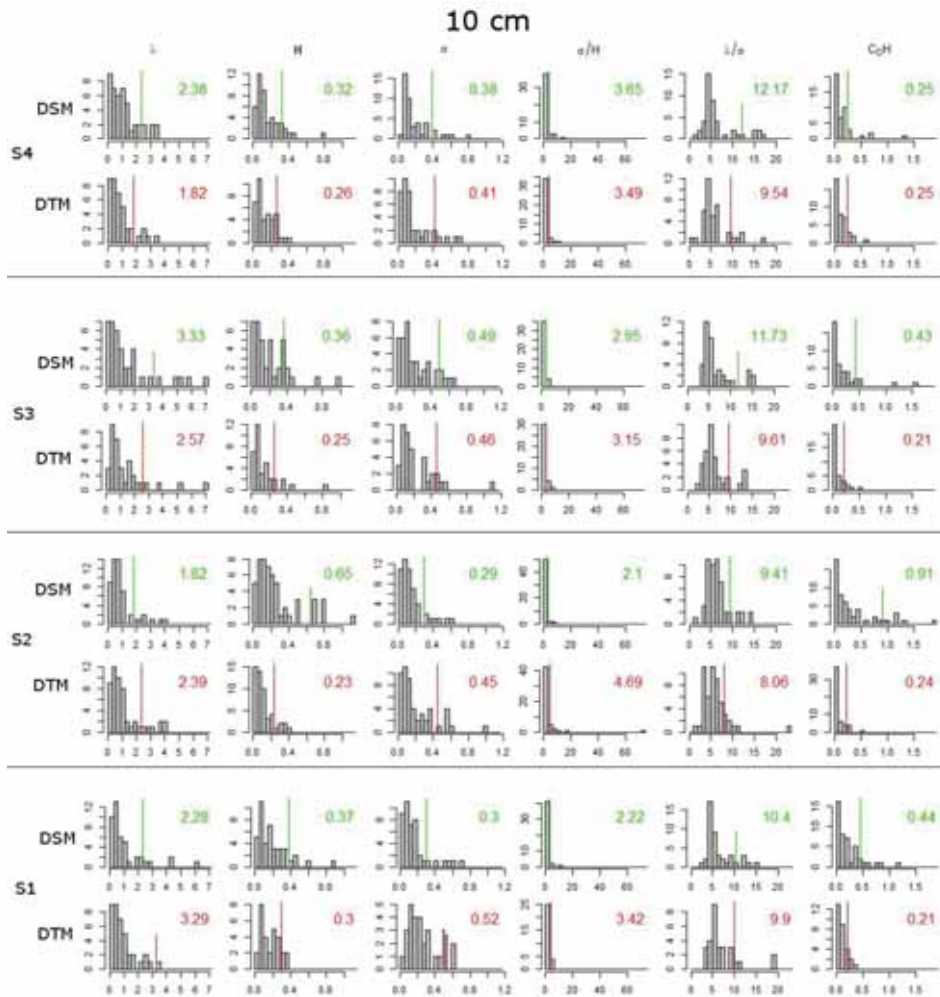


Figure 22: Histograms representing the distributions of the roughness metrics and their important combinations, extracted from the profiles of the DTM and the DSM at 10 cm resolution. The vertical lines and numbers at the top right corner of each histogram correspond to the 88th percentiles of the distributions.

3.1.1.4 Histograms derived from the 15 cm resolution DTM and DSM

The distributions of the roughness metrics as they were derived from the 15 cm DTM and DSM show a significant variation between the two scenarios. Specifically, the regularised values of H are higher due to the presence of vegetation along all the cross sections (0.23, 0.42, 0.3 and 0.01 higher along the cross sections S1, S2, S3 and S4, respectively). Conversely, the regularised values of λ and σ are

decreasing due to the presence of vegetation. In more detail, the regularised value of λ is 0.63 lower along the cross section S1, 0.3 lower along the cross section S2, 0.16 lower along the cross section S3 and 1.19 lower along the cross section S4. Similarly, the regularised value of σ is 0.03 lower along the cross section S1, 0.25 lower along the cross section S2, 0.05 lower along the cross section S3 and 0.11 lower along the cross section S4.

Moreover, the regularised value of the ratio σ/H is 3.31 lower along the cross section S1, 5.83 lower along the cross section S2, 1.18 lower along the cross section S3 and 0.88 lower along the cross section S4. Conversely, the regularised values of the product $C_D H$ increase due to the presence of vegetation and are higher by 0.47 along the lower cross section, 0.76 higher along the cross section S2 and 0.51 higher along the cross section S3.

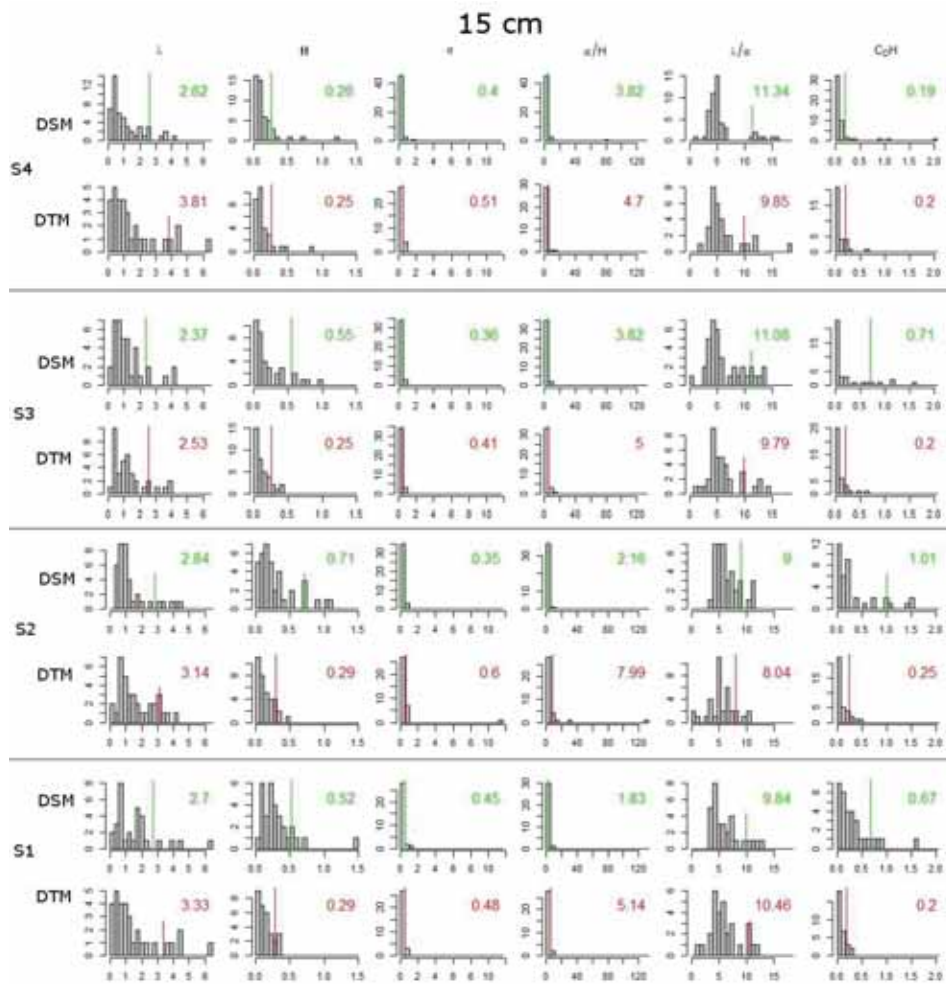


Figure 23: Histograms representing the distributions of the roughness metrics and their important combinations, extracted from the profiles of the DTM and the DSM at 15 cm resolution. The vertical lines and numbers at the top right corner of each histogram correspond to the 88th percentiles of the distributions.

3.1.1.5 Overall

It is evident that the presence of vegetation on the riverbank is affecting the roughness metrics by increasing the regularised values of the protrusion height (H). This is because, when the vegetation elements are taken into account, the diameter of their stems is being added to the protrusion height of the topographic undulations of the bank. Furthermore, the regularised values of the streamwise length (σ) of the roughness elements are being decreased due to the

presence of vegetation, this is because the vegetation stems, which are narrower than the topographic undulations of the riverbank, are taken into consideration. Similarly, the regularised values of the spacing between two subsequent elements (λ) are also being decreased due to the presence of vegetation, since the number of roughness elements located in the same reach is increasing for the vegetated scenario. Furthermore, the ratio σ/H decreases due to the presence of vegetation, indicating a change on the geometry of the roughness elements and the values of the product $C_D H$ increase, indicating that the intensity of the wake produced by the roughness elements becomes stronger when the vegetation is taken into account.

All of the above described effects are more pronounced along the cross sections that are located on the lower parts of the riverbank (cross sections S1 and S2) because these cross sections intersect with a higher density of vegetation. The distributions of the roughness metrics and their combinations, as well as their regularised values, are also significantly affected by the resolution of the DTMs and the DSMs, with larger differences being observed on the metrics that were extracted from the coarser surfaces. For this reason a resolution analysis was conducted as discussed further below.

3.2 Resolution Analysis

Based on the statistical analysis, it is evident that the resolution of the DTMs and the DSMs affects significantly the extracted roughness metrics and consequently their calculated regularised values. Therefore, a resolution analysis is extremely important in identifying which is the optimal scale for the analysis in this particular study.

The average values of the roughness metrics (λ , H , σ and z_{0sf}) for the total extent of the surveyed reach were calculated, by averaging the mean values that were extracted from each profile. These average values were afterwards plotted against the resolution of the DTMs and the DSMs, the diagrams are presented in Figures 24 and 25.

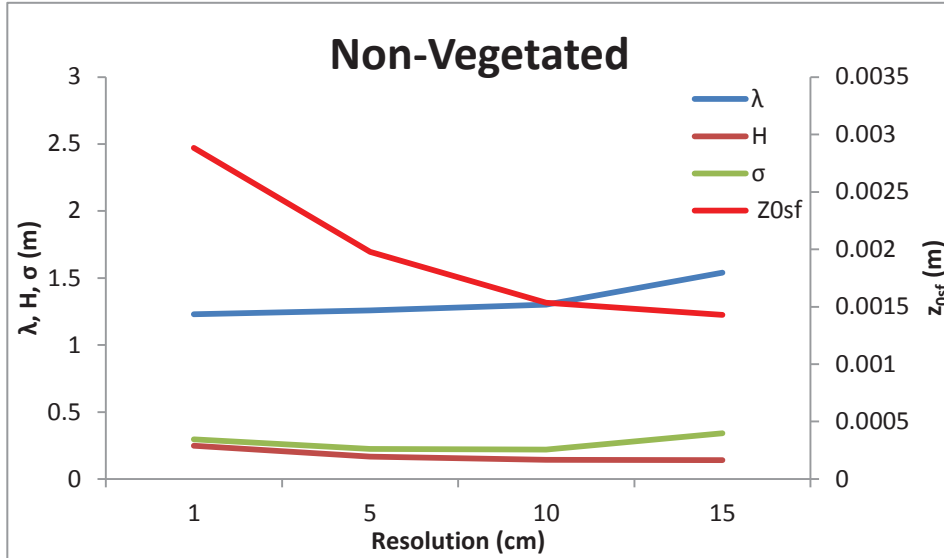


Figure 24: Variations of λ , H , σ and z_{0sf} as a function of the DTMs' resolution

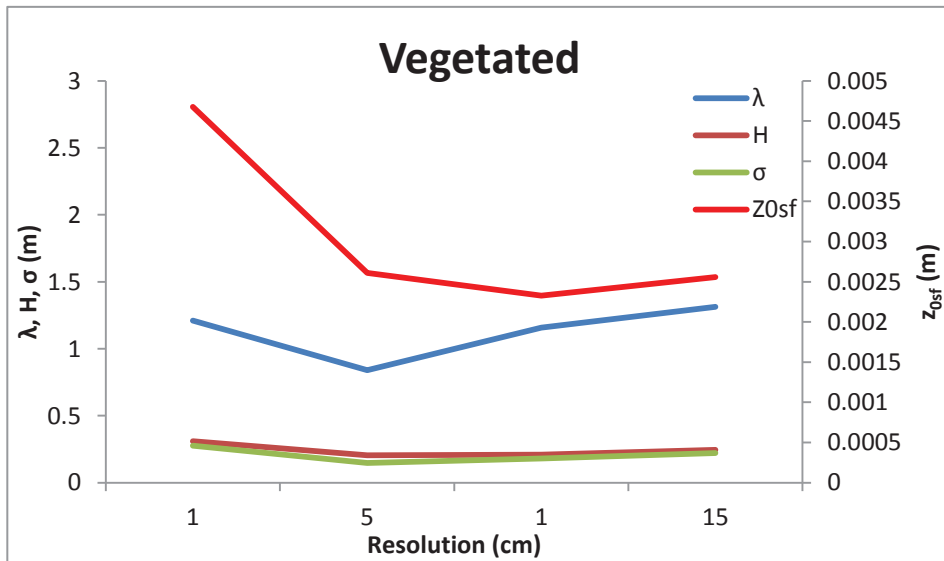


Figure 25: Variations of λ , H , σ and z_{0sf} as a function of the DSMs' resolution

The values of the protrusion height (H) and the streamwise length (σ) of the roughness elements show insignificant variation along all the resolutions in both scenarios. Little variation is also observed for the values of the distance between two subsequent roughness elements

(λ) for resolutions up to 10 cm, with an exception for the 5 cm resolution in the vegetated scenario (Figure 25). However, the resolution of 15 cm seems to be overestimating the values of λ .

The roughness height (z_{0sf}) is significantly affected by the used resolutions with its values being significantly higher for the finer resolution of 1 cm. This is probably due to the fact that the cell size of 1 cm was not effective enough in removing the points representing the grass during the filtering process. The roughness height (z_{0sf}) is calculated from the residuals between the original profile of the riverbank and the fitted Gaussian curves. Therefore, points representing the grass, that were not removed during the filtering process, are likely to produce a more complicated profile geometry, for which the approximated Gaussian curve has a lower goodness of fit and consequently higher values of roughness height are estimated.

Based on these observations it is safe to discard the resolutions of 1 and 15 cm. Therefore the optimal resolution for this study is between 5 and 10 cm, since for these resolutions the points that represent the grass are filtered out effectively, without any significant effects on the extracted roughness metrics.

Another observation, based on these diagrams, is that the values of the roughness height (z_{0sf}) are lower, by two orders of magnitude in comparison with the values of H and σ and by three orders of magnitude, in comparison with the values of λ . Based on this, it can be derived that the values of the skin drag, directly affected by the values of the roughness height (z_{0sf}), are proportionally lower in comparison to the form drag values, which are directly affected by the values of the roughness metrics (H, λ, σ), demonstrating the dominant role of the form drag component of the boundary shear stress, which agrees with previous studies (e.g. Griffin et al., 2005, Kean and Smith, 2005, Darby et al., 2010)

3.3 Form Drag Index (FDI)

Using equation 13 a ratio was calculated between the vegetated and the non-vegetated scenarios. This was done under the assumption that the reference velocity (u_{ref}) remains the same in both scenarios. In that case a simple index (equation 18) can be derived indicating the extent to which the presence of vegetation increases the form drag emanating from the bank roughness ($FDI > 1$) or decreases it ($FDI < 1$). $FDI = 1$ denotes that the present vegetation has no impact on the form drag.

$$FDI = \frac{C_{D,veg} \frac{H_{veg}}{\lambda_{veg}}}{C_{D,non-veg} \frac{H_{non-veg}}{\lambda_{non-veg}}} \quad (18)$$

In equation 18 the regularised values of the roughness metrics, given by equation 17, are used, averaged for the total surveyed reach. The same, average, regularised values were also used for the calculation of the drag coefficient C_D , which is given by equation 16.

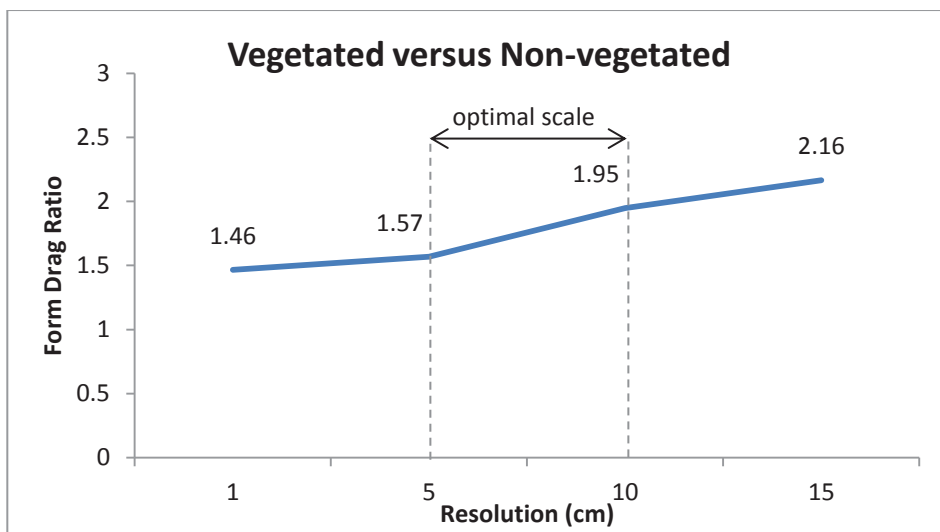


Figure 26: The FDI as it was calculated based on the regularised values averaged for the total surveyed reach that were derived from the models of different spatial resolutions.

From Figure 26 it is clear that the presence of vegetation has a significant effect on the form drag component of the boundary shear stress. The values of FDI , calculated from the metrics that were derived from all resolutions, are higher than 1 (1.46, 1.57, 1.95 and 2.16 for the 1, 5, 10 and 15 cm resolutions, respectively), indicating that the form drag emanating from the vegetative roughness adds to the form drag emanating from the bank's topographic roughness. However, as shown in Figure 26, the FDI is also scale-dependent, and shows significant variation according to the resolution of the DTMs and the DSMs, from which the roughness metrics were extracted. Nevertheless, based on the resolution analysis, which was described in section 3.2, the optimal resolution lies between 5 and 10 cm, based on that, the roughness emanating from the vegetation

elements increases the average form drag component of the boundary shear stress by at least 57% and not more than 95%.

The increased value of the form drag, caused by the riverbank's vegetation, will in turn limit the value of the skin drag (equation 2) and consequently decrease the rates of erosion (equation 1). However, measurements of the flow velocity are required in order to accurately quantify the skin drag component of the boundary shear stress. Furthermore, the estimation of the erodibility parameters (k and τ_c for equation 1) are also necessary for an accurate quantification of the erosion rates. Such measurements were not obtained because the quantification of the skin drag and the erosion rates exceeds the purposes of this study. Furthermore, the additional drag emanating from the present vegetation will alter the river flow, by decreasing the flow velocity and increasing the flow depth and in turn the flood risk potential.

4 Discussion

TLS data were successfully used to derive the roughness characteristics of a riverbank under the presence and absence of vegetation, demonstrating that TLS technology has strong potential in fluvial studies, as long as an effective method of filtering can be developed for the 3D point clouds, if required, for each particular case.

4.1 *Optimal Scale of Measurement*

The resolution analysis, described in section 3.2, indicates that the optimal scale for measurements of river bank and vegetative roughness is between 5 and 10 cm. Finer resolutions seem to overestimate the values of the roughness height (z_{0st}). This is because smaller cell sizes do not succeed in effectively filtering out the points representing the grass that partially covers the riverbank. Conversely, coarser resolutions show a tendency to overestimate the values of the distance between two subsequent crests (λ). This is an expected effect since the surfaces derived from rasters of a coarser resolution are of lower detail and therefore omit roughness elements of smaller spatial dimensions. In the study of Leyland et al. (manuscript in preparation), which was conducted on a bare riverbank of the Cecina River in Italy, it is demonstrated that the optimal measurements are derived from any point spacing not higher than 4.8 cm. This indicates that measurements in the scale of few centimetres are sufficient to characterise the riverbank roughness. However, the optimal scale of measurement may show a low variation for each study site, due to the unique physical characteristics of each surveyed surface.

4.2 *Vegetated versus Non-Vegetated Bank Roughness*

As demonstrated in section 3.1.1, the presence of vegetation on the riverbank significantly affects the roughness metrics, by increasing the values of the protrusion height (H) and decreasing the values of the streamwise length (σ) as well as the distance between crests (λ) of bank roughness elements. Consequently, the form drag emanating from the vegetative roughness adds to the form drag emanating from the topographic roughness of the riverbank, as demonstrated in section 3.3. The total average form drag of the surveyed reach is

estimated to be 57 to 95 % higher than the form drag that would be present if the vegetation elements were removed from the flow.

The increased form drag stress will, in turn, limit the values of the skin drag and consequently control the erosion rates. However, for the accurate quantification of the skin drag component, measurements of the flow velocity are necessary. Furthermore, estimation of the riverbank's erodibility parameters, namely the erodibility coefficient (k) and the critical shear stress (τ_c) is required to accurately estimate the erosion rates. The above mentioned measurements were not obtained in this research, since the quantification of the skin drag and the estimation of the rates of erosion exceed the purpose of this initial study.

Moreover, the increased drag emanating from the vegetation added roughness will alter the flow dynamics of the river by decreasing the flow velocity (Thorne and Furbish, 1995) and increasing the flow depth (Griffin and Smith, 2004), the latter of which may increase the potential flood risk.

4.3 Criticism

The present study was based on some assumptions and idealisations that are discussed in the following sections.

4.3.1 Manual TLS Data Cleaning

As described in Chapter 2, the raw TLS data obtained in this work included points representing the riverbank, the grass that partially covers it as well as other types of vegetation growing in front of the riverbank. From the total of the points only those representing the riverbank and the lower rigid parts of the vegetation elements, that were positioned very close to the surface of the bank, were kept while the rest were discarded.

The points representing the vegetation foliage were manually removed from the TLS data. The assumption on which this decision was based is that the foliage will be out washed due to the forces exerted by the flow. Therefore, it will not provide any additional form drag stress.

Regarding the non-rigid parts of the vegetation, they were also discarded from the data because it was assumed that they will bend due to the forces exerted by the flow. This will change their angle between the main flow direction and the vegetation stem.

Consequently, the value of the drag emanating from the non-rigid stems will change as a function of the flow velocity. The assumption that these elements are stiff would lead to higher values of form drag that do not represent reality. Therefore, a decision was made that they should be discarded.

Regarding the rigid parts of the vegetation elements that were positioned further away from the riverbank. These were also discarded from the datasets based on the assumption that water will flow between these elements and the bank. Therefore, if these elements were included in the datasets and used in the creation of the DSMs, they would generate roughness elements with very large values of protrusion height. Consequently, very high values of form drag would be calculated that do not represent the real conditions of the reach.

Finally, regarding the lower rigid parts of the vegetation elements that were kept into the datasets and used for the construction of the DSMs. It is assumed that there is no space between the stems and the riverbank and therefore water flows only in front of the stems. Although this does not accurately represent the real conditions, it was taken care that only the stems that are positioned very close to the surface of the bank are included in the models. Therefore, any potential flow between the stems and the riverbank will insignificantly affect the river flow dynamics.

4.3.2 Filtering Method

The points representing the grass were filtered out from the 3D point clouds, based on the assumption that the grass will be out washed due to the forces exerted by the flow, similarly to the vegetation foliage. The TLS data were filtered by converting the 3D point clouds into rasters, as explained in section 2.2.4. This approach significantly downgrades the raw TLS data. Initially, an alternative filtering approach was attempted, using the slope based filtering algorithm (Vosselman, 2000) which is implemented in the Point Cloud Mapper (PCM) software, developed at ITC in the Netherlands and characterises each point of the 3D point cloud either as terrain or off-terrain, based on certain mathematical morphological criteria. However, this algorithm was developed for the filtering of airborne lidar data and it is based on the principle that "a large height difference between two nearby points is unlikely to be caused by a steep slope in the terrain" (Vosselman, 2000). This principle does not apply in the present study, where, due to the natural curvature of the river, steep undulations of the riverbank are common. Therefore, the

results of this filtering method were poor and are not presented here. Alternatively the raster based filtering approach was implemented instead.

4.3.3 Modelling Approach

The vegetation elements were incorporated into the DTMs and DSMs were created. This approach is different from the ones followed in previous studies, such as the ones by Griffin et al. (2005) and Manners et al. (2013), where the vegetation elements are approximated as vertical cylinders with a diameter equal to the mean diameter of the corresponding element's stem. Approximation of complex vegetation elements, such as the small trees located on the surveyed reach, with a vertical cylinder would overestimate the volume of the tree and consequently would produce significant errors. Individual branches could have been approximated as cylinders with the main axis of the cylinder being tilted in such a way that it would coincide with the main axis of the original branch. However, this is difficult to be modelled based on TLS data and it would not significantly improve the modelled surfaces.

4.3.4 FDI

An important assumption was made in the introduction of the FDI (section 3.3.3) where it is assumed that the reference velocity (u_{ref}) remains constant between the vegetated and the non-vegetated scenario. This assumption was necessary in order to quantify the additional drag emanating from the vegetative roughness. However, as described in section 1.3.1, the reference velocity (u_{ref}) is affected by three individual flow regions, namely internal boundary region, wake region and outer boundary layer region. The outer boundary layer region is the region that is not affected by the roughness of the bank and therefore it is safe to assume that the flow velocity within this region remains constant between the two scenarios. Conversely, the flow dynamics within the internal boundary and the wake regions are significantly affected by the presence of the roughness elements. Therefore, in reality, the reference velocity is likely to vary between the two scenarios. This is a limitation of the present study which could only be avoided if flow velocity measurements were obtained. However, the flow velocity measurements must be obtained during high flow peaks, when the roughness elements are submerged and affect the river flow dynamics. Therefore, two surveys are required, one under low flow conditions, when the roughness elements are above the level of the flow and the surface measurements can be obtained, and one under

high flow conditions when the roughness elements are submerged, affecting the flow dynamics, where the flow measurements can be obtained. It also must be stressed out that these two sets of measurements are meaningful only under the assumption that the riverbank topography remains unchanged during the acquisition of the two sets of measurements. This is highly unlikely based on the fact that the riverbank topography is constantly evolving under the influence of the erosional and depositional processes arising from the water flow (Darby et al., 2010), which is a limitation of the Kean and Smith model.

4.4 Recommendations

Improvements could be made in this study, which may assist in achieving models of higher accuracy. Firstly, the intensity values of the recorded laser echoes could be used to assist in the classification of the 3D point cloud data into different categories such as terrain, grass, tree foliage and vegetation stems. Thus, providing a robust way to clean the TLS data and minimize the requirement for filtering. However, that requires normalization of the recorded intensity values based on the distance between the scanner and the target, the angle of incidence, as well as the moisture content of the target.

Furthermore, as described in section 2.2.5 the modelling of the roughness elements is based on points that are manually selected by the user. Therefore, it is likely that this process is user-dependent and consequently the calculated roughness metrics may vary between individual users, a matter that should be further investigated.

Finally, repeated TLS surveys on the study area could provide the required measurements from which DEMs of Difference (DOD) could be derived, revealing the parts of the riverbank that are being actively influenced by the flow dynamics. Relation of this information with the location of the vegetation elements may provide further proof to the vegetation effect on the erosional and depositional processes and forms. Furthermore, repeated surveys could provide valuable data to investigate any temporal (seasonal perhaps) variation on the riverbank roughness.

5 Conclusion

The present study has demonstrated a method to incorporate surface measurements of high resolution, obtained from the riverbank of the River Lugg, into the existing Kean and Smith (2006a, 2006b) hydraulic model. The novelty of this study lies in the fact that measurements representing the vegetation elements were also introduced in the model. Thus, a clear quantification of the additional form drag emanating from the vegetative roughness is presented.

DTMs and DSMs of the riverbank were created from the obtained TLS data. The roughness metrics were derived from these models and significant variations between the vegetated and the non-vegetated scenarios were revealed through the statistical analysis. A Form Drag Index (FDI) was introduced. The estimated values of the FDI indicate that the additional form drag emanating from the vegetative roughness increases the total average form drag of the studied reach by at least 57 % and up to 95 %.

This high increase will consequently alter the flow dynamics of the river decreasing the flow velocity and increasing the flow depth indicating a higher flood potential. Furthermore, the higher average values of the form drag will in turn decrease the values of the skin drag component of the boundary shear stress and consequently limit the erosion rates. However, the accurate quantification of the skin drag component as well as of the erosion rates requires measurements of the flow velocity and of the riverbank's erodibility parameters, respectively.

Conclusion

References

- ABT, S. R., CLARY, W. P. & THORNTON, C. I. 1994. Sediment deposition and entrapment in vegetated streambeds. *Journal of Irrigation and Drainage Engineering*, 120, 1098-1111.
- AMIRI-TOKALDANY, E., DARBY, S. E. & TOSSWELL, P. 2003. Bank stability analysis for predicting reach scale land loss and sediment yield. *Journal of the American Water Resources Association*, 39, 897-909.
- ANTONARAKIS, A. S., RICHARDS, K. S., BRASINGTON, J. & BITHELL, M. 2009. Leafless roughness of complex tree morphology using terrestrial lidar. *Water Resources Research*, 45.
- BERALDIN, J. A., BLAIS, F. & LOHR, U. 2010. Laser Scanning Technology. In: VOSSSELMAN, G. & MAAS, H. G. (eds.) *Airborne and terrestrial laser scanning*. Whittles.
- BRASINGTON, J., LANGHAM, J. & RUMSBY, B. 2003. Methodological sensitivity of morphometric estimates of coarse fluvial sediment transport. *Geomorphology*, 53, 299-316.
- BRASINGTON, J., VERICAT, D. & RYCHKOV, I. 2012. Modeling river bed morphology, roughness, and surface sedimentology using high resolution terrestrial laser scanning. *Water Resources Research*, 48.
- BRIESE, C. 2010. Extraction of Digital Terrain Models. In: VOSSSELMAN, G. & MAAS, H. G. (eds.) *Airborne and terrestrial laser scanning*. Whittles.
- BRITISH GEOLOGICAL SURVEY. 2012. Available: http://www.bgs.ac.uk/science/landUseAndDevelopment/new_technologies/terrestrial_scanning.html [Accessed 21,10 2012].
- CENTRE FOR ECOLOGY & HYDROLOGY. 2013. Natural Environment Research Council. Available: http://www.ceh.ac.uk/data/nrfa/data/time_series.html?55003 [Accessed 24 04 2013].
- DARBY, S. E. 1999. Effect of riparian vegetation on flow resistance and flood potential. *Journal of Hydraulic Engineering-Asce*, 125, 443-454.
- DARBY, S. E., GESSLER, D. & THORNE, C. R. 2000. Computer program for stability analysis of steep, cohesive riverbanks. *Earth Surface Processes and Landforms*, 25, 175-190.
- DARBY, S. E., RINALDI, M. & DAPPORTO, S. 2007. Coupled simulations of fluvial erosion and mass wasting for cohesive river banks. *J. Geophys. Res.*, 112, F03022.
- DARBY, S. E., TRIEU, H. Q., CARLING, P. A., SARKKULA, J., KOPONEN, J., KUMMU, M., CONLAN, I. & LEYLAND, J. 2010. A

- physically based model to predict hydraulic erosion of fine-grained riverbanks: The role of form roughness in limiting erosion. *Journal of Geophysical Research-Earth Surface*, 115, 1-20.
- GRIFFIN, E. R., KEAN, J. W., VINCENT, K. R., SMITH, J. D. & FRIEDMAN, J. M. 2005. Modeling effects of bank friction and woody bank vegetation on channel flow and boundary shear stress in the Rio Puerco, New Mexico. *Journal of Geophysical Research-Earth Surface*, 110.
- GRIFFIN, E. R. & SMITH, J. D. 2004. *Floodplain stabilization by woody riparian vegetation during an extreme flood*, Washington, Amer Geophysical Union.
- HODGE, R., BRASINGTON, J. & RICHARDS, K. 2009a. Analysing laser-scanned digital terrain models of gravel bed surfaces: linking morphology to sediment transport processes and hydraulics. *Sedimentology*, 56, 2024-2043.
- HODGE, R., BRASINGTON, J. & RICHARDS, K. 2009b. In situ characterization of grain-scale fluvial morphology using Terrestrial Laser Scanning. *Earth Surface Processes and Landforms*, 34, 954-968.
- HODGE, R. A. 2010. Using simulated Terrestrial Laser Scanning to analyse errors in high-resolution scan data of irregular surfaces. *ISPRS Journal of Photogrammetry and Remote Sensing*, 65, 227-240.
- HOPSON, T. M. 1999. *The form drag of large natural vegetation along the banks of open channels*. University of Colorado.
- HOSSAIN, M. 1993. ECONOMIC-EFFECTS OF RIVERBANK EROSION - SOME EVIDENCE FROM BANGLADESH. *Disasters*, 17, 25-32.
- HUAI, W. X., LI, C. G., ZENG, Y. H., QIAN, Z. D. & YANG, Z. H. 2012. CURVED OPEN CHANNEL FLOW ON VEGETATION ROUGHENED INNER BANK. *Journal of Hydrodynamics*, 24, 124-129.
- INGENSAND, H. Metrological aspects in terrestrial laser-scanning technology. Proceedings of the 3rd IAG/12th FIG symposium, Baden, Austria, 2006.
- JARVIE, H. P., JÜRGENS, M. D., WILLIAMS, R. J., NEAL, C., DAVIES, J. J. L., BARRETT, C. & WHITE, J. 2005. Role of river bed sediments as sources and sinks of phosphorus across two major eutrophic UK river basins: the Hampshire Avon and Herefordshire Wye. *Journal of Hydrology*, 304, 51-74.
- KEAN, J. W. & SMITH, J. D. 2005. Generation and verification of theoretical rating curves in the Whitewater River basin, Kansas. *Journal of Geophysical Research-Earth Surface*, 110.
- KEAN, J. W. & SMITH, J. D. 2006a. Form drag in rivers due to small-scale natural topographic features: 1. Regular sequences. *Journal of Geophysical Research-Earth Surface*, 111.

- KEAN, J. W. & SMITH, J. D. 2006b. Form drag in rivers due to small-scale natural topographic features: 2. Irregular sequences. *Journal of Geophysical Research-Earth Surface*, 111.
- KNAPEN, A., POESEN, J., GOVERS, G., GYSSELS, G. & NACHTERGAELE, J. 2006. Resistance of soils to concentrated flow erosion: A review. *Earth-Science Reviews*, 80, 75-109.
- LAZAR, A. N., BUTTERFIELD, D., FUTTER, M. N., RANKINEN, K., THOUVENOT-KORPPOO, M., JARRITT, N., LAWRENCE, D. S. L., WADE, A. J. & WHITEHEAD, P. G. 2010. An assessment of the fine sediment dynamics in an upland river system: INCA-Sed modifications and implications for fisheries. *Science of The Total Environment*, 408, 2555-2566.
- LEE, I. S., LEE, J. O., PARK, H. J. & BAE, K. H. 2010. Investigations into the influence of object characteristics on the quality of terrestrial laser scanner data. *KSCE Journal of Civil Engineering*, 14, 905-913.
- LEMMENS, M. 2011. Terrestrial Laser Scanning. *Geo-information*. Springer.
- LEYLAND, J. 2012. Kean and Smith (2006) Gaussian roughness extraction Matlab code. Available from: <http://www.leyland.org.uk/downloads.html>.
- LEYLAND, J., DARBY, S. E., RINALDI, M., LILIANA, T. & OSTUNI, D. Temporal Variations in Bank Roughness Revealed by High-Resolution Digital Photogrammetry and Terrestrial Laser Scanning (Manuscript in preparation).
- LICHTI, D. D. 2007. Error modelling, calibration and analysis of an AM-CW terrestrial laser scanner system. *ISPRS Journal of Photogrammetry and Remote Sensing*, 61, 307-324.
- LICHTI, D. D., GORDON, S. J. & TIPDECHO, T. 2005. Error models and propagation in directly georeferenced terrestrial laser scanner networks. *Journal of surveying engineering*, 131, 135-142.
- MANNERS, R., SCHMIDT, J. & WHEATON, J. M. 2013. Multiscalar model for the determination of spatially explicit riparian vegetation roughness. *Journal of Geophysical Research: Earth Surface*, 1-19.
- MCLEAN, S. R. & SMITH, J. D. 1986. A MODEL FOR FLOW OVER TWO-DIMENSIONAL BED FORMS. *Journal of Hydraulic Engineering-Asce*, 112, 300-317.
- MEILE, T., BOILLAT, J. L. & SCHLEISS, A. J. 2011. Flow Resistance Caused by Large-Scale Bank Roughness in a Channel. *Journal of Hydraulic Engineering-Asce*, 137, 1588-1597.
- MILAN, D. J. 2009. Terrestrial laser scan-derived topographic and roughness data for hydraulic modelling of gravelbed rivers. *In:*

- HERITAGE, G. L. & LARGE, A. R. G. (eds.) *Laser Scanning for the Environmental Sciences*.: Wiley-Blackwell.
- MURGATROYD, A. & TERNAN, J. 1983. The impact of afforestation on stream bank erosion and channel form. *Earth Surface Processes and Landforms*, 8, 357-369.
- REES, W. G. 2001. *Physical principles of remote sensing*, Cambridge University Press.
- RINALDI, M. & DARBY, S. E. 2007. Modelling river-bank-erosion processes and mass failure mechanisms: progress towards fully coupled simulations. In: HABERSACK, H., RINALDI, M. & PIÉGAY, H. (eds.) *Gravel Bed Rivers VI: From Process Understanding to River Restoration*. Elsevier Science.
- RUMSBY, B. T., BRASINGTON, J., LANGHAM, J. A., MCLELLAND, S. J., MIDDLETON, R. & ROLLINSON, G. 2008. Monitoring and modelling particle and reach-scale morphological change in gravel-bed rivers: Applications and challenges. *Geomorphology*, 93, 40-54.
- SCHENK, T. 1999. Photogrammetry and laser altimetry. *International archives of photogrammetry and remote sensing*, 32, W14.
- SMITH, J. D. 2004. The role of riparian shrubs in preventing floodplain unraveling along the Clark Fork of the Columbia River in the Deer Lodge Valley, Montana. *Riparian Vegetation and Fluvial Geomorphology, Water Sci. Appl. Ser.*, 8, 71-85.
- SMITH, J. D. & MCLEAN, S. 1984. A model for flow in meandering streams. *Water Resources Research*, 20, 1301-1315.
- SMITH, J. D. & MCLEAN, S. R. 1977. Spatially averaged flow over a wavy surface. *Journal of Geophysical Research-Oceans and Atmospheres*, 82, 1735-1746.
- THORNE, S. D. & FURBISH, D. J. 1995. INFLUENCES OF COARSE BANK ROUGHNESS ON FLOW WITHIN A SHARPLY CURVED RIVER BEND. *Geomorphology*, 12, 241-257.
- UNITED STATES ENVIRONMENTAL PROTECTION AGENCY. 2000. The Quality of our Nation's Waters. *Water Quality Report* [Online]. Available: <http://www.epa.gov/305b/2000report/>.
- VOSSelman, G. 2000. Slope based filtering of laser altimetry data. *International archives of photogrammetry and remote sensing*, 33, 935-942.
- VOSSelman, G. & MAAS, H.-G. 2010. *Airborne and terrestrial laser scanning*, Whittles.
- WADE, A. J., BUTTERFIELD, D., GRIFFITHS, T. & WHITEHEAD, P. G. 2007. Eutrophication control in river-systems: an application of INCA-P to the River Lugg. *Hydrology and Earth System Sciences*, 11, 584-600.
- XIA, J., WU, B., WANG, Y. & ZHAO, S. 2008. An analysis of soil composition and mechanical properties of riverbanks in a

- braided reach of the Lower Yellow River. *Chinese Science Bulletin*, 53, 2400-2409.
- YAKHOT, V., ORSZAG, S., THANGAM, S., GATSKI, T. & SPEZIALE, C. 1992. Development of turbulence models for shear flows by a double expansion technique. *Physics of Fluids A: Fluid Dynamics*, 4, 1510.

References

APPENDIX A: TLS Point Clouds

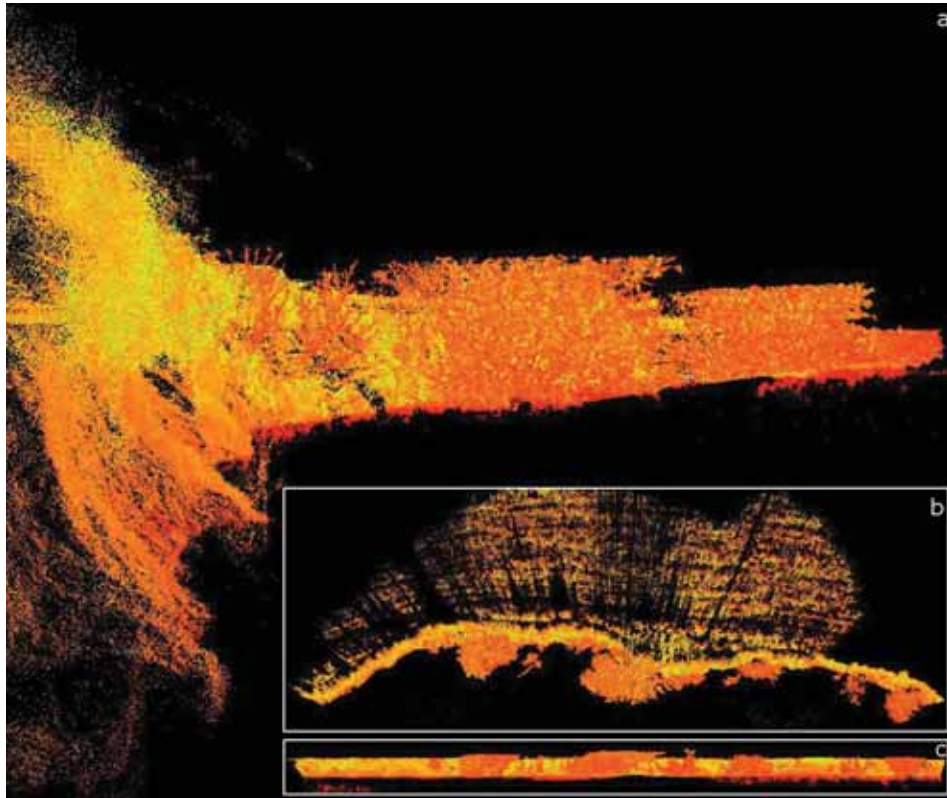


Figure 27: The original TLS 3D point cloud data; a) side view, b) top down view, c) front view

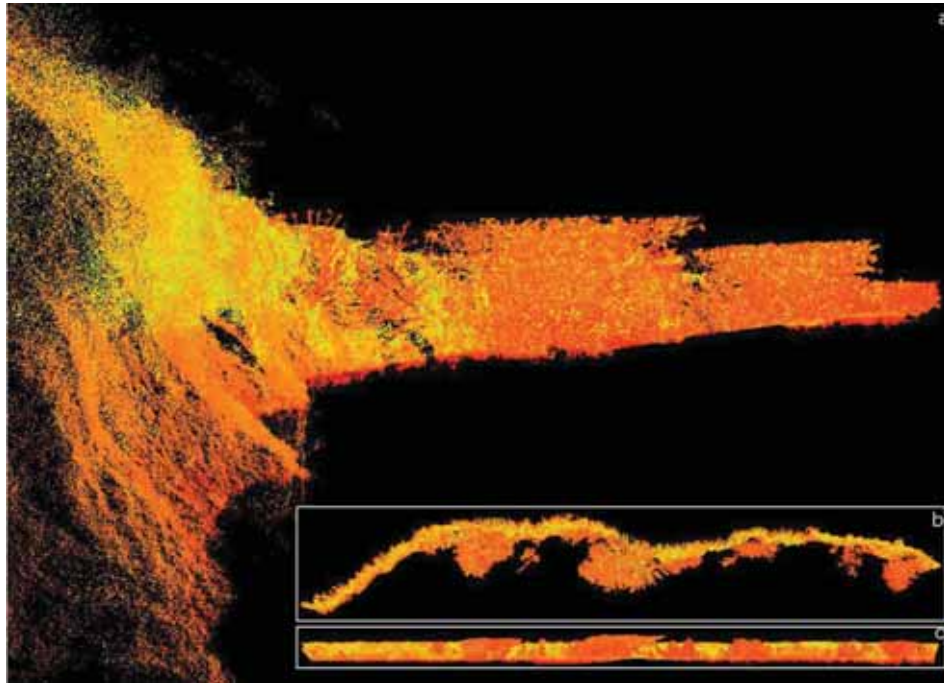


Figure 28: The cleaned TLS 3D point cloud data; a) side view, b) top down view, c) front view

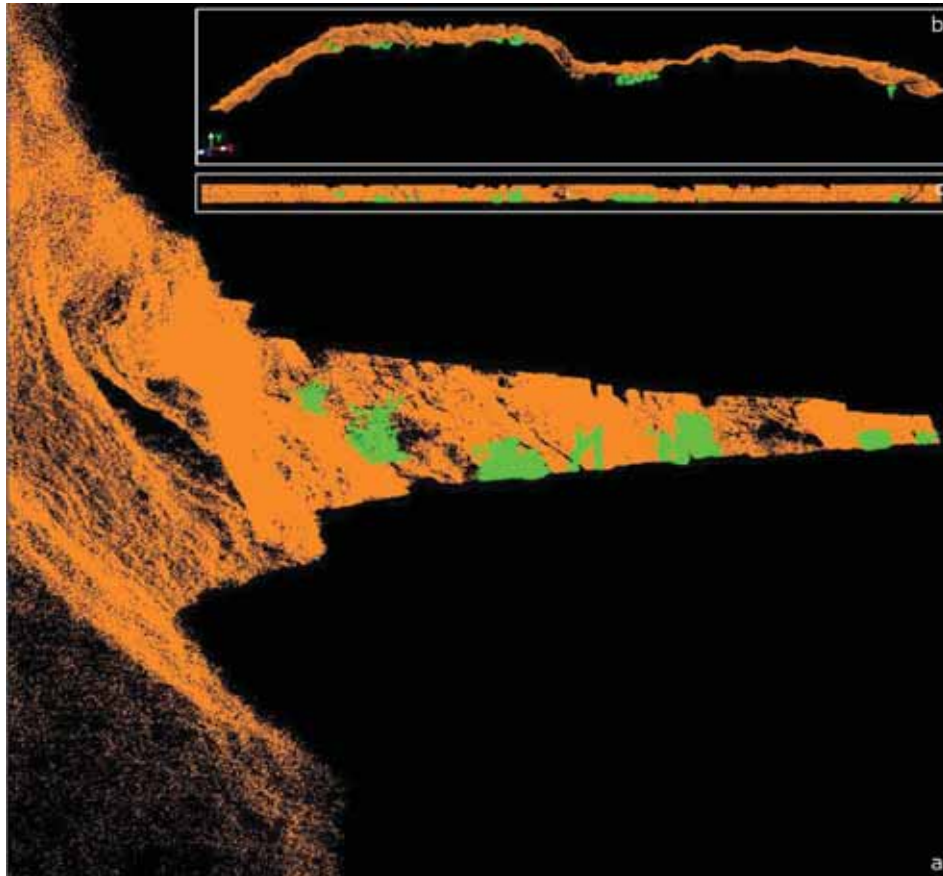


Figure 29: The final TLS data after their partitioning into two subsequent point clouds. The points representing the riverbank are in orange and the points representing the vegetation stems are in green colour a) side view, b) top down view, c) front view

APPENDIX B: ArcGIS Model

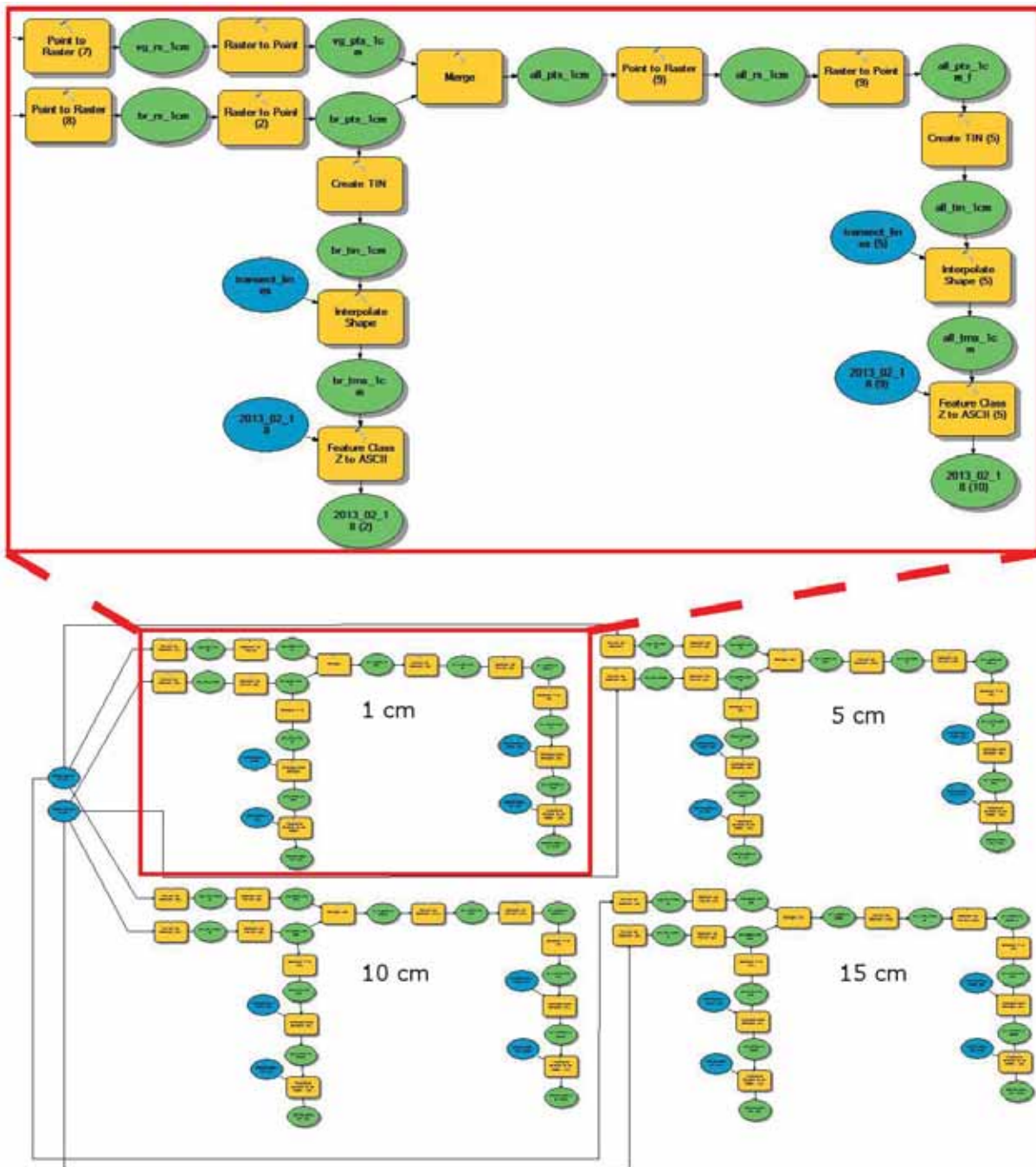


Figure 30: Model created in ArcGIS model builder for the filtering of the point clouds, the creation of the DTMs and DSMs, as well as the extraction and exporting of the profiles.

APPENDIX C: DTMs and DSMs

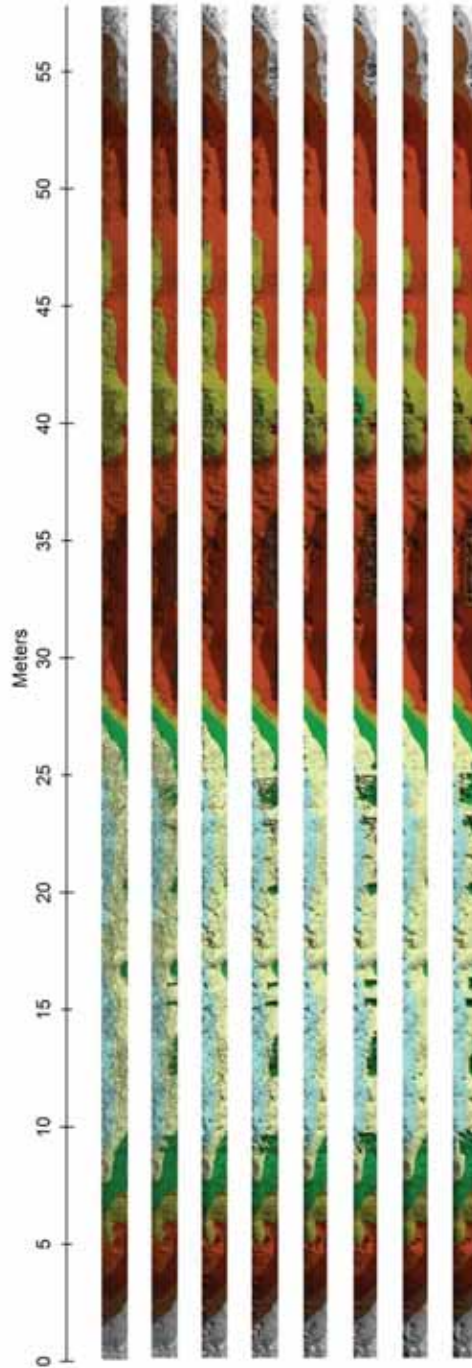


Figure 31: DTMs and DSMs of the riverbank in TIN format after the application of filters of different unit cell size. A) DTM 1 cm, b) DSM 1 cm, c) DTM 5 cm, d) DSM 5 cm, e) DTM 10 cm, f) DSM 10 cm, g) DTM 15 cm, h) DSM 15 cm.

APPENDIX D: Modelled Profiles

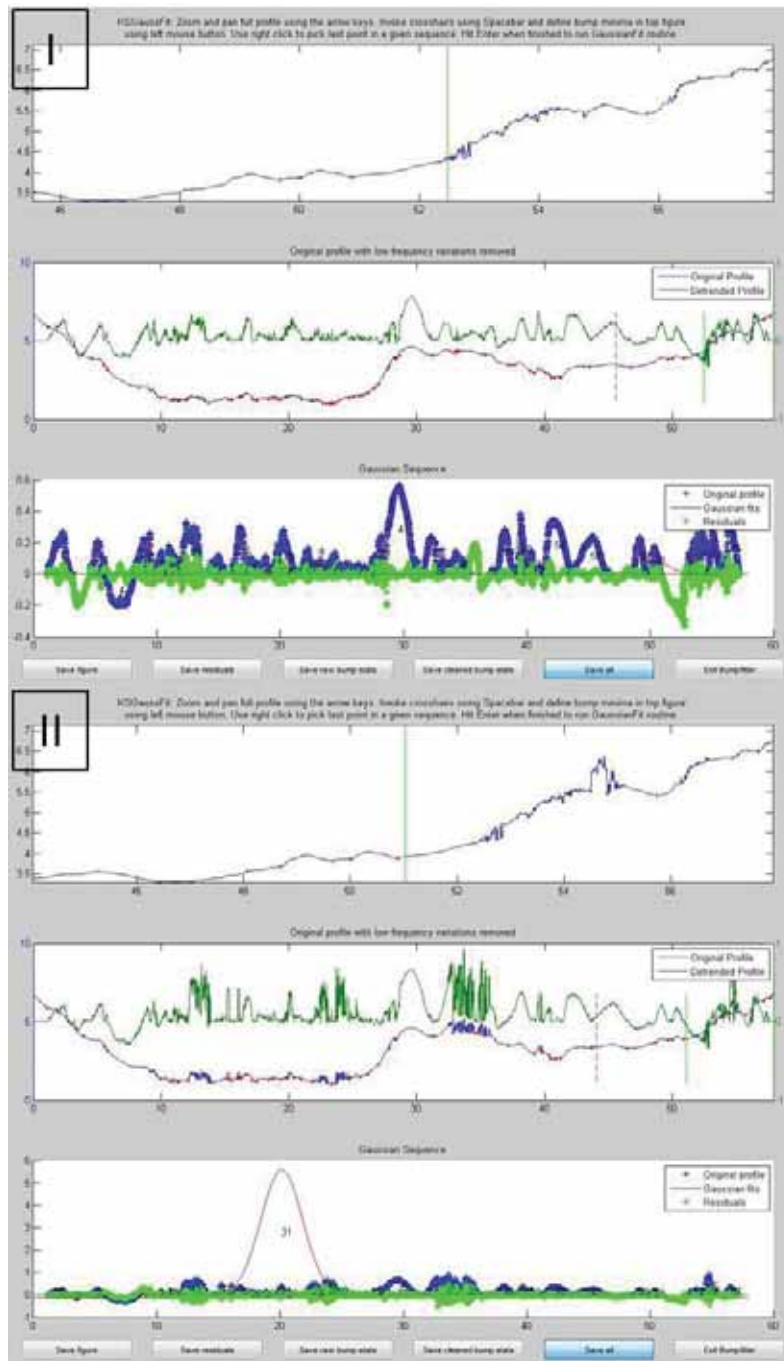


Figure 32: Modelled profiles of the cross section S1 from the 1 cm resolution of the DTM (I) and the DSM (II).

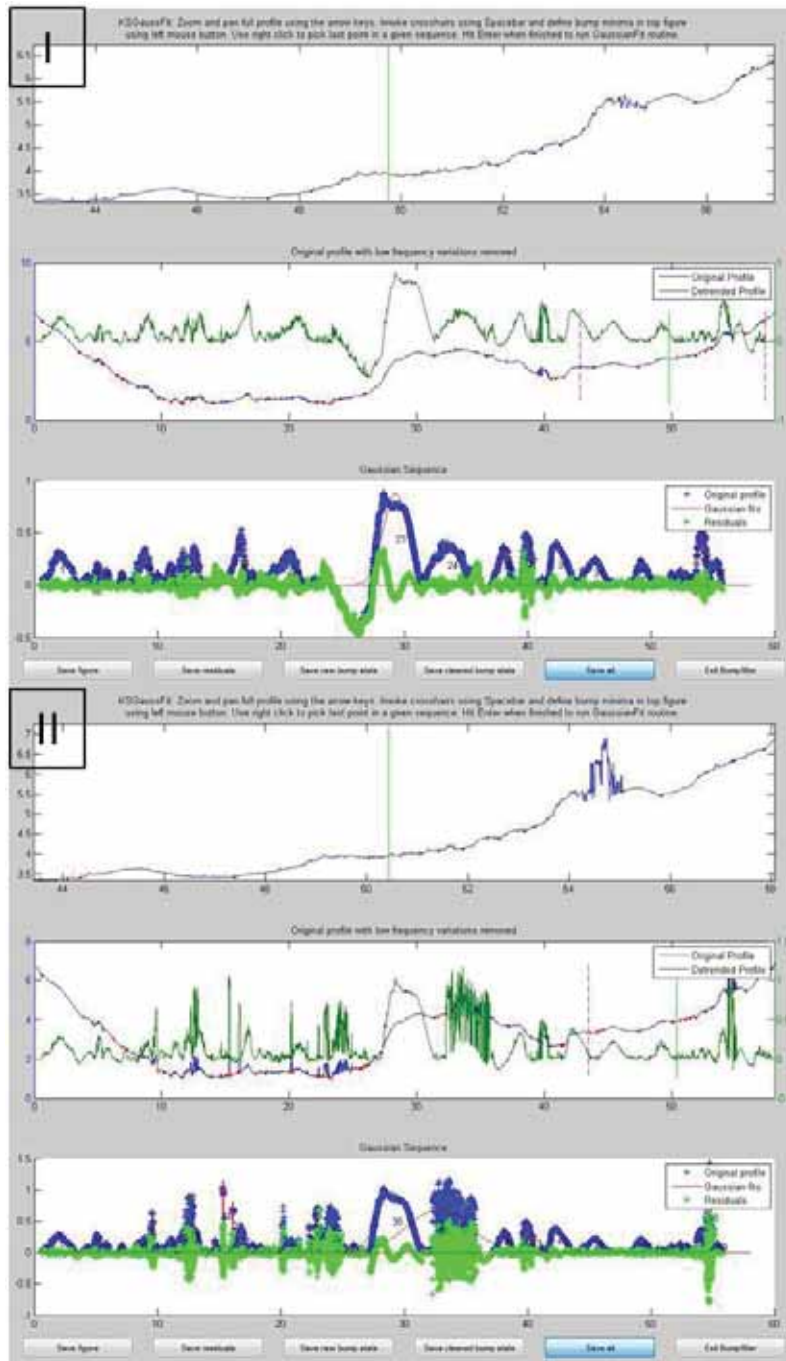


Figure 33: Modelled profiles of the cross section S2 from the 1 cm resolution of the DTM (I) and the DSM (II).

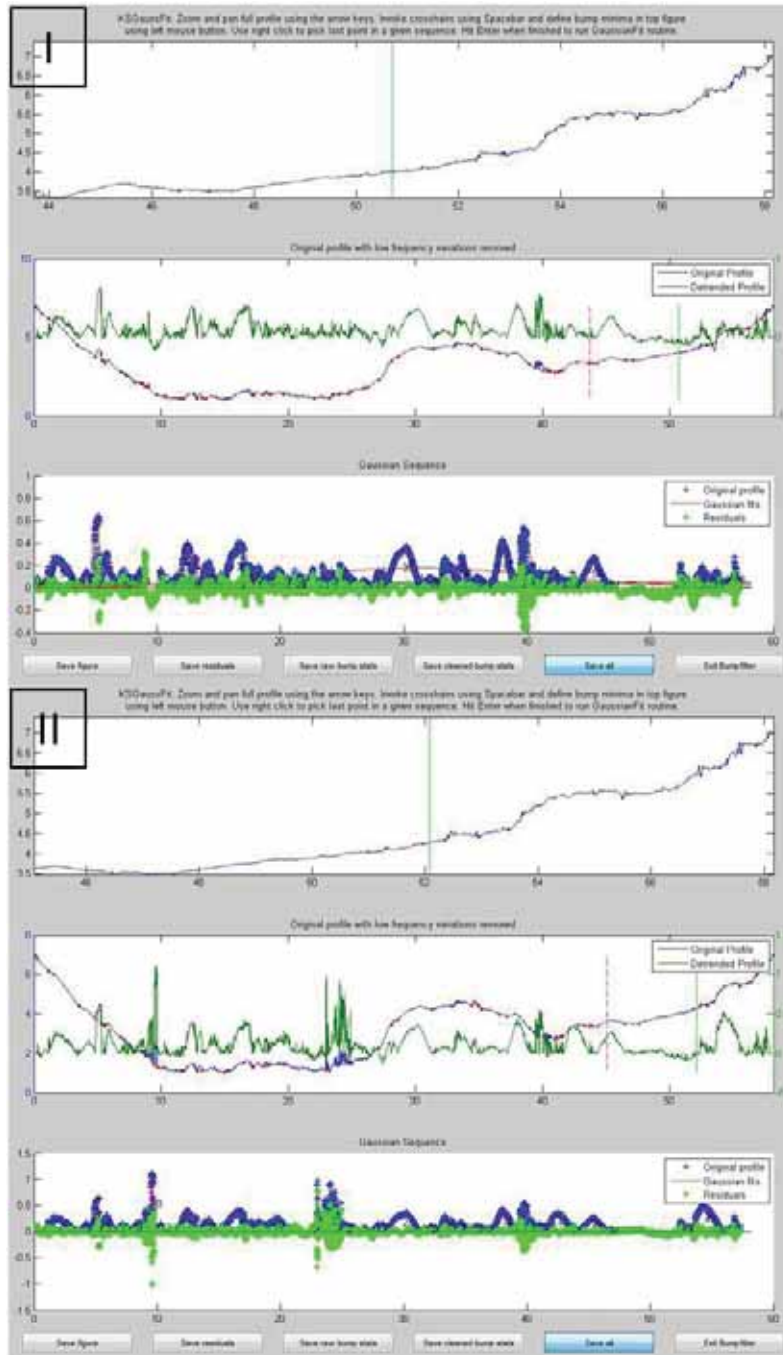


Figure 34: Modelled profiles of the cross section S3 from the 1 cm resolution of the DTM (I) and the DSM (II).

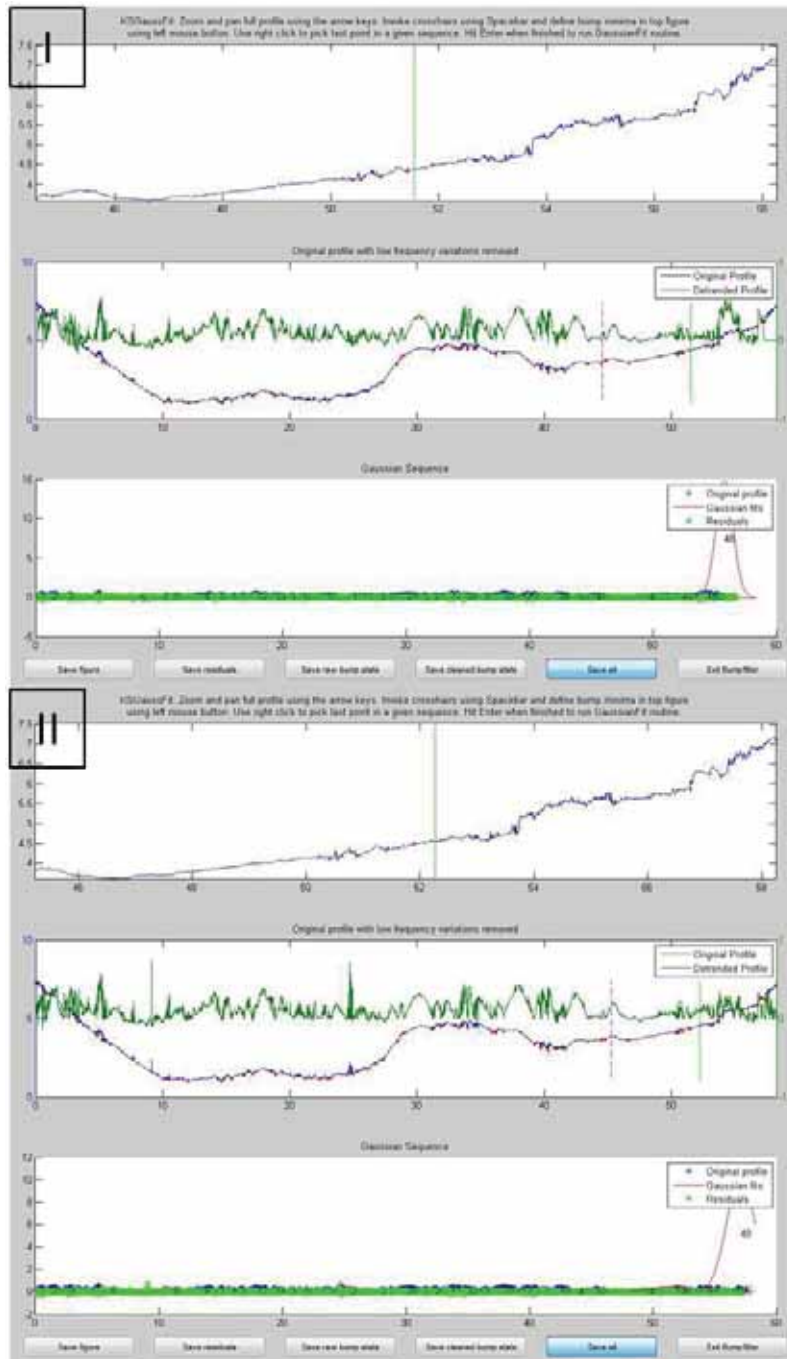


Figure 35: Modelled profiles of the cross section S4 from the 1 cm resolution of the DTM (I) and the DSM (II).

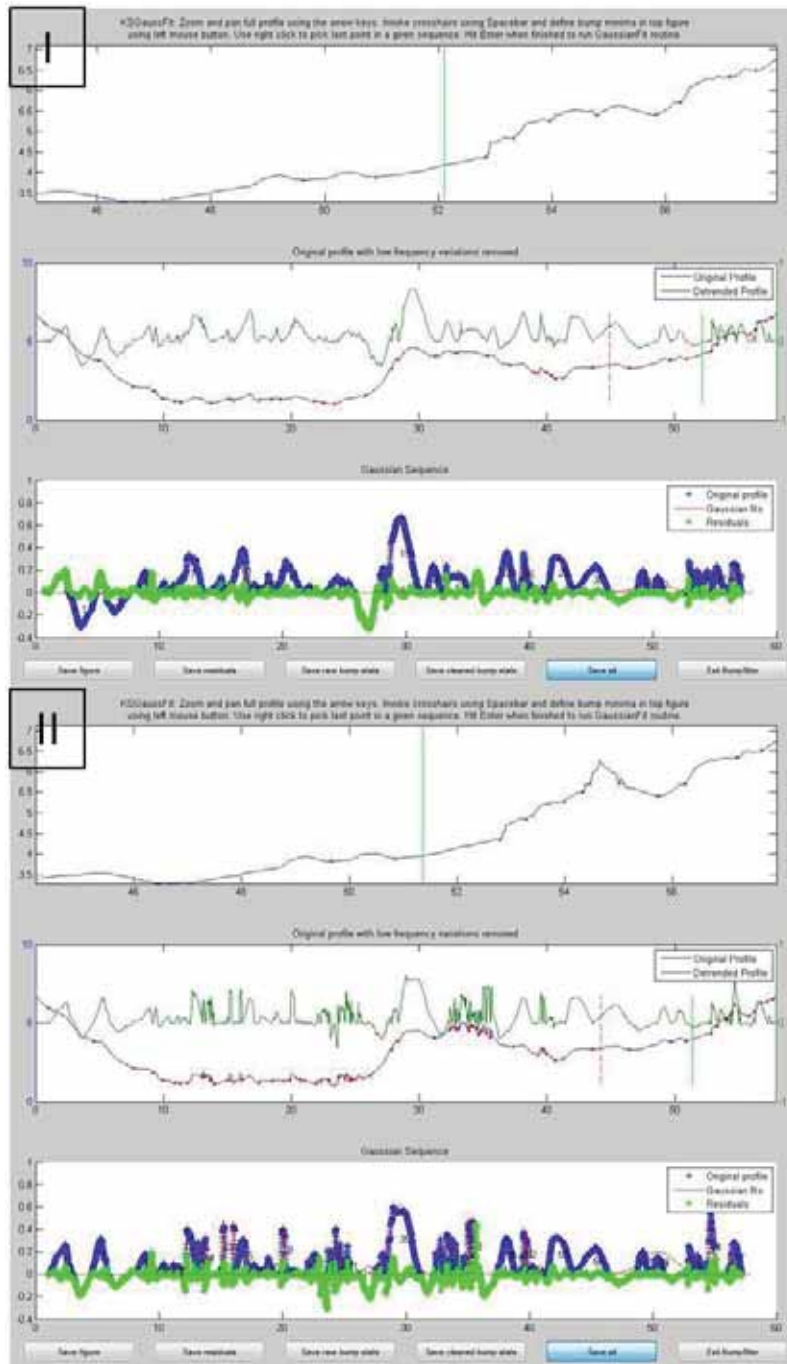


Figure 36: Modelled profiles of the cross section S1 from the 5 cm resolution of the DTM (I) and the DSM (II).

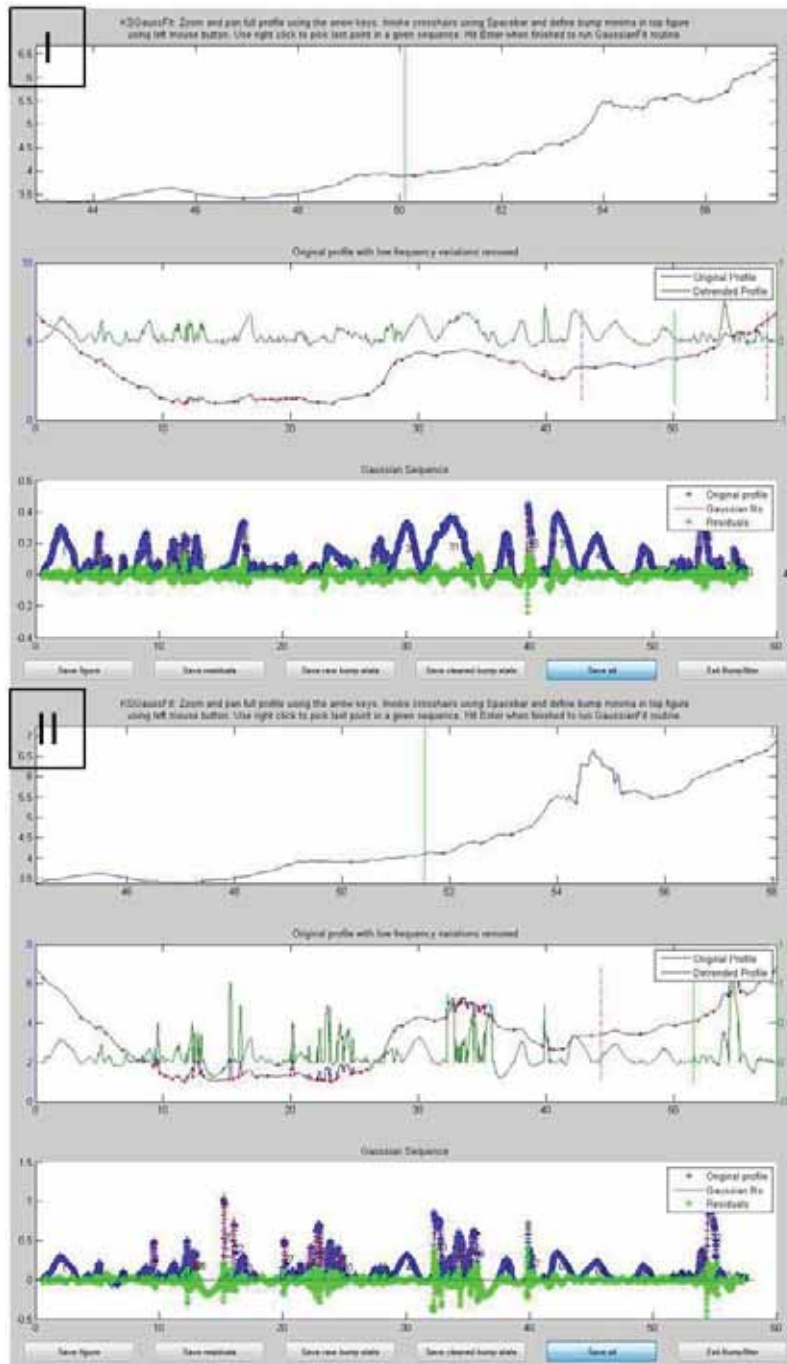


Figure 37: Modelled profiles of the cross section S2 from the 5 cm resolution of the DTM (I) and the DSM (II).

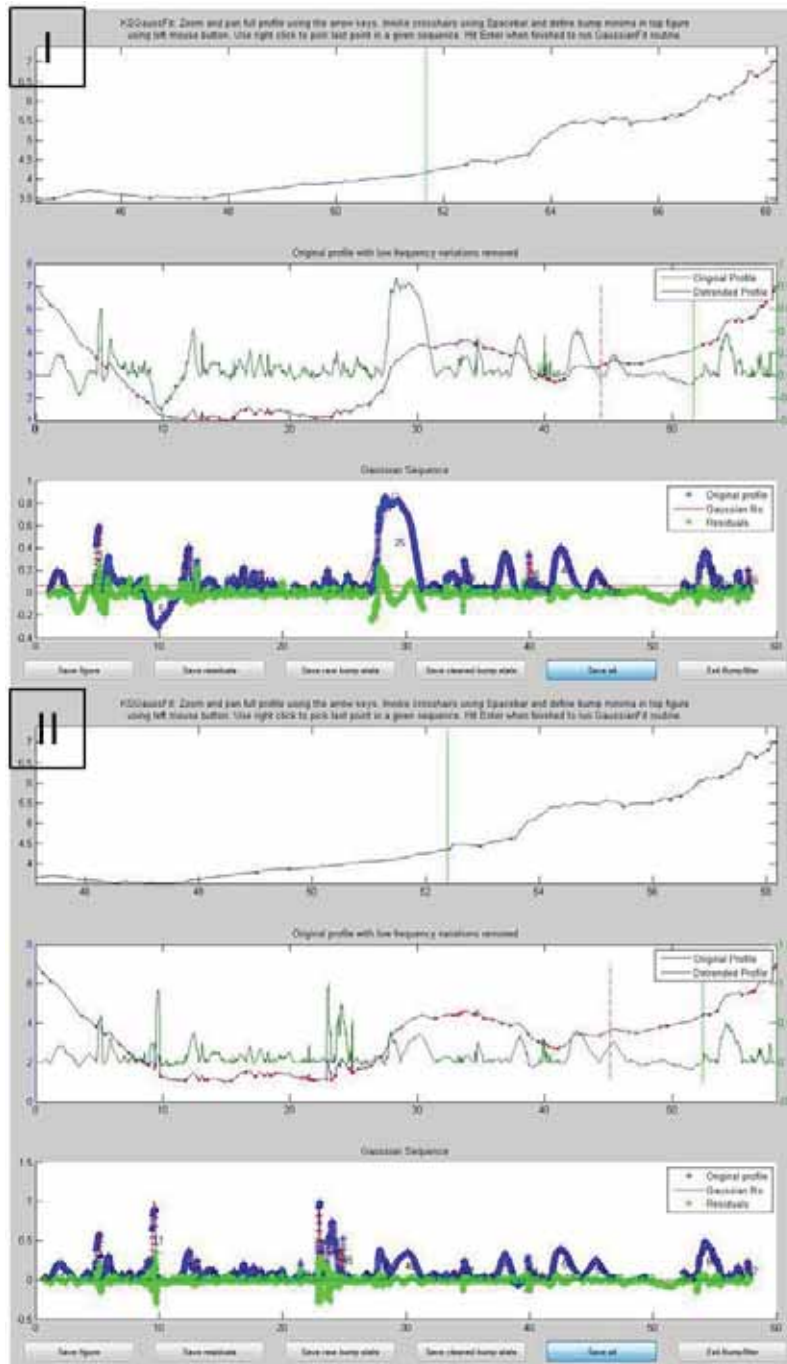


Figure 38: Modelled profiles of the cross section S3 from the 5 cm resolution of the DTM (I) and the DSM (II).

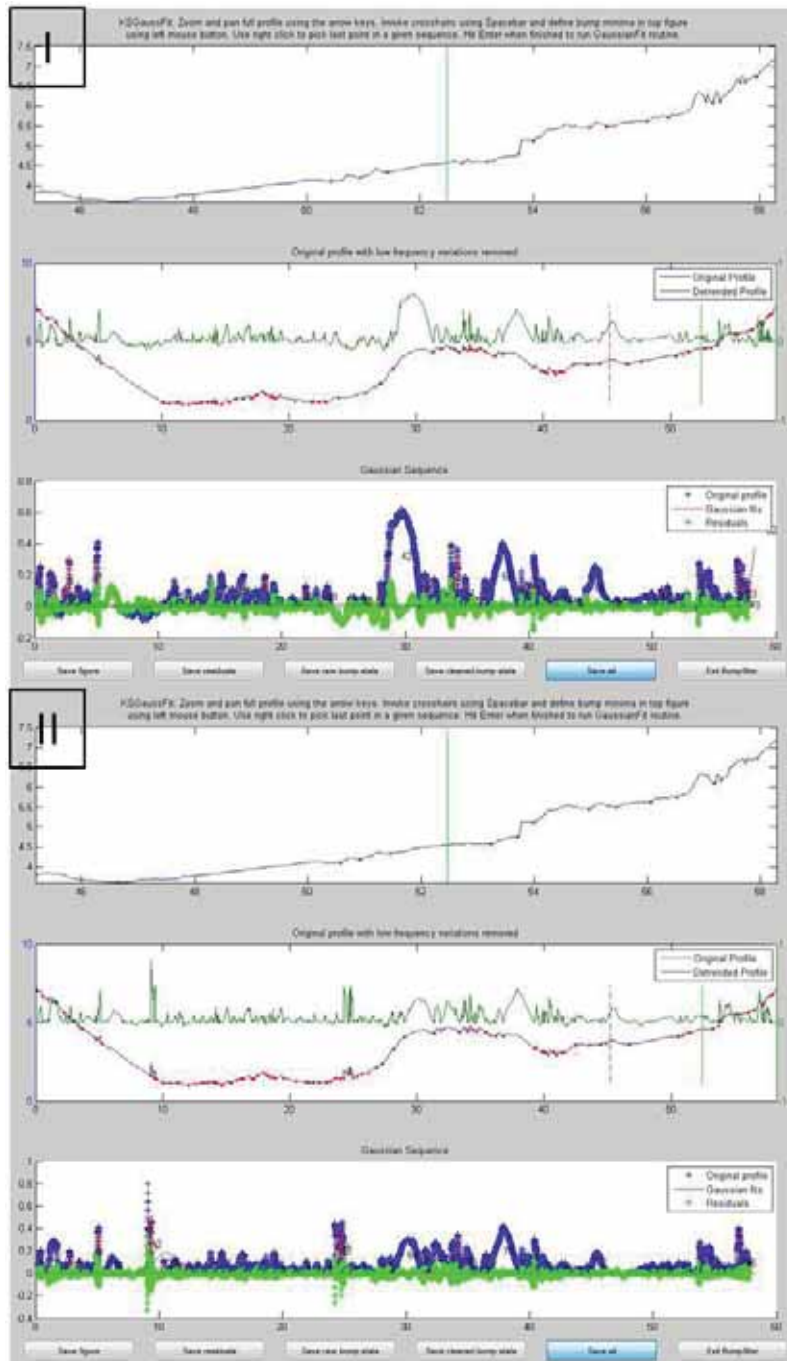


Figure 39: Modelled profiles of the cross section S4 from the 5 cm resolution of the DTM (I) and the DSM (II).

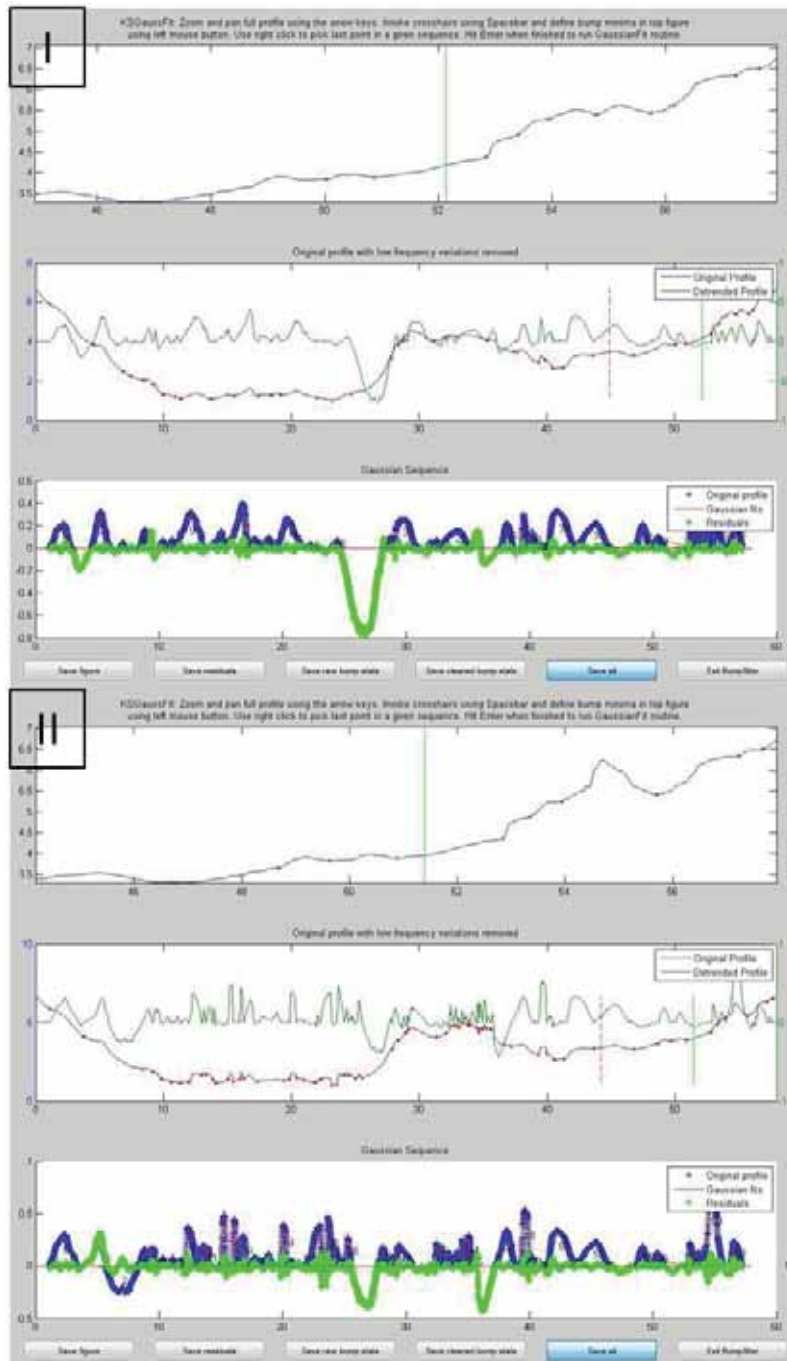


Figure 40: Modelled profiles of the cross section S1 from the 10 cm resolution of the DTM (I) and the DSM (II).

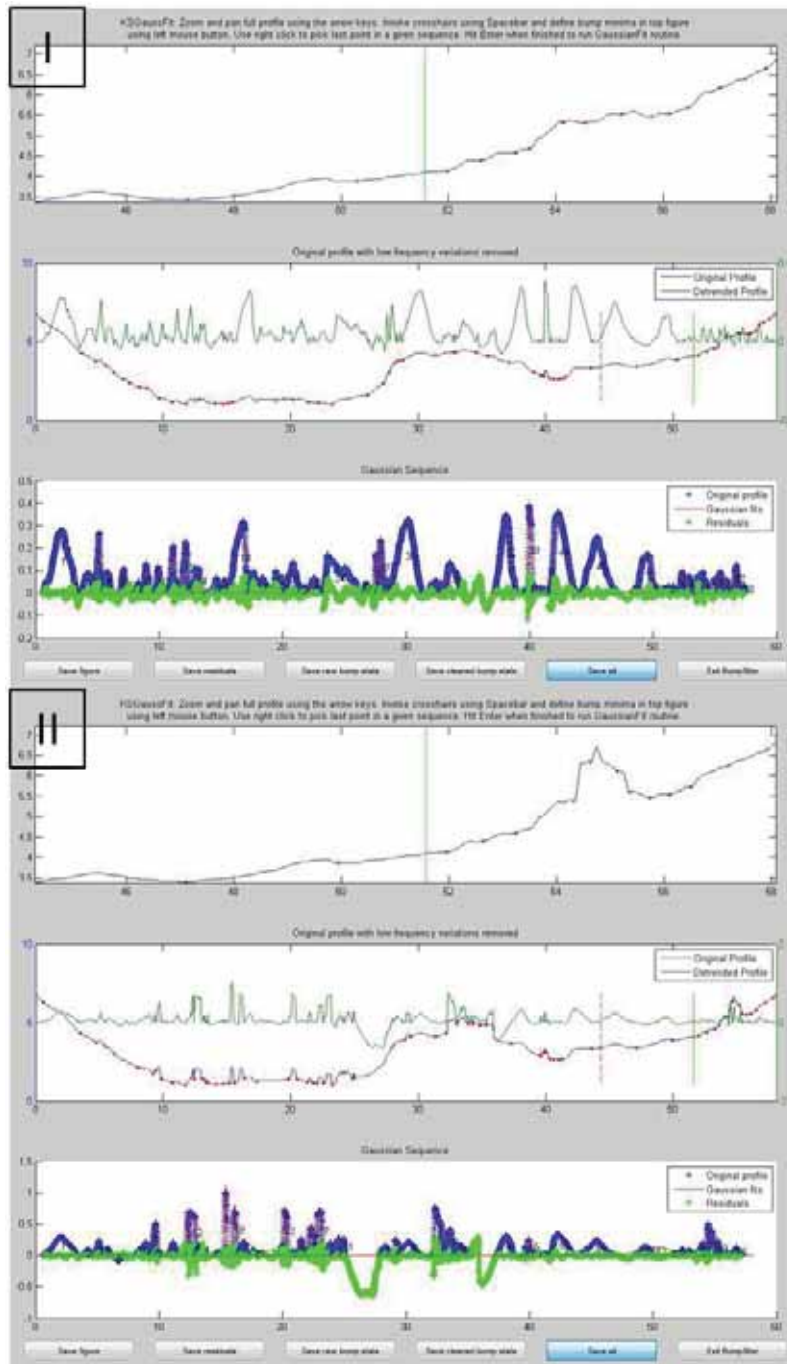


Figure 41: Modelled profiles of the cross section S2 from the 10 cm resolution of the DTM (I) and the DSM (II).

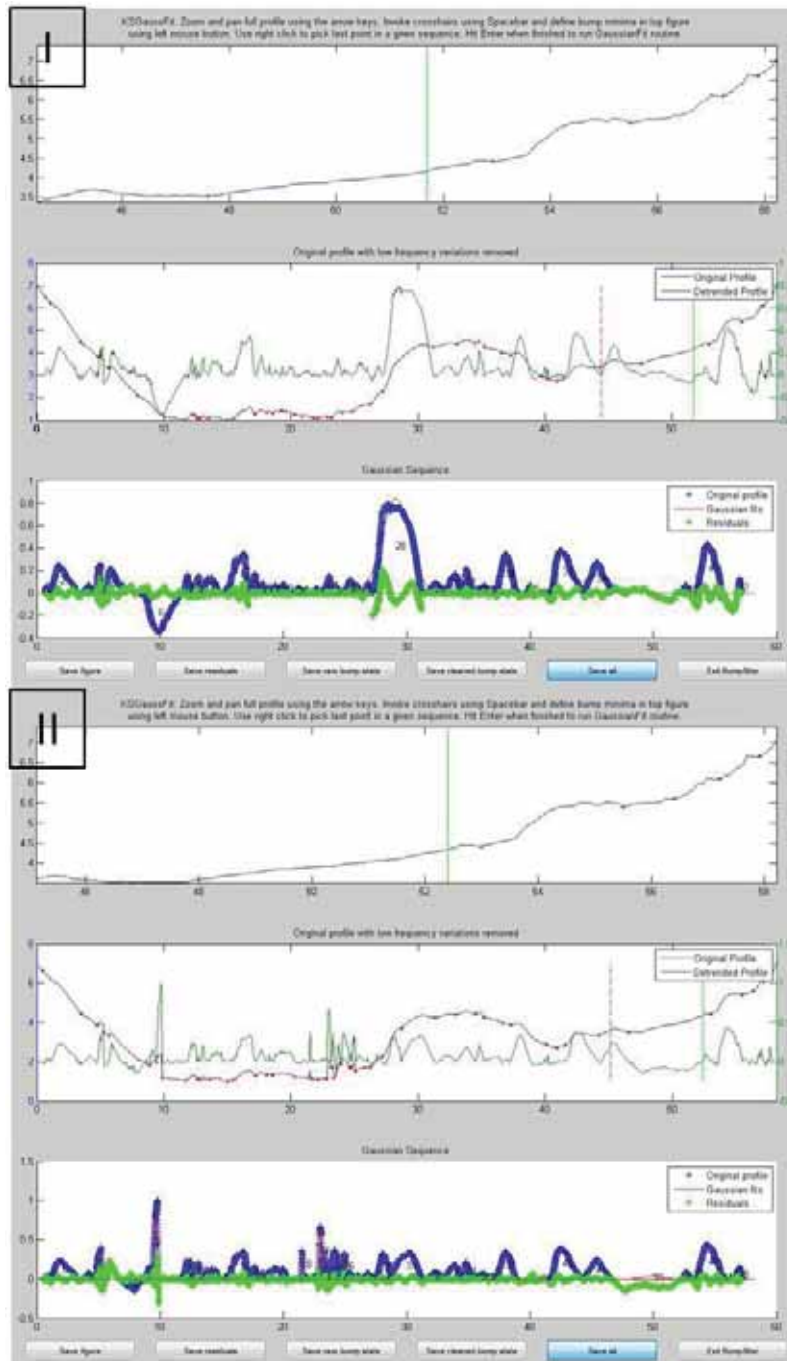


Figure 42: Modelled profiles of the cross section S3 from the 10 cm resolution of the DTM (I) and the DSM (II).

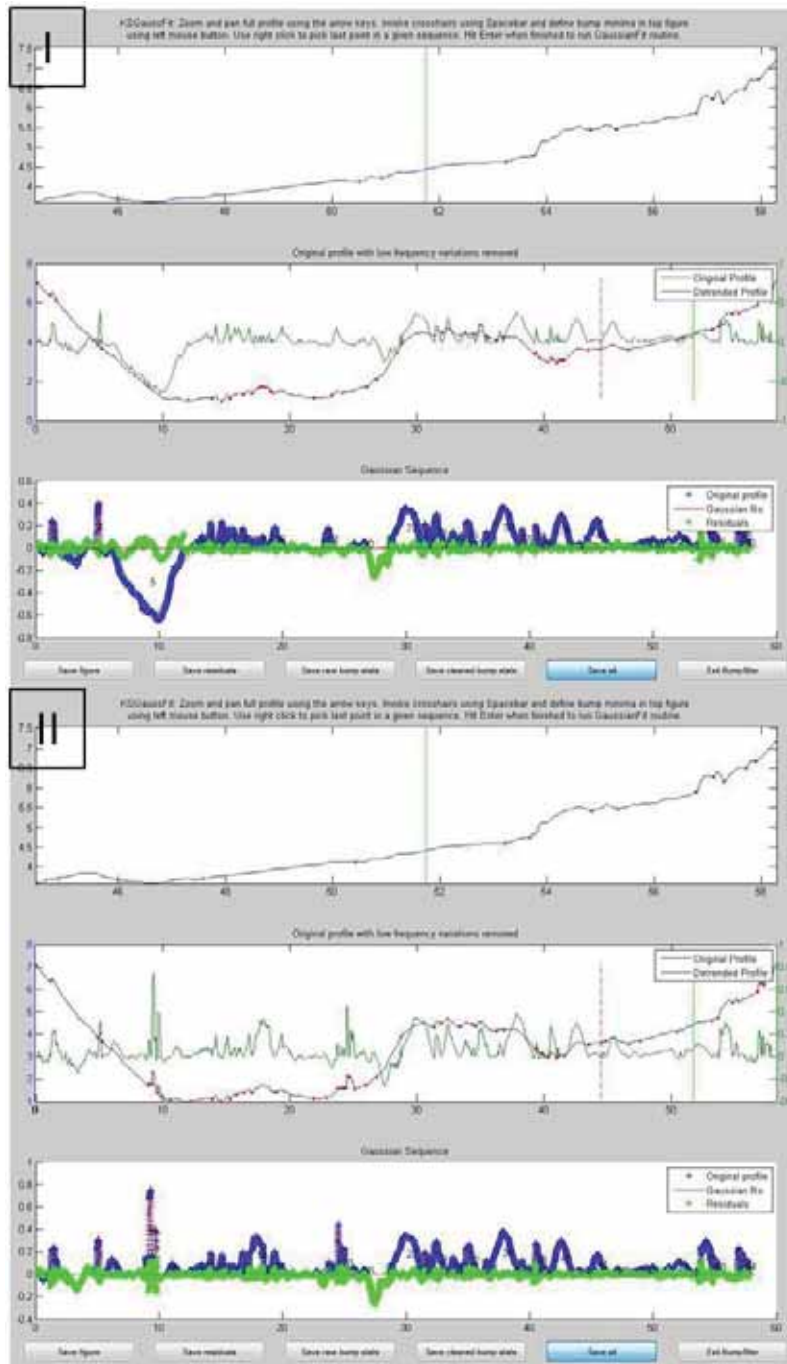


Figure 43: Modelled profiles of the cross section S4 from the 10 cm resolution of the DTM (I) and the DSM (II).

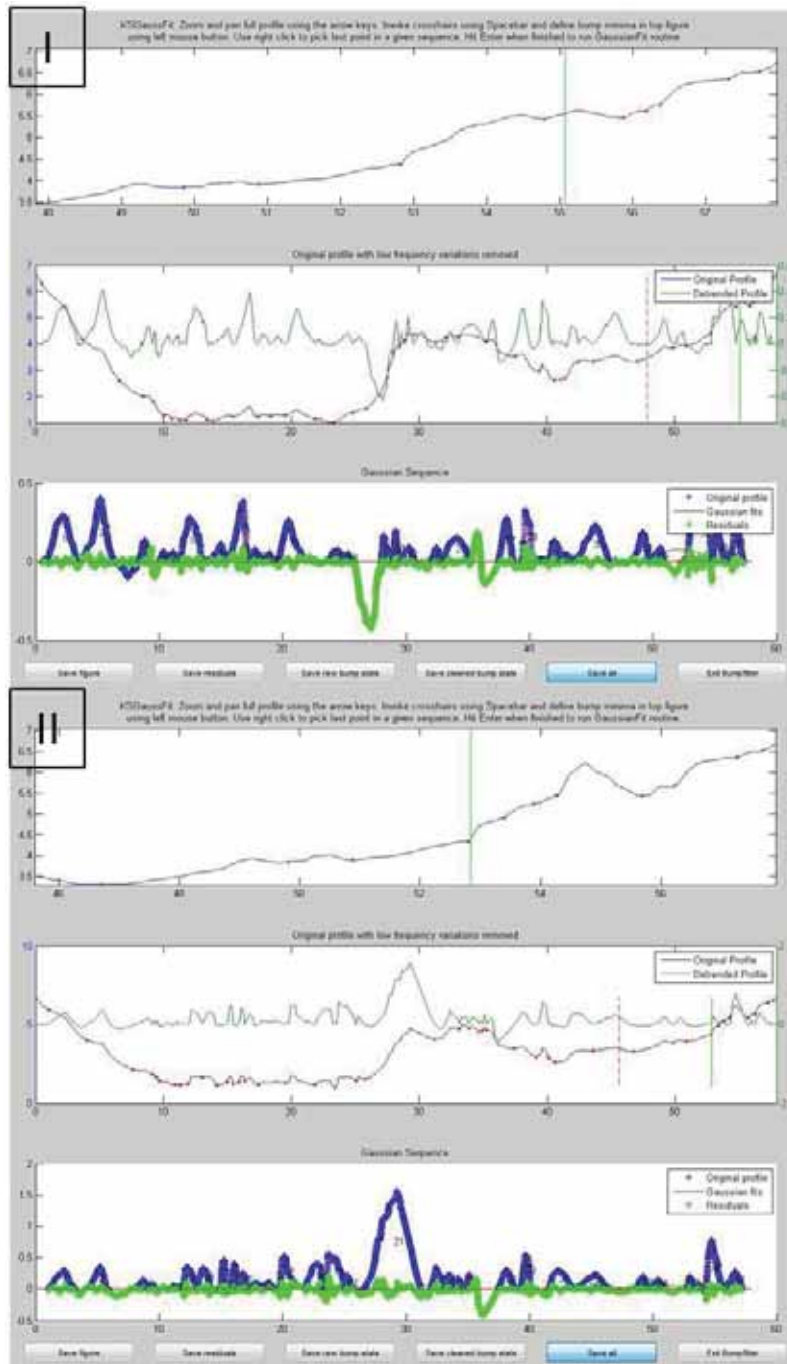


Figure 44: Modelled profiles of the cross section S1 from the 15 cm resolution of the DTM (I) and the DSM (II).

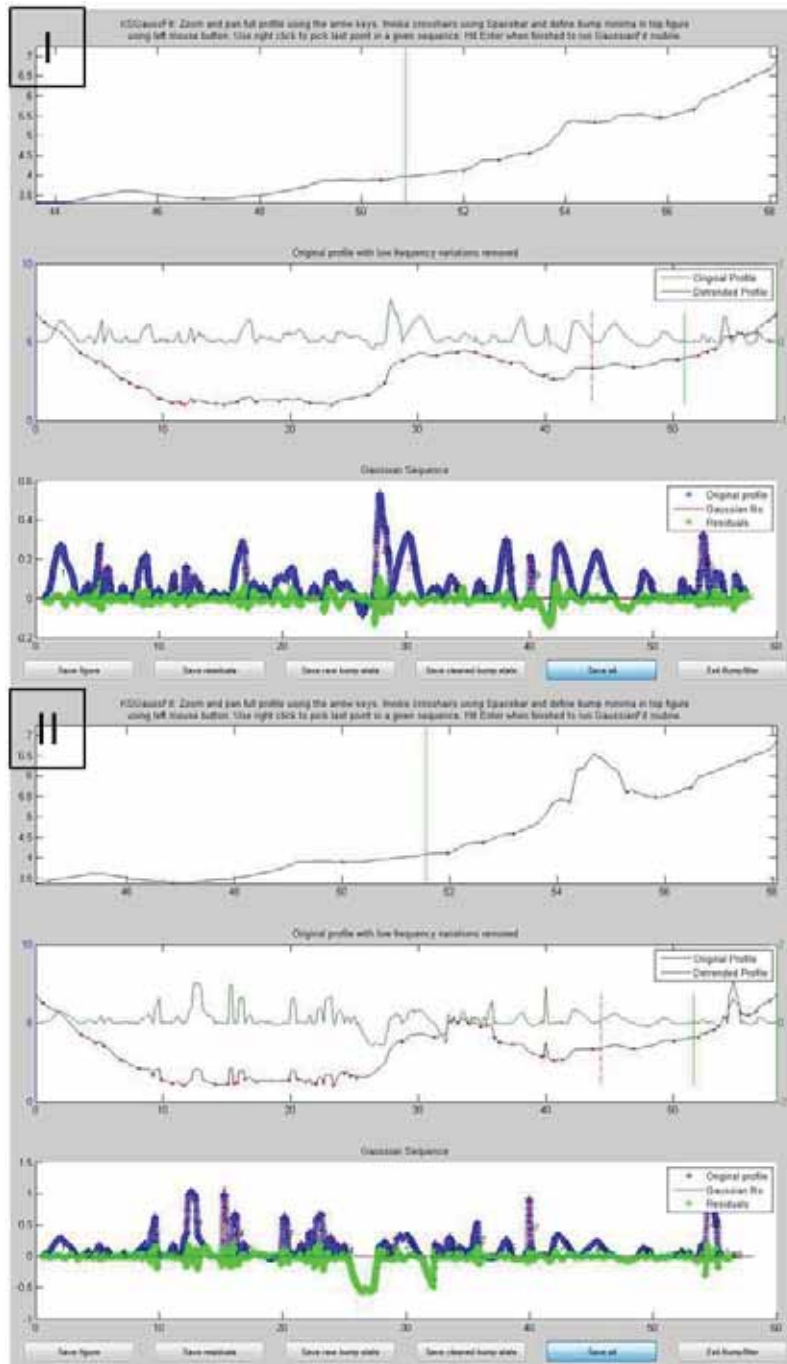


Figure 45: Modelled profiles of the cross section S2 from the 15 cm resolution of the DTM (I) and the DSM (II).

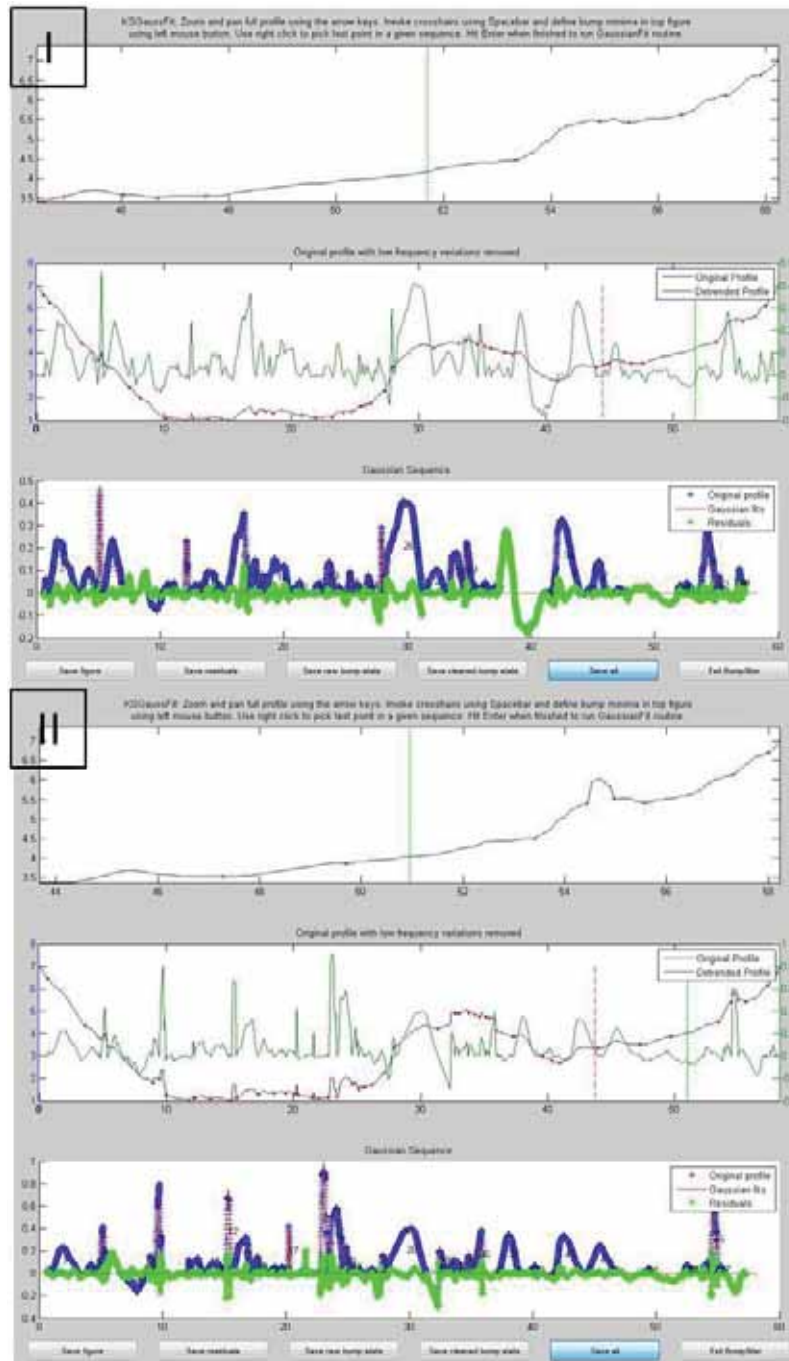


Figure 46: Modelled profiles of the cross section S3 from the 15 cm resolution of the DTM (I) and the DSM (II).

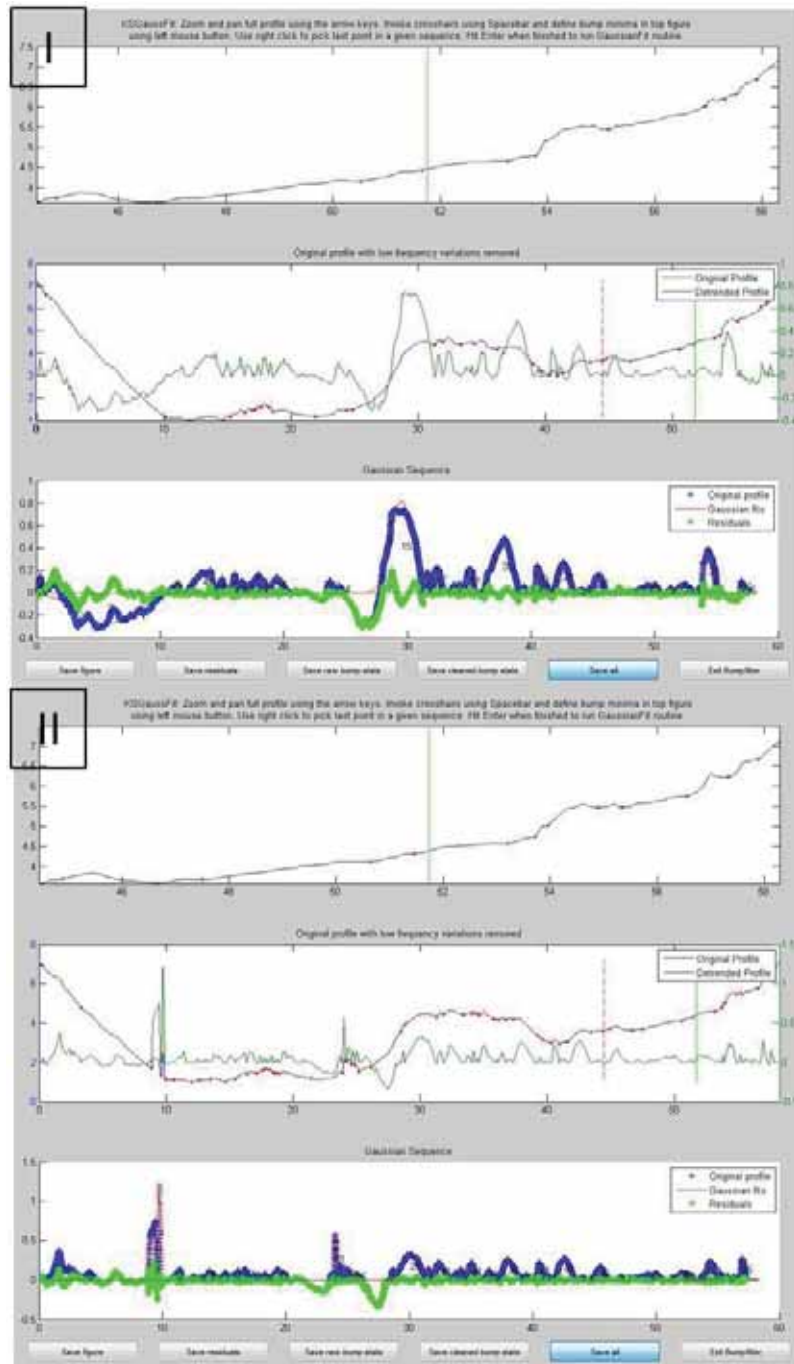


Figure 47: Modelled profiles of the cross section S4 from the 15 cm resolution of the DTM (I) and the DSM (II).